RSC Advances

ROYAL SOCIETY OF CHEMISTRY

REVIEW

View Article Online
View Journal | View Issue

Check for updates

Cite this: *RSC Adv.*, 2025, **15**, 30490

Nanographene horizons: the emerging role of hexa-*peri*-hexabenzocoronene in functional material design

Ehsan Ullah Mughal, *[a] Nafeesa Naeem, [a] Syeda Fariha Kainat,[a] Amina Sadiq[b] and Hanan A. Ogaly [c]

Received 29th June 2025
Accepted 8th August 2025

DOI: 10.1039/d5ra04623h

rsc.li/rsc-advances

Hexa-*peri*-hexabenzocoronene (HBC) and its derivatives have emerged as prominent polycyclic aromatic hydrocarbons (PAHs) due to their unique structural, electronic, and photophysical properties. This review provides a comprehensive overview of the synthetic strategies employed for the construction of HBC frameworks, ranging from traditional methods to recent advances that offer improved efficiency, regioselectivity, and structural diversity. The molecular architecture of HBCs, characterized by extended π-conjugation and planarity, contributes significantly to their stability and distinctive physical properties, including high charge-carrier mobility and tunable optical absorption. We further highlight the multifaceted applications of HBC-based materials, particularly in the realm of organic and optoelectronic devices, where their excellent semiconducting behavior and strong π–π stacking facilitate their use in organic field-effect transistors (OFETs), organic photovoltaics (OPVs), and organic light-emitting diodes (OLEDs). Their roles in energy storage, especially in supercapacitors and battery systems, are also discussed, focusing on their ability to enhance charge storage and cycling stability. Moreover, HBCs have demonstrated potential as catalytic platforms and chemical sensors due to their electron-rich surfaces and functionalizable peripheries. Finally, the incorporation of HBC derivatives in biomedical fields such as bioimaging and drug delivery is reviewed, with emphasis on their biocompatibility, fluorescence properties, and structural adaptability. Overall, this article underscores the significant progress in HBC research and its expanding role in diverse scientific and technological domains.

1. Introduction

Graphene[1,2] has captivated the scientific community due to its exceptional physical and chemical characteristics, particularly its outstanding electronic behavior.[3–5] These unique properties have led to its integration across a wide array of advanced technological domains, including energy storage devices such as batteries,[6,7] organic light-emitting diodes (OLEDs),[8–10] sensors,[11–13] and photovoltaic systems.[14–17] Despite its numerous advantages, single-layer graphene functions as a zero-band gap semiconductor, a feature that restricts its utility in conventional electronic applications. Hence, introducing a band gap while preserving its intrinsic qualities remains a crucial objective.

Band gap engineering in graphene can be achieved *via* chemical or physical methodologies. Chemical approaches are broadly categorized into "top-down"[18–20] and "bottom-up"[21–23] strategies. Top-down methods often result in materials with poorly controlled structures due to limited precision, whereas bottom-up techniques allow for the atomically precise synthesis of well-defined nanographene structures. These molecularly defined nanographenes are increasingly investigated for use in molecular electronics, photovoltaics, and sensor technologies, owing to their tunable structures and reproducibility.[24–26]

Among the synthetic approaches available, oxidative cyclodehydrogenation—commonly referred to as the Scholl reaction—is a key method used in the solution-phase construction of nanographenes from oligophenylene precursors.[27,28] This transformation generally employs Lewis or Brønsted acids in combination with oxidants[29,30] and is valued for its operational simplicity. Nevertheless, issues such as regioselectivity limitations and undesired rearrangements may arise.[31–33] To address these challenges, alternative strategies such as cyclodehydrohalogenation[34–36] and palladium-catalyzed annulation[37–39] reactions have been explored. Additionally, methods aimed at π-extension have been employed to enlarge smaller polycyclic aromatic hydrocarbon (PAH) frameworks.[40–49] Specific regions within PAHs—namely the K-,[50,51] bay-,[52–55] and L-regions[56]—serve as functionalization sites for annulative π-extension (APEX) as shown in Fig. 1.[57] A related method,

---

[a] Department of Chemistry, University of Gujrat, Gujrat-50700, Pakistan. E-mail: ehsan.ullah@uog.edu.pk
[b] Department of Chemistry, Govt College Women University, Sialkot-51300, Pakistan
[c] Chemistry Department, College of Science, King Khalid University, Abha 61421, Saudi Arabia

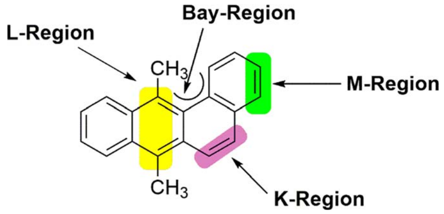

Fig. 1 Different regions of polycyclic hydrocarbons.[60]

dehydrative π-extension (DPEX), involves intramolecular cyclization of aryl aldehydes.[58,59]

Polycyclic aromatic hydrocarbons (PAHs) are a class of fused-ring compounds composed entirely of sp^2-hybridized carbon atoms. Structurally, they can be viewed as molecular fragments of graphene, exhibiting extended π-conjugation. The primary mode of intermolecular interaction among PAHs involves π–π stacking in a face-to-face fashion, although alternative packing motifs such as face-to-edge (herringbone) arrangements have also been observed. While PAHs occur naturally in combustion byproducts, the isolation of pure and structurally defined PAHs requires controlled synthetic procedures. Over time, a broad range of PAHs with varying geometries and dimensionalities have been synthesized, from linear systems like pentacene to more complex two-dimensional frameworks such as perylene.[61,62] Numerous PAHs have demonstrated utility as active materials in organic electronics. Pentacene, for instance, is a benchmark PAH known for its performance in organic field-effect transistors (OFETs),[63–65] where its high molecular order and strong intermolecular interactions contribute to efficient charge carrier mobility—a critical parameter for device operation. In recent years, attention has expanded to include larger PAHs, which are being explored as potential electrode materials due to their structural resemblance to extended graphene sheets.[61,66]

Among these large PAHs, hexa-*peri*-hexabenzocoronene (HBC) represents a prominent disc-shaped molecule composed of 42 carbon atoms (Fig. 2b). Owing to its rigid planar structure and extensive π-conjugation, HBC exhibits remarkable thermal and chemical stability. The molecular symmetry and shape of HBC promote its self-assembly into columnar architectures *via* strong π–π interactions. These packing characteristics render unsubstituted HBC virtually insoluble, requiring techniques such as vacuum deposition for film processing. However, chemical modification of the HBC core allows the introduction of solubilizing groups, enabling solution processability and unlocking properties such as liquid crystalline behavior. The synthetic flexibility of HBC derivatives permits a wide range of functionalization, expanding their applicability in areas such as nanostructured materials, organic electronics, and energy storage.[67]

HBC is a highly symmetrical nanographene molecule, characterized by a flat, disc-shaped structure made up of seven interconnected benzene rings. It stands out as one of the smallest and most structurally uniform representatives in the class of molecular nanographenes. This fully benzenoid PAH benefits from the distribution of π-electrons into Clar's aromatic sextets,[68] a feature that contributes to its high thermodynamic stability. Functionalization at the peripheral positions of HBC is straightforward, enabling the attachment of bulky groups—such as *tert*-butyl moieties—to improve solubility and reduce aggregation. Alternatively, linear alkyl chains[69–73] can be introduced to direct the molecule's self-assembly into supramolecular architectures. For example, long alkyl chains promote the formation of one-dimensional columnar stacks, while amphiphilic side chains may lead to the development of nanotubular structures.[74–77]

The photophysical properties of HBC are well-documented. Its absorption spectrum in the near-UV and visible regions can be divided into three distinct bands: the p-band (HOMO–LUMO transition), and the α- and β-bands, which arise from transitions of different symmetry as shown in Fig. 3.[78,79] The β-band, being symmetry-allowed, dominates the absorption profile near 360 nm,[80] while the symmetry-forbidden α- and p-bands appear at approximately 450 nm and 390 nm, respectively. The p-band gains intensity through vibronic coupling with the β-band, whereas the α-band remains relatively weak due to its greater energy separation.[81] Fluorescence emission from HBC typically exhibits structured peaks centered around 490 nm, with a singlet excited-state lifetime of roughly 50 nanoseconds[80,82] consistent with its forbidden transition nature. At cryogenic temperatures (77 K), phosphorescence is observed, characterized by emission maxima near 565 and 575 nm.[83]

Electrochemical studies of HBC reveal oxidation potentials at approximately +1.1 and +1.3 V *versus* the ferrocene/

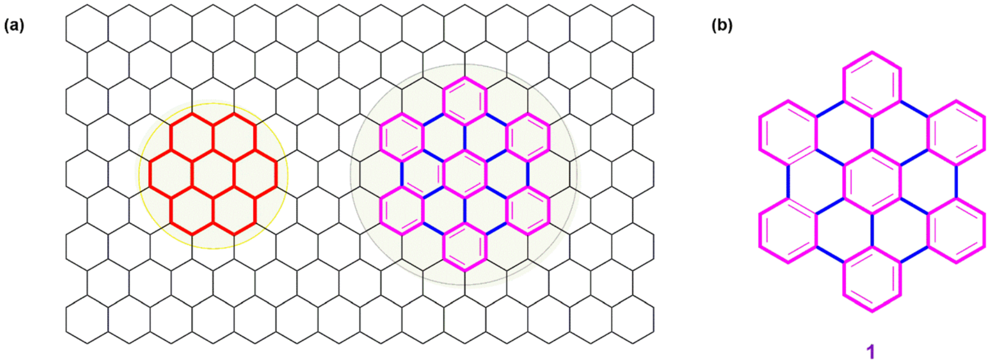

Fig. 2 (a) Graphene sheet and (b) HBC (1).

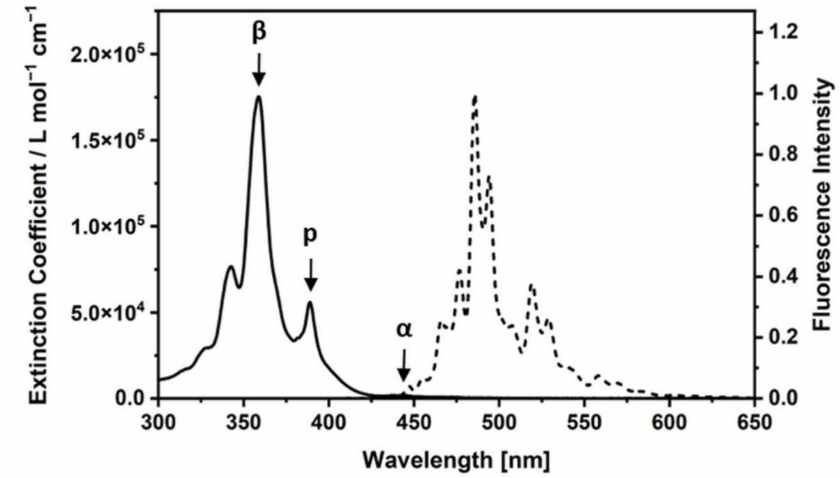

Fig. 3 Absorption (solid line) and fluorescence spectra (dashed line) of HBC. Reproduced from ref. 81 with permission from Elsevier, Copyright © 2023.

ferrocenium (Fc/Fc$^+$) couple, and a reduction potential at −1.7 V *versus* Fc/Fc$^+$ in dichloromethane. The radical cation form of HBC shows characteristic absorption bands at 551 and 840 nm, further emphasizing its rich redox behavior and potential for optoelectronic applications.[84]

This review aims to provide a comprehensive overview of the synthetic strategies employed for HBC construction, along with a critical analysis of their structure–property relationships and applications. Special attention is given to the use of HBC derivatives in organic and optoelectronic electronics, energy storage devices and supercapacitors, catalysis and chemical sensing, as well as their emerging roles in bioimaging and drug delivery. By consolidating current advancements and challenges, this article seeks to guide future efforts toward the rational design and functional deployment of HBC-based materials in next-generation technologies.

2. Synthesis of HBC and its derivatives

2.1. Classical synthetic approach

Various synthetic strategies for HBC have been reported in the literature.[66] A notable method for synthesizing HBC derivatives was introduced by Müllen and colleagues, wherein in 1995, functionalized hexaphenylbenzene (HPB, **2**) was oxidized using copper(II) and aluminum(III) salts. In this protocol, Cu(II) served as an oxidant, while Al(III) acted as a Lewis acid, facilitating the synthesis of alkyl-substituted HBCs under relatively mild conditions.[85,86] These alkylated derivatives exhibited significantly improved solubility, which in turn simplified both their purification and structural characterization.

The HPB core itself can be constructed through the cyclotrimerization of 1,2-diphenylethyne (**4**) catalyzed by dicobalt hexacarbonyl complexes. This method, outlined in Scheme 1 (Method 1), is well known for its tolerance to a broad range of functional groups.[87–89] Using this strategy, C_3-symmetric HBC molecules were obtained from asymmetrically substituted tolanes bearing functional moieties such as alkyl chains and ester groups.[90] The cobalt-catalyzed trimerization of HPB yielded two distinct regioisomers, which could be efficiently separated prior to the oxidative cyclodehydrogenation step.

An alternating substitution pattern consisting of alkyl and ester functionalities was introduced successfully in about 63% of the HPB intermediates and over 85% of the final HBC products. However, when this method was applied to a trimethoxy-substituted C_3-symmetric HBC bearing alkyl groups, the yield of the target HBC significantly declined. This drop in efficiency was attributed to methoxy group migration and the concurrent formation of undesired spirocyclic dienone byproducts.[91]

An alternative strategy to modify the functional periphery of the HBC framework involves the [4 + 2] Diels–Alder cycloaddition (Scheme 1, Route 2).[92,93] In this approach, cyclopentadienone (**5**) reacts with alkyne (**4**) to generate a carbonyl-bridged intermediate, which upon the elimination of carbon monoxide yields the corresponding HPB derivative. Additionally, the HPB core can be assembled *via* a Suzuki–Miyaura cross-coupling reaction between sterically hindered 1,4-diiodo-2,3,5,6-tetraarylbenzenes (**6**) and appropriately functionalized boronic esters (**7**), ultimately furnishing D_2-symmetric HBCs after planarization (Scheme 1, Method 3).[94]

Another synthetic route to C_3-symmetric HBCs involves Suzuki coupling between 1,3,5-tribromobenzene (**8**) and biphenyl boronic acid derivatives (**9**), as illustrated in Scheme 1, Method 4.[95] The resulting 1,3,5-tris(2′-biphenyl)benzene (**3**) serves as a precursor for the parent HBC upon oxidative cyclodehydrogenation. This methodology has also proven effective in producing alkoxylated HBC derivatives in nearly quantitative yields.[32] Likewise, Suzuki coupling between 1,3,5-tris(bromophenyl)benzene (**10**) and aryl boronic acid derivatives (**7**) yields C_3-symmetric HBCs (Scheme 1, Method 5).[96]

The Scholl reaction, a Lewis acid-mediated oxidative aryl–aryl coupling, remains a pivotal step across most established HBC synthetic routes.[97,98] Early protocols utilizing NaCl/AlCl$_3$ were constrained by harsh conditions, limiting their functional

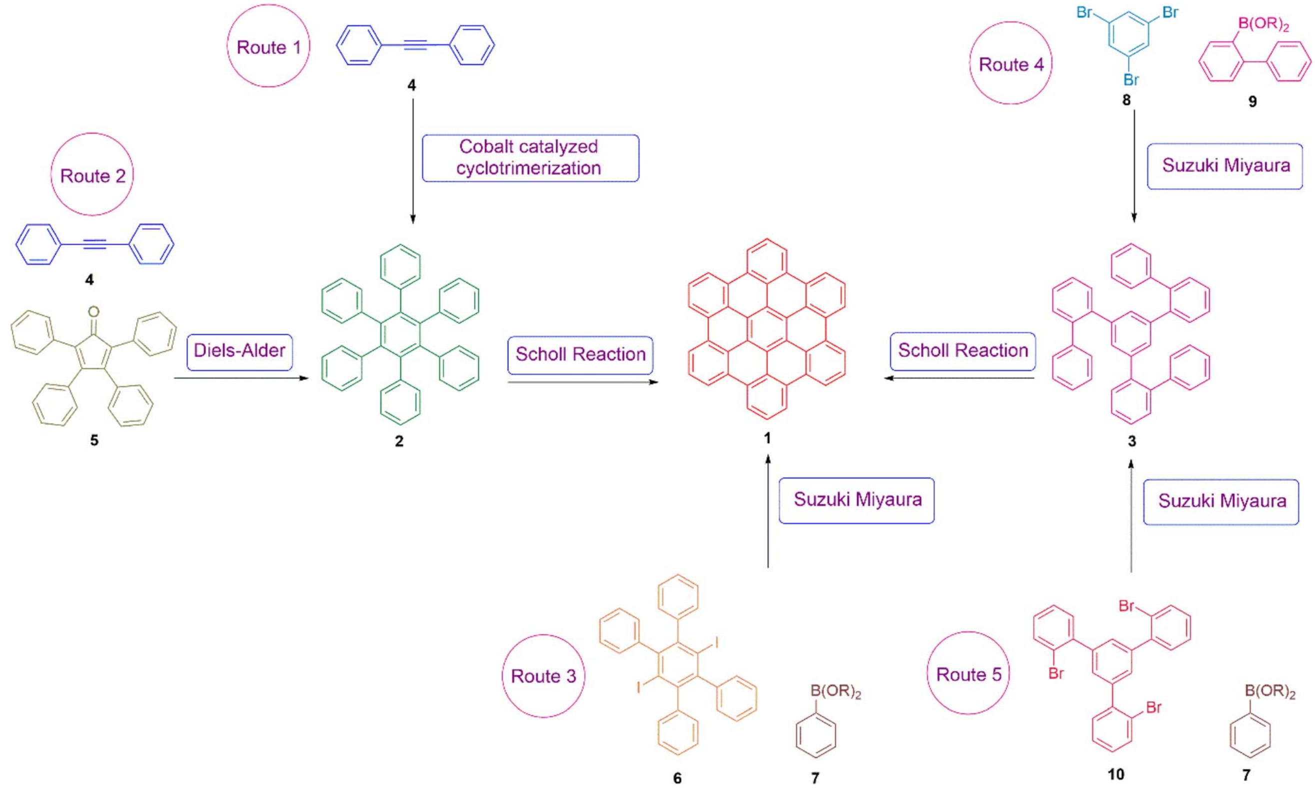

Scheme 1 Different routes for the synthesis of HBC core molecule.[67]

group compatibility. Subsequent improvements under milder conditions—such as FeCl$_3$ or nitromethane-assisted oxidative cyclodehydrogenation—enabled the efficient formation of highly substituted HBCs with improved yields.[92,93] Iron(III) salts, serving as both oxidants and Lewis acids, minimize side reactions like dealkylation, halogenation, and alkyl group migration. Functionally diverse HPB halide precursors can be easily obtained, offering versatile platforms for downstream modifications.[91]

Other oxidation systems have also been reported, including AlCl$_3$ in combination with PhI(O$_2$CCF$_3$)$_2$/BF$_3$·Et$_2$O,[99] DDQ under acidic conditions,[100] MoCl$_5$, and Cu(II) salts (chlorides or triflates).[101] These reagents facilitate the transformation of HPB into both unsubstituted and substituted HBCs. Functionalized derivatives include halogenated variants (*e.g.*, fluorinated or iodinated) and those bearing chiral, linear, branched, or aromatic alkyl chains.[102–105] Depending on the substituent pattern, Scholl-type reactions can yield structurally diverse HBC architectures.

Precursors such as tris(biphenyl)benzenes have also been converted to hexakis-alkoxy HBCs[91] and in some instances, trialkyl-substituted HBCs.[106] However, these oxidative cyclizations are often limited when substrates contain chemically incompatible groups or generate stable intermediates. For example, attempts to synthesize alkoxy-substituted HBCs *via* FeCl$_3$-mediated oxidative cyclization frequently led to side reactions, including the formation of quinone or indenofluorene derivatives and products arising from methoxy migration.[32,91,107,108] The use of precursor variant **3**, a 1,3,5-tris(biphenyl)benzene derivative, or the incorporation of a phenyl linker (as per Scheme 1, Route 4) facilitated access to the desired hexakis-alkoxy HBCs.[32,109–112]

Functional groups such as alkanones, ester-containing alkoxycarbonyls, and methylene alkanoates are often incompatible with FeCl$_3$ conditions due to their sensitivity to oxidation.[67,113] However, the presence of four to six *tert*-butyl solubilizing chains on HPB intermediates improves both the solubility and yields of the resulting HBCs under FeCl$_3$ or DDQ conditions. In one instance, a *tert*-butyl-substituted 1,4-bis(2′-biphenyl)yl-2,5-diphenylbenzene required sequential FeCl$_3$ treatments to achieve full cyclodehydrogenation.[96,100,114,115] In general, electron-donating (*e.g.*, alkoxy, amine) or electron-withdrawing (*e.g.*, nitrile, carbonyl) substituents interfere with planarization; however, such electronic effects can be mitigated by introducing peripheral spacers or additional solubilizing groups.

Fluorinated derivatives demonstrate that substitution on the central core with fluorine atoms yields acceptable products, whereas hexakis(4-bromophenyl)benzene consistently fails to undergo complete oxidative cyclodehydrogenation under various conditions.[102,116,117] Typical side reactions during Scholl-type HBC synthesis include unwanted chlorination and polymerization, which can be suppressed by adjusting reagent stoichiometry and continuously purging the reaction mixture with an inert gas to remove evolved hydrogen chloride. The occasional isolation of semifused HPB intermediates suggests a stepwise mechanism for cyclization.[92,111]

Two primary mechanistic pathways have been proposed for the Scholl reaction: the arenium-ion mechanism and the radical-cation pathway (Scheme 2, Routes A and B).[99,108,118–121] In the arenium-ion route (Scheme 2, Path A), protonation of the aromatic precursor forms a σ-complex (**11a**), which undergoes electrophilic aromatic substitution, deprotonation, and further

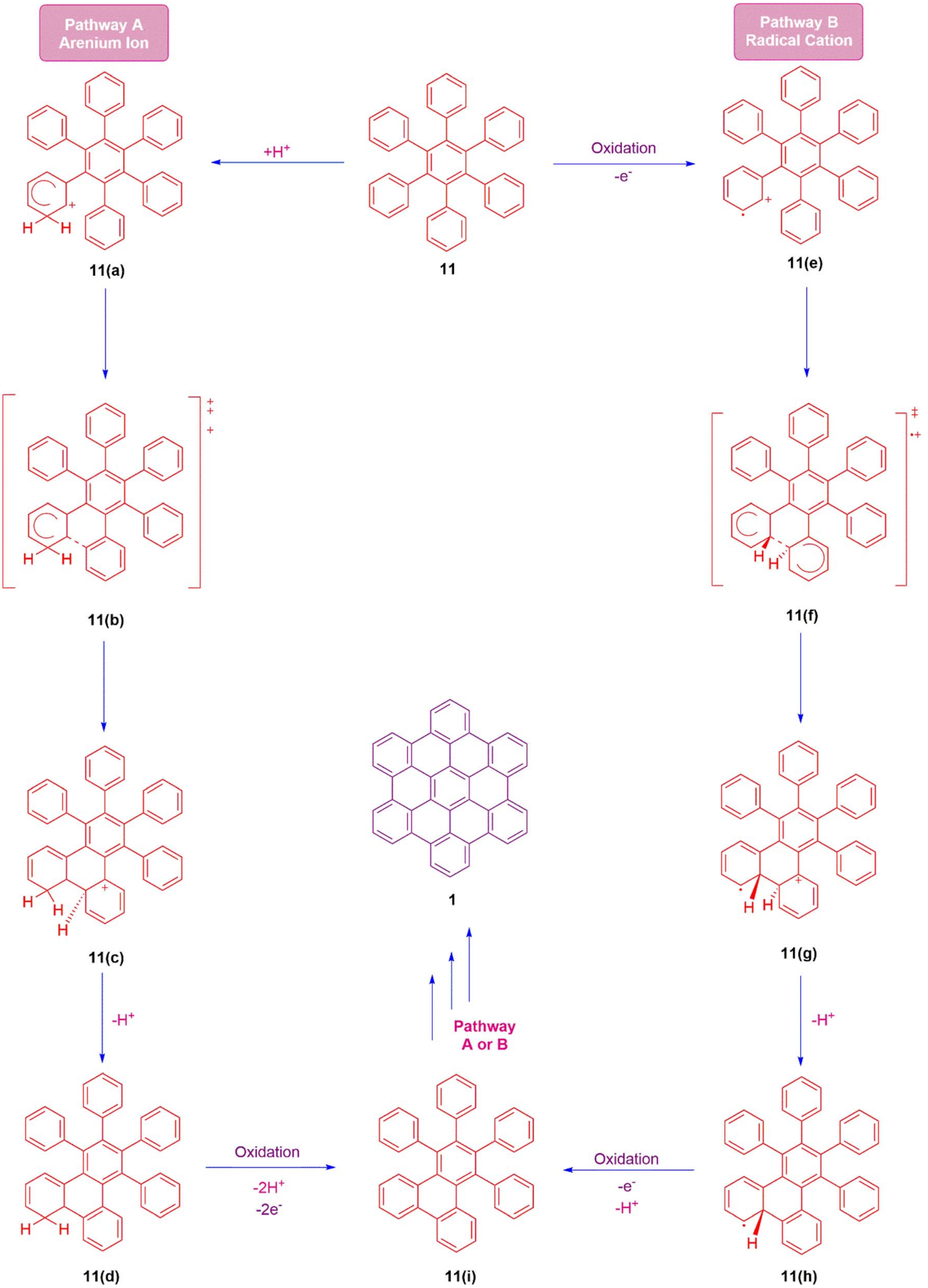

Scheme 2 Scholl reaction for the conversion of HBP to HBC, the proposed mechanism for arenium ion (A) and radical cation (B) respectively.[99,108,118–121]

oxidation to yield the fully fused product (**11i**). Alternatively, the radical-cation mechanism (Scheme 2, Path B) involves a single-electron oxidation to generate a radical cation (**11e**), which then reacts with an adjacent arene to form a C–C bond (**11g**), followed by further oxidation and proton elimination to restore aromaticity and complete the ring fusion to form **11i**.

Selective functionalization of HBC at the 6, 12, or 18 positions is readily achievable and has been explored through various regioselective approaches. A wide array of solubilizing groups has been introduced, as illustrated in Fig. 4a (**12** and **13**). Furthermore, the incorporation of reactive functionalities such as aryl halides facilitates subsequent derivatization *via* cross-coupling reactions.[116] Extension of the π-conjugated framework has been accomplished by integrating acetylene-based moieties, including phenylacetylene and diphenylacetylene derivatives, often bearing polar or nonpolar alkyl chains. The attachment of hydrophilic, fluorous, or lipophilic solubilizing segments to the HBC core has led to the formation of amphiphilic HBC systems, as shown in Fig. 4b (**14**). Particularly, Gemini-type amphiphilic HBCs have shown remarkable capacity for directing supramolecular self-assembly (Figure 4c, **15**).[122] The strategic introduction of electroactive, photoreactive, or chemically labile groups—either directly onto the HBC periphery or *via* spacer linkers—has enabled the construction of more architecturally sophisticated HBC derivatives.[95,123,124]

Amido- and ureido-functionalized HBC derivatives, such as **16** and **17**, have been successfully employed in the formation of organogels (Fig. 5).[125] Additionally, HBC-containing pendants and ladder-type polymers constructed on a polynorbornene backbone have been synthesized, as exemplified by **18**.[126] Covalent linkage of ethynyl-substituted HBC to an electron-deficient perylene monoimide unit has been achieved *via* an acetylene spacer using the Sonogashira–Hagihara cross-coupling strategy, yielding **19** (Fig. 5).[127] In a related approach, azobenzene moieties have been anchored to the HBC core to create optically responsive molecular switches, such as **20**.[128]

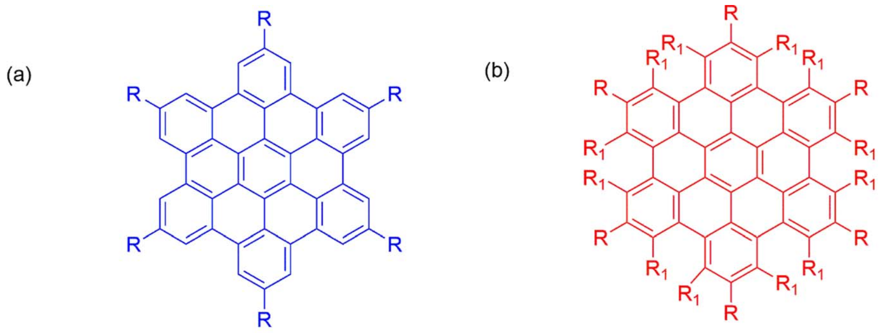

12

$R=$ Alkyl, alyklphenyl, alkoxy, acetylene aryl(aryl, dendtric), amine

13

$R= R_1 =$ Methoxy
$R=$ H $R_1 =$ Methyl
$R=$ Alkyl $R_1 = D$
$R =$ Alkoxy $R_1= F$

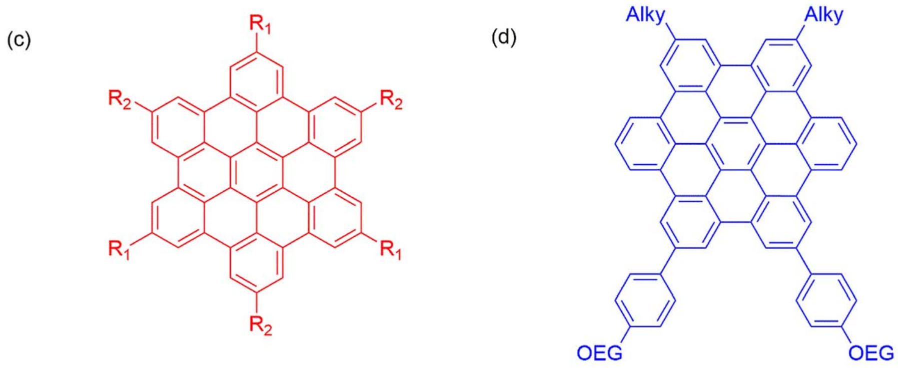

14

$R_1= R_2 =$ Acetylene-phenyl (OEG)
$R_1=$ Alkyl $R_2 =$ Phenyl (OEG)
$R_1= R_2 =$ Perfluoroalkyl

15

OEG = ethylene glycol chain with a possiblity to attached other functional groups on the end of chains

Fig. 4 Different structures of functionalized HBC molecules (a) symmetrical 6-, 12-, and 18-fold substituted HBCs (b) core–shell structure (c) (a and b) symmetrical 6-, 12-, and 18-fold substituted HBCs (d) Gemini-shaped amphiphilic HBCs.[95,123,124]

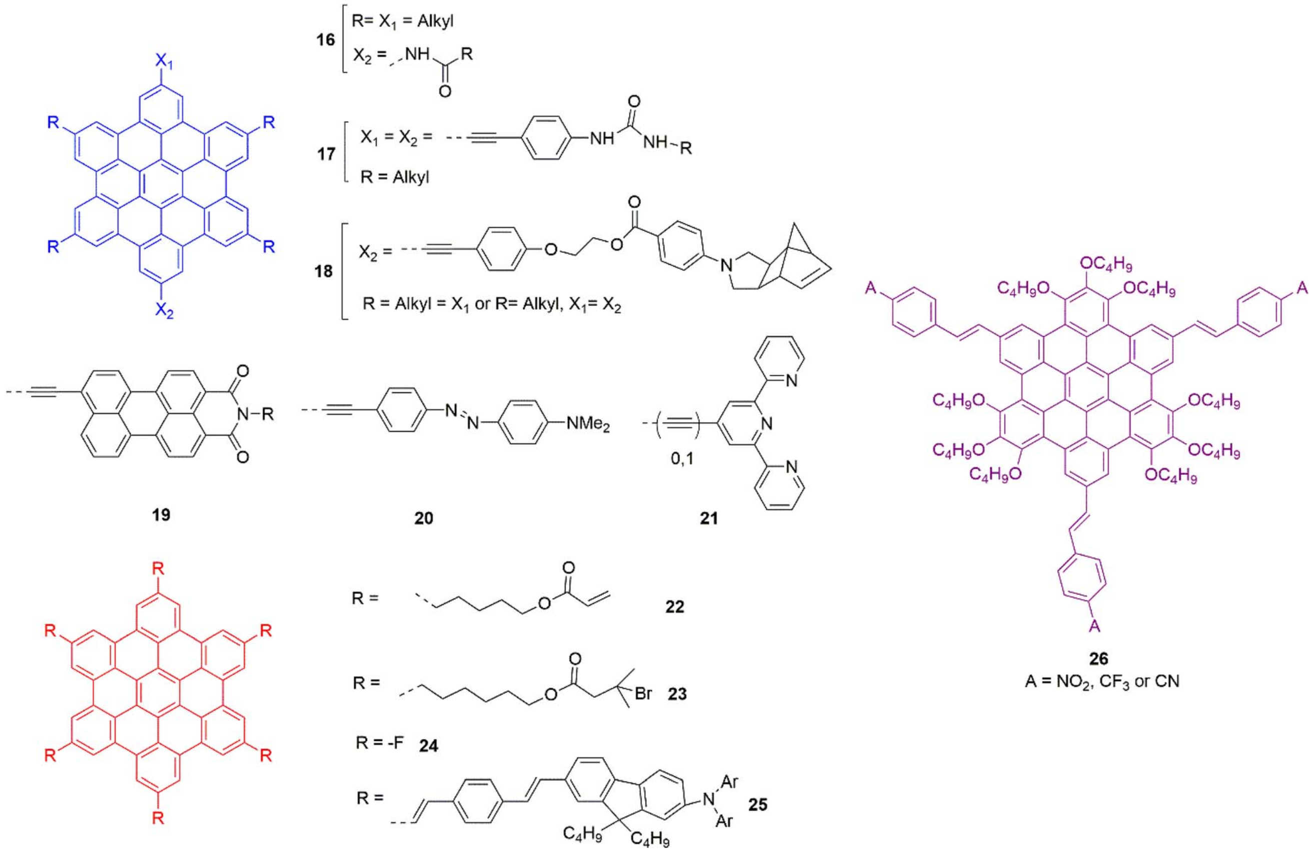

Fig. 5 HBC derivatives incorporating diverse functional groups for applications in optical absorption, cross-linking, hydrogen bonding, and related functionalities.[127]

Moreover, the introduction of terpyridine functionalities to the HBC scaffold has facilitated coordination with transition metals, resulting in the formation of HBC-based metal complexes, as illustrated by **21**.[105] Physical cross-linking of HBC aggregates using acrylate derivatives (**22**) or 2-bromo-2-methylpropionic ester (**23**) has led to the generation of robust and structurally stable HBC architectures with favorable synthetic yields.[129]

Kikuzawa *et al.* explored the synthesis of 2,5,8,11,14,17-hexafluoro-HBC (**24**) *via* a Diels–Alder reaction involving 4,4′-difluoro-diphenylacetylene and tetrakis(4-fluorophenyl) cyclopentadienone. This approach contrasts with previously reported strategies for synthesizing hexakis(iodo)-substituted HBCs.[89,102,116] The resulting HPB intermediate was subjected to oxidative cyclodehydrogenation using either $FeCl_3$ or a combination of $AlCl_3$ and $Cu(OTf)_2$, achieving moderate yields of 47% and 64%, respectively.[102] The incorporation of fluorine atoms enhances n-type semiconducting behavior by stabilizing the frontier molecular orbitals and promoting favorable C–H⋯F–C intermolecular interactions.[130,131]

Additionally, star-shaped HBC derivative **25** (ref. 132) and the C_3-symmetric "octupolar" HBC **26** (ref. 133) have emerged as promising molecular systems for two-photon absorption applications due to their donor–acceptor architectures. Compound **25** was synthesized through the Pd-catalyzed Heck coupling of conjugated peripheral acceptor moieties onto a cyclized hexaiodo precursor. In the case of **26**, alternating donor and acceptor units were strategically introduced, starting with an asymmetric toluene derivative bearing both ester and alkoxy groups. Subsequent transformations using the Wittig–Wadsworth–Emmons reaction enabled the incorporation of electron-withdrawing functionalities such as nitro, nitrile, and trifluoromethyl groups from a triphosphonate-based HBC intermediate.[133]

Following the development of Gemini-type amphiphilic HBC derivatives **18**, Fig. 4d, a diverse array of structurally advanced analogs has been reported.[110] Using symmetric or asymmetric alkynes, the synthetic strategy illustrated in Scheme 1, Route 2, facilitated the construction of HPBs bearing photoactive, electroactive, or halogen substituents, which were amenable to further derivatization. Cyclodehydrogenation under mild conditions yielded the corresponding HBCs in moderate to high efficiencies. Amphiphilic HBC derivatives have also been functionalized with dithienylethene pendants,[122] thiol groups,[134] norbornene units,[135] azides,[136] pyridine moieties,[137] and electron-deficient components such as 4,5,7-trinitro-9-fluorenone (TNF),[138] coumarins,[139] isothiouronium groups, and C_{60}-fullerene conjugates.[140] These modifications enabled the formation of stable, peripherally substituted conductive nanostructures.

Fluorenyl-based HBCs (FHBCs) have also gained attention for their chemical tunability and solution-processable characteristics. Upon cyclodehydrogenation, HPBs containing dioctylfluorene units yielded a series of HBCs with well-defined cores (**27–30,** Fig. 6).[141] The reactive halogen atoms present on the fluorene side chains allowed further transformations *via*

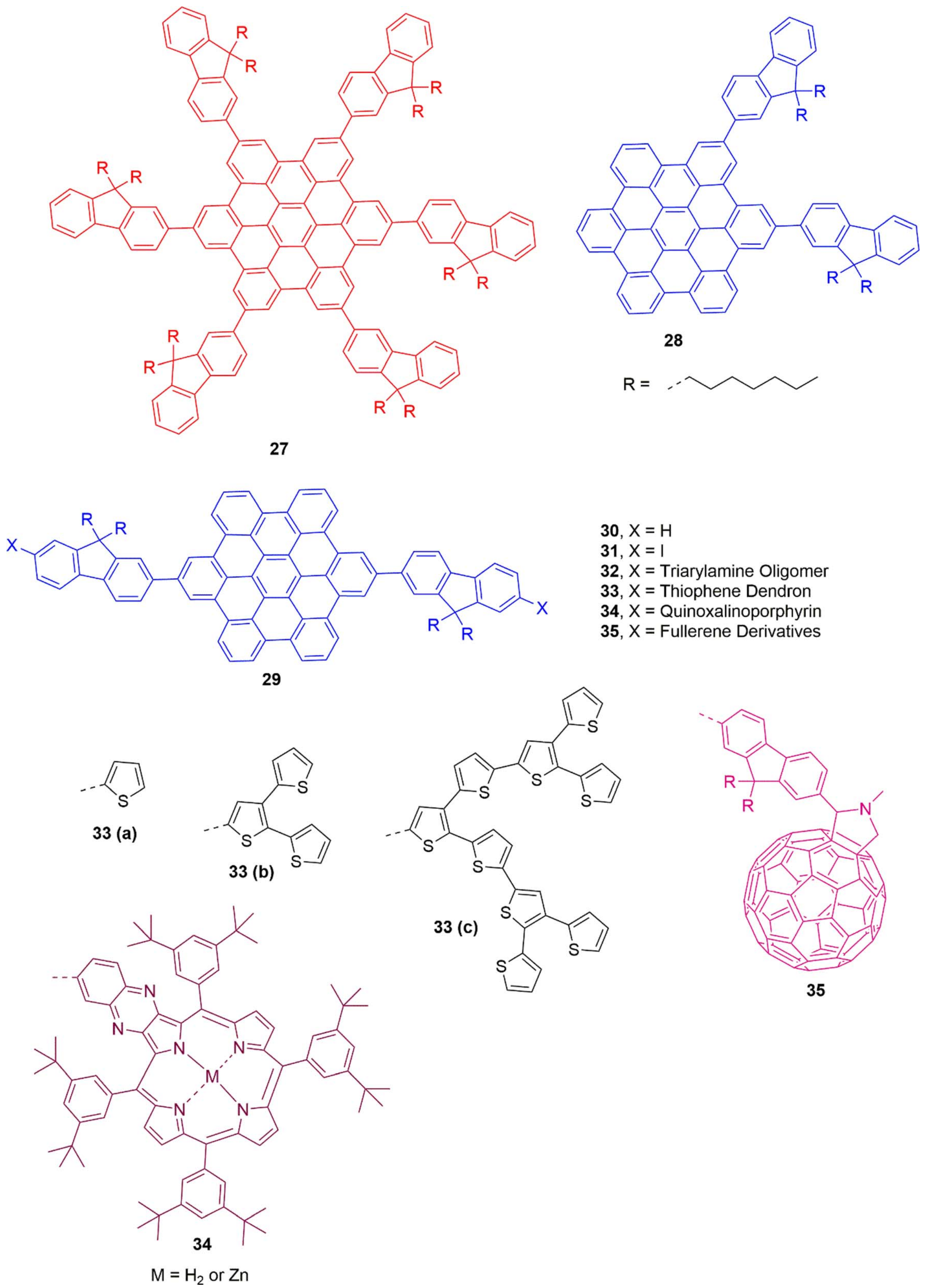

Fig. 6 Core structure of FHBC derivatives incorporating pendant arylamines, thiophenes, porphyrins, and fullerenes.[141,144,145]

Suzuki–Miyaura cross-coupling, Buchwald–Hartwig amination, and lithium–halogen exchange reactions (Figure 6, **31**). These reactions facilitated the targeted synthesis of functional derivatives including electron-rich arylamines **32**,[103] thiophenes **33**,[142,143] porphyrins **34**,[144] and fullerene adducts **35**.[145]

Zhang *et al.* (2014) synthesized a series of triptycene derivatives (**36a–c**) incorporating mono-, di-, and tri-substituted HBC units within the triptycene scaffold, as illustrated in Fig. 7. The planar geometry of the HBC moiety induces a pronounced deshielding effect, resulting in notable downfield shifts of the methine protons in the triptycene core. The expanded internal molecular free volume (IMFV) of these triptycenes presents considerable potential for hosting novel guest molecules, making them promising candidates for applications in supramolecular chemistry and biomedicine.[146]

Hirsch *et al.* (2014) reported the first synthesis of a linear HBC–porphyrin conjugate (**40**), featuring a *meso*-linked connection between the chromophoric units. A key intermediate in this synthesis was hexaphenylbenzaldehyde (**38**), which serves as a soluble precursor to its otherwise insoluble HBC analogue. Compound **38** was obtained in high yield on a gram scale *via* a solvent-free microwave-assisted Diels–Alder reaction, overcoming the typical synthetic bottleneck. Subsequent oxidation of the HPB intermediate (**39**) to the HBC core was successfully achieved in the presence of the free-base porphyrin, without requiring metalation of the macrocycle, as depicted in Scheme 3. This strategy enabled the construction of a novel carbon-rich molecular architecture containing two photoactive and redox-active moieties with electronic communication.[147]

Wei *et al.* (2014) introduced a straightforward and efficient synthetic approach based on the cyclodehydroannulation (CSA) strategy for the preparation of 3-fold symmetric, highly substituted c-HBCs. This method utilizes simple starting materials and employs benzylic carbon centers as annulation partners, offering a practical alternative to previously reported techniques. The synthesis proceeds through two key multifold transformation steps under mild reaction conditions, yielding the desired products in good to excellent yields. These features render c-HBCs among the most synthetically accessible large PAHs, while also providing a versatile platform for chemists and materials scientists. Particularly, this method allows for the synthesis of extended molecular graphenes and heteroatom-doped c-HBCs, enabling easy access to coronene-based PAHs with core and peripheral substitutions, as illustrated in Fig. 8 (**41–44**). The authors suggest that this strategy not only complements Nuckolls' approach but also broadens the scope of c-HBC chemistry. Ongoing efforts are focused on expanding the synthetic utility of this methodology, with the resulting nanographenes (NGs) continuing to find relevance in diverse applications.[148]

Müllen *et al.* (2015) demonstrated the precise synthesis of the CHBC-based macrocycle **47a**, as depicted in Fig. 9. By enlarging the macrocyclic ring size and strategically blocking reactive positions, they achieved selective formation of CHBCs while minimizing undesired strain-relieving side reactions. The successful application of the Scholl reaction further confirmed that graphenic sidewalls can be constructed within strained cyclic systems. As π-extension of the CHBC framework could yield carbon nanotube (CNT) sidewall segments, this post-synthetic approach presents a promising route toward bottom-up CNT fabrication. However, the significant ring strain associated with 15-membered macrocycles hindered complete and selective dehydrogenation, thus limiting scalability. Overcoming this limitation requires the development of sufficiently large and structurally robust polyphenylene macrocycles capable of undergoing quantitative conversion into fully conjugated graphenic sidewalls, which remains a critical challenge in the bottom-up synthesis of CNTs.[149]

Pal *et al.* (2016) explored a novel class of alkoxy-substituted HBC derivatives, resulting in the development of distinct liquid crystalline materials. These unsymmetrical HBCs were synthesized through the cyclodehydrogenation of the corresponding symmetrical hexa-phenylbenzene precursors, as illustrated in Fig. 10. At ambient temperature, the formation of well-organized columnar mesophases was observed. Specifically, **48** exhibited a Col_r phase characterized by *p*6*mm* symmetry, whereas **49** displayed a Col_h phase with *p*2*gm* lattice symmetry. In terms of photophysical properties, **48** emitted

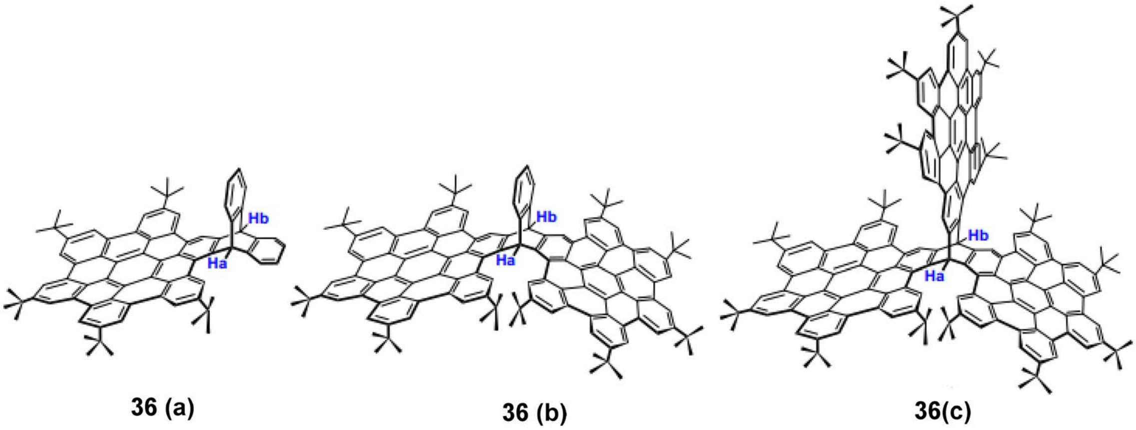

Fig. 7 Structure of HBCs-based triptycenes. Reproduced from ref. 146 with permission from Elsevier, Copyright © 2014.

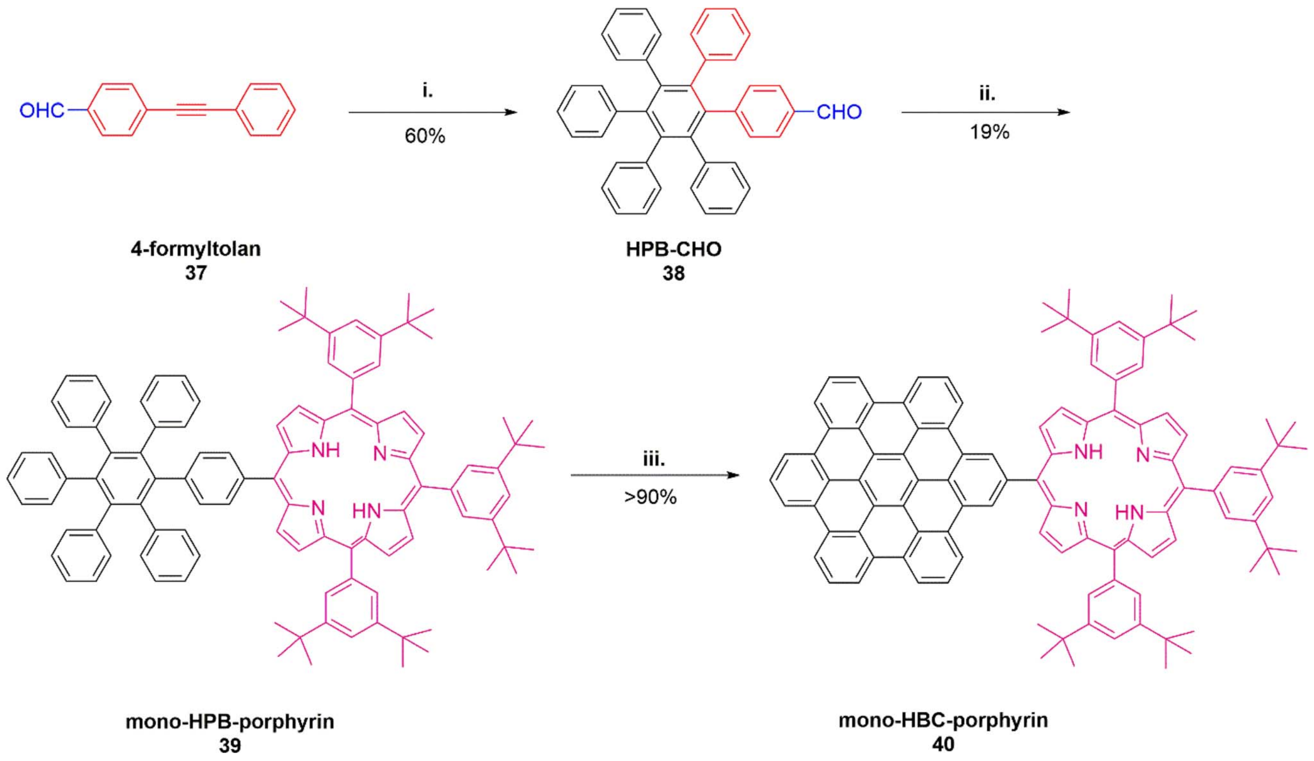

Scheme 3 Synthesis of HBC porphyrin using (i) 0.5 equiv. tetracyclone (ii) 1 equiv. 3,5-di-*tert*-butylbenzaldehyde, 3 equiv. pyrrole, trifluoroacetic acid (TFA), CH_2Cl_2 and DDQ 19% yield (iii) 16 equiv. dry $FeCl_3/CH_3NO_2$ (300 mg mL^{-1}), CH_2Cl_2, 0 °C, 2.5 h, >90% yield.[147]

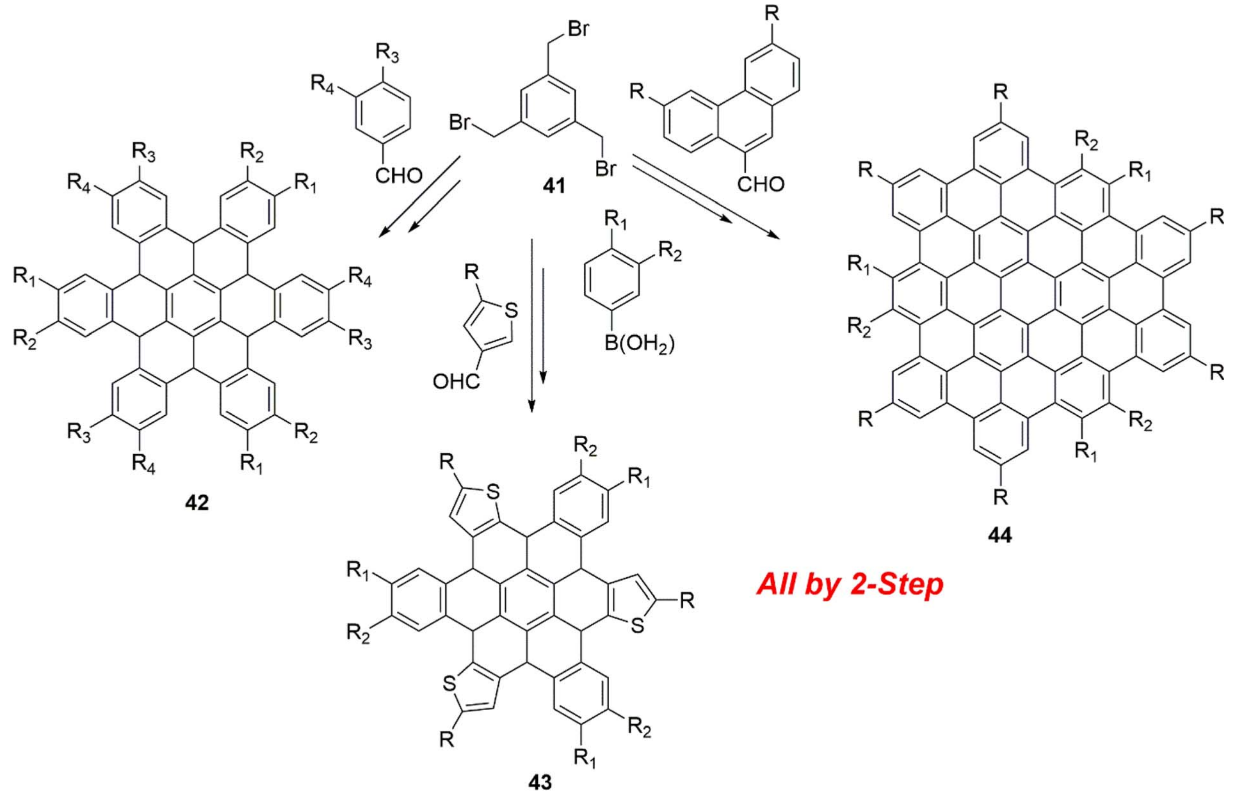

Fig. 8 Synthesis of c-HBC using CSA strategy.[148]

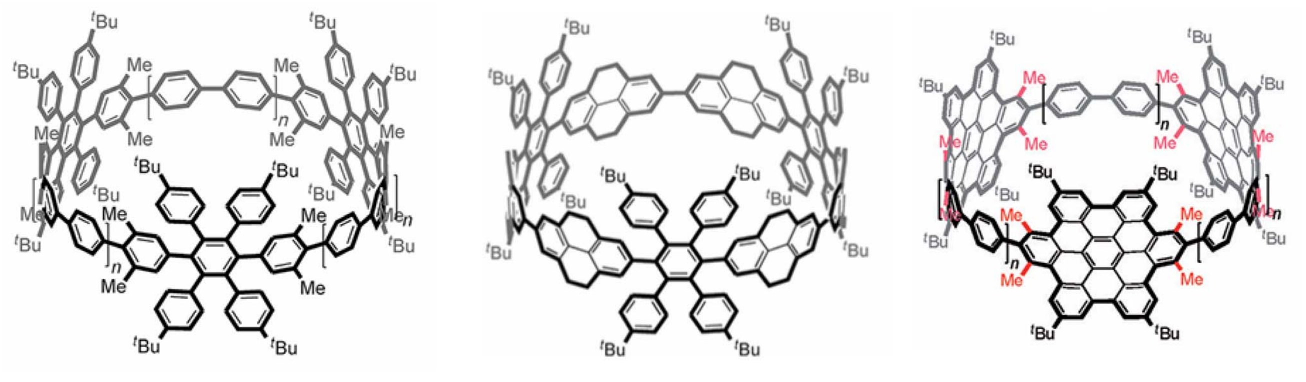

45 **46** **47**
47a n= 2

Fig. 9 Structural representation of phenylene-extended cyclic HBCs synthesized by using cyclodehydrogenation reaction. Reproduced from ref. 149 with permission from John Wiley & Sons, Copyright © 2015, Wiley-VCH Verlag GmbH & Co. KGaA, Weinheim.

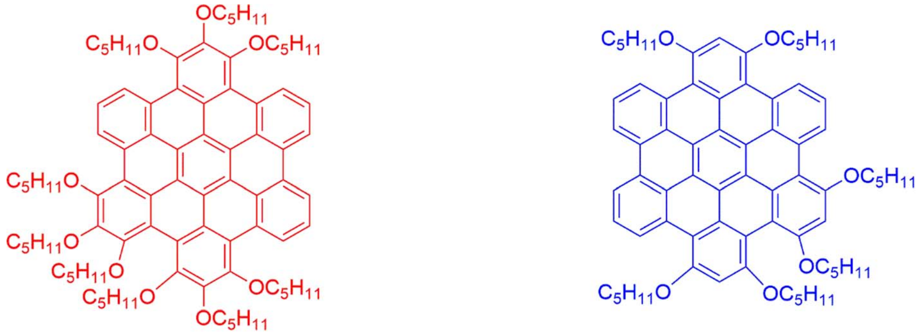

48 **49**

Fig. 10 Structures of HBC derivatives that were synthesized.[150]

reddish fluorescence in both solution and thin-film states, while **49** showed yellowish-green fluorescence under the same conditions.[150]

Narita *et al.* (2016) investigated two distinct synthetic strategies for constructing a series of HBC–acceptor dyads incorporating electron-deficient units such as 9,10-anthraquinone, naphthalene-1,8-dicarboximide, and perylene-3,4-dicarboximide (**50–52**). These approaches involved introducing the acceptor moieties either before or after the cyclodehydrogenation of the hexabenzocoronene core, as depicted in Fig. 11. The resulting dyads exhibited varying extents of intramolecular charge-transfer interactions, alongside tunable optical, electrochemical, and liquid-crystalline properties, which were dependent on the specific acceptor units employed. These results highlight the potential of molecular design to tailor the optoelectronic behavior of nanographene systems through strategic acceptor integration. Furthermore, the synthetic methodologies developed enable access to larger nanographene architectures and graphene nanoribbons, facilitating the creation of advanced nanographene–acceptor hybrids.[151]

Bonifazi *et al.* (2017) reported the first successful synthesis of a soluble hexabenzoborazine-based nanocarbon (HBBNC) *via* a planarization strategy employing a Friedel–Crafts-type reaction, as outlined in Scheme 4 (**53–59**). The process commenced with a hexafluoroborazine precursor, wherein six C–C bonds were simultaneously formed to achieve the fully conjugated structure. Single-crystal X-ray diffraction confirmed the presence of an inner B_3N_3 ring featuring notably short B–N bond lengths, indicative of a highly conjugated system. This novel class of B_3N_3-doped hybrid nanographenes exhibited characteristic photophysical properties, including strong UV absorption, blue-violet singlet emission, and green phosphorescence—features in good agreement with theoretical predictions. The development of this synthetic route represents a key advancement in the field of heteroatom-doped graphene derivatives, offering precise control over doping patterns. These findings not only enhance the understanding of the optoelectronic behavior of BN-doped nanographenes but also open new pathways for designing functional materials for advanced applications in materials science and nanotechnology.[152]

Shinokubo *et al.* (2017) investigated the synthesis of *cis*- and *trans*-dicyanoethene-bridged HBC dimers through the oxidative coupling of a dicyanomethyl-substituted HBC anion, as depicted in Fig. 12 (**60a** and **60b**). These dimers displayed photoinduced *cis–trans* isomerization in solution. Furthermore, the

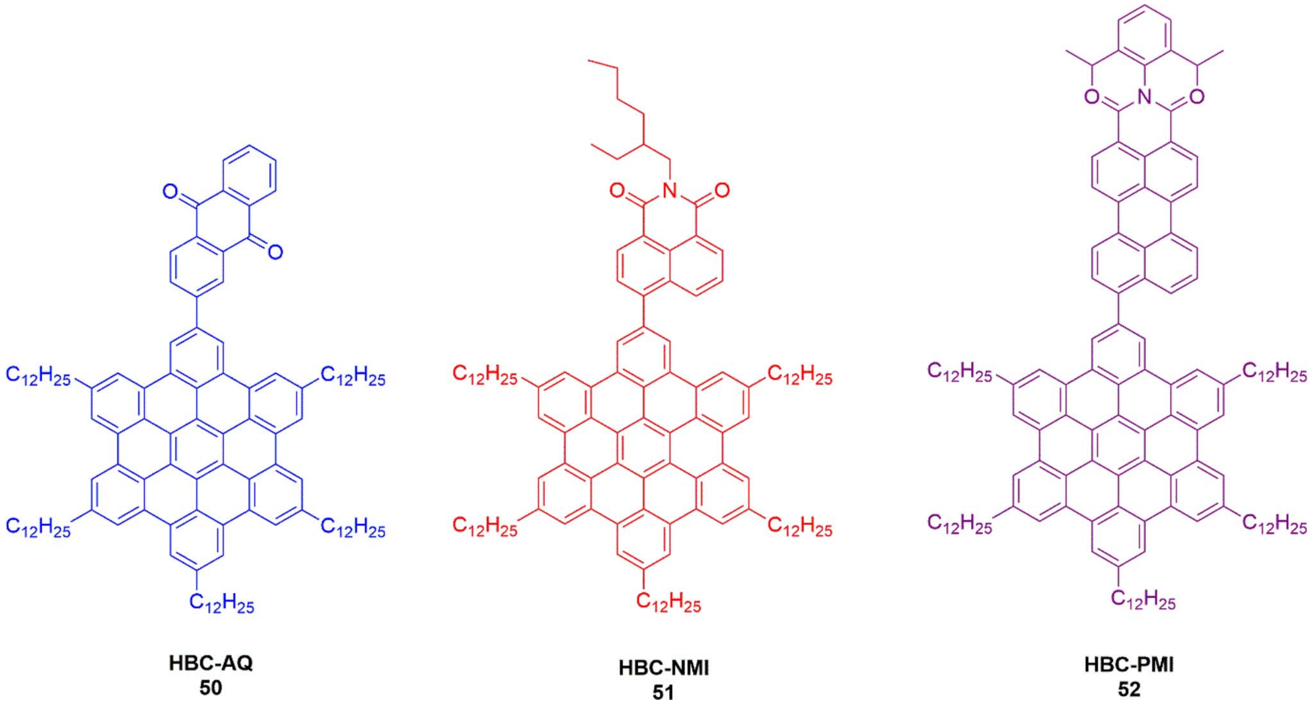

Fig. 11 Molecular representation of HBC-AQ, -NMI, and -PMI.[151]

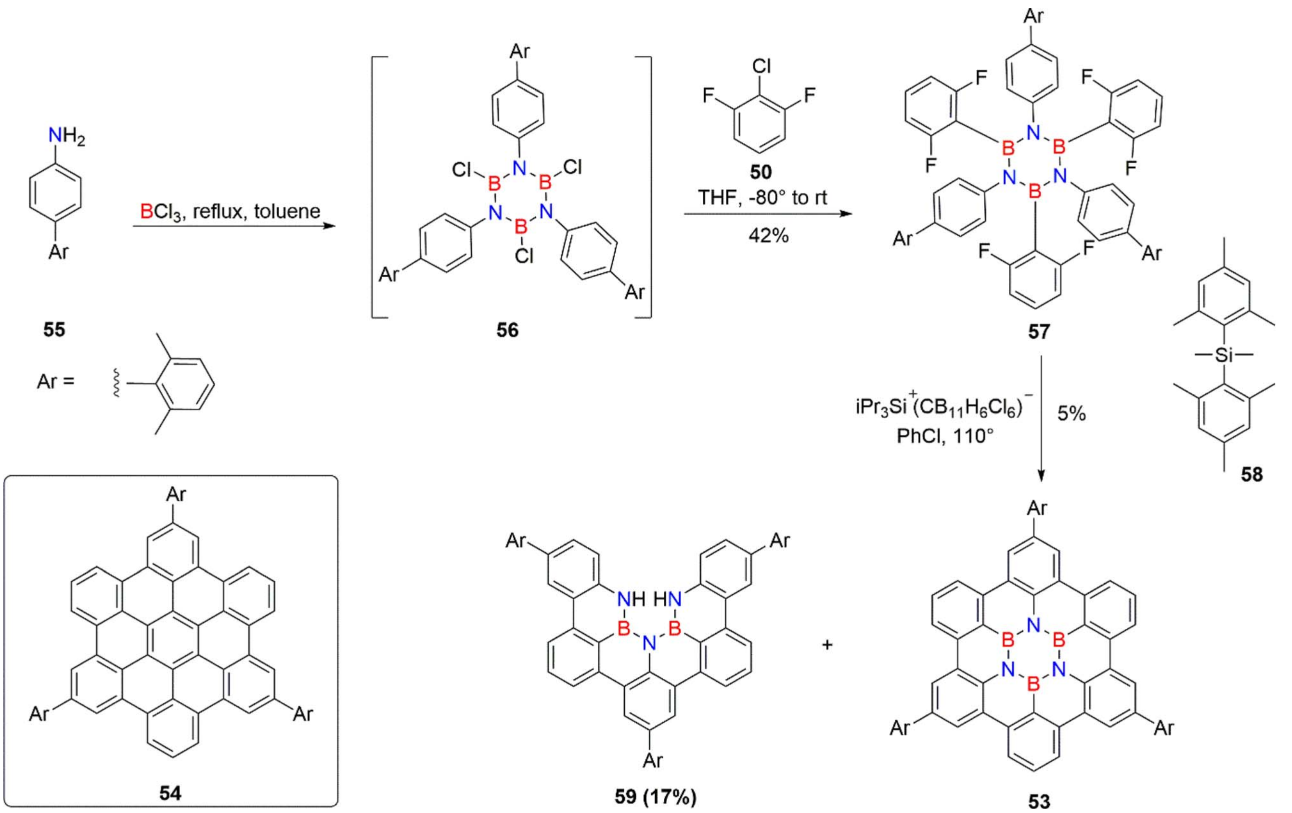

Scheme 4 Synthetic route for xylyl-substituted HBBNC **53**; full-carbon congener.[152]

electronic modulation of the HBC moieties facilitated S_1–S_0 transitions, producing intense red fluorescence in both solution and solid states. These findings highlight the potential of dicyanomethyl and dicyanoethene functionalities to enhance the photophysical properties of carbon-rich systems, including graphene quantum dots. Current efforts are aimed at extending

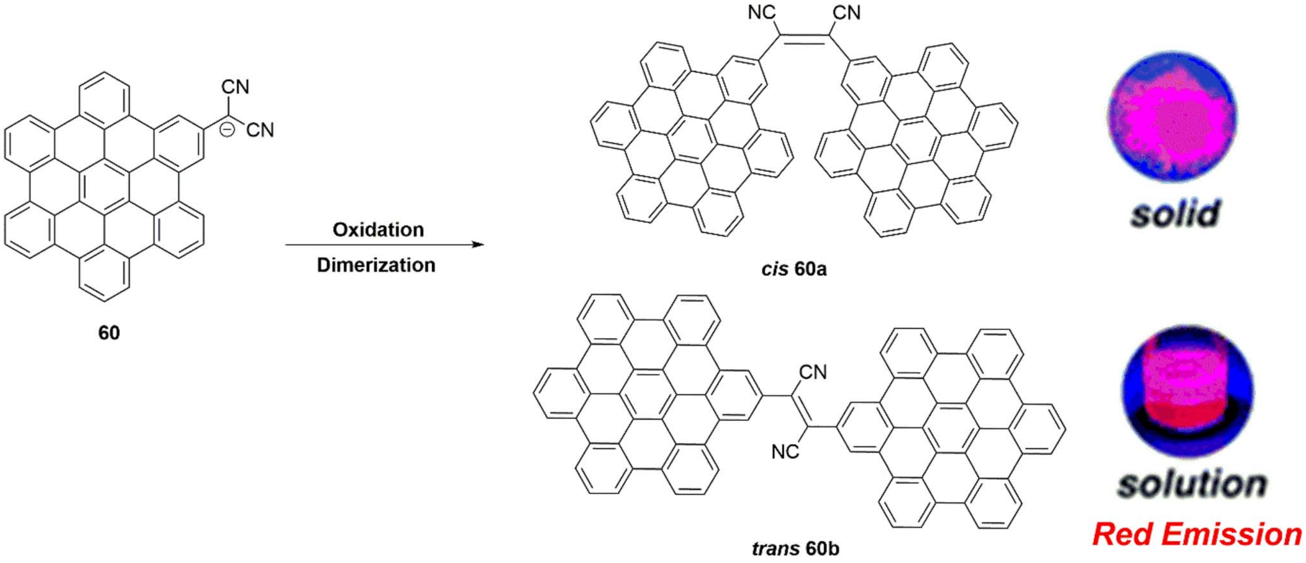

Fig. 12 Synthesis of dicyanomethyl HBC dimers. Reproduced from ref. 153 with permission from the Royal Society of Chemistry.

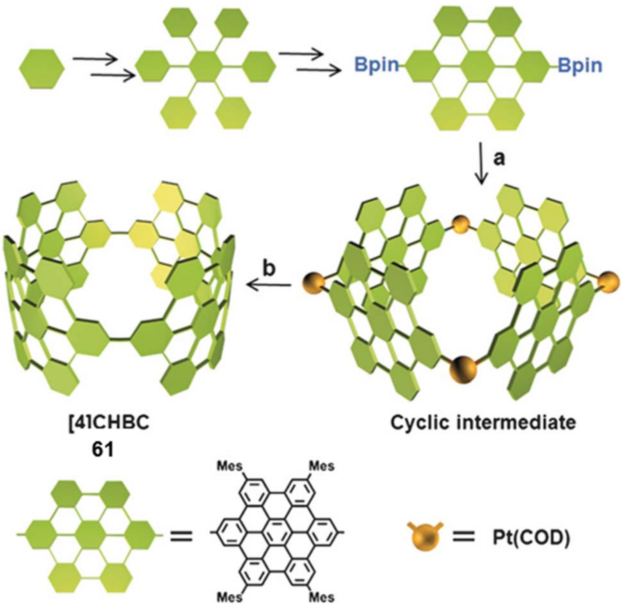

Fig. 13 Synthetic strategy for [4]CHBC. Reproduced from ref. 154 with permission from John Wiley & Sons, Copyright © 2017, Wiley-VCH Verlag GmbH & Co. KGaA, Weinheim.

this design strategy to more complex and larger nanocarbon architectures.[153]

Du *et al.* (2017) reported the successful synthesis of a π-extended carbon nanoring, designated as [4]CHBC, *via* a platinum-catalyzed reductive elimination strategy, as illustrated in Fig. 13 (**61**). The resulting [4]CHBC exhibited distinct optoelectronic features, including characteristic absorption and fluorescence properties. Preliminary studies on its host–guest interactions revealed the formation of a 1 : 1 complex with C_{70} fullerene, indicating promising supramolecular behavior. Due to its structural attributes, [4]CHBC serves as a valuable molecular segment for the bottom-up construction of structurally uniform carbon nanotubes (CNTs). The research group is also actively exploring related challenges, such as the synthesis of CNTs with controlled diameters and the design of highly conjugated carbon nanorings that emulate extended CNT fragments.[154]

Narita *et al.* (2018) demonstrated the efficient synthesis of a spirobifluorene-bridged HBC (SB-HBC, **62**), incorporating a robust spiro-linkage, as depicted in Fig. 14. The resulting SB-HBC exhibited reversible redox behavior, undergoing both reduction and chemical oxidation to yield stable oxidized species. This study highlights the development of π-extended spirobifluorene-based nanographenes with modified optical and electronic properties, offering a promising platform for the exploration of spiro-fused nanographene architectures.[155]

Fan *et al.* (2018) synthesized a series of four disc-cube triads, each consisting of a central HBC core connected to two polyhedral oligomeric silsesquioxane (POSS) units *via* either amide or ester linkages, as illustrated in Fig. 15 (**63A–E** and **64A–E**). The self-assembly behavior of these triads, incorporating spacers of different lengths, was systematically investigated at

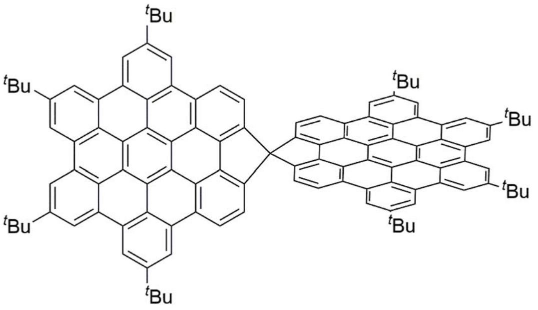

62

Fig. 14 Structural representation of spiro-fused bis-HBC (SB-HBC).[155]

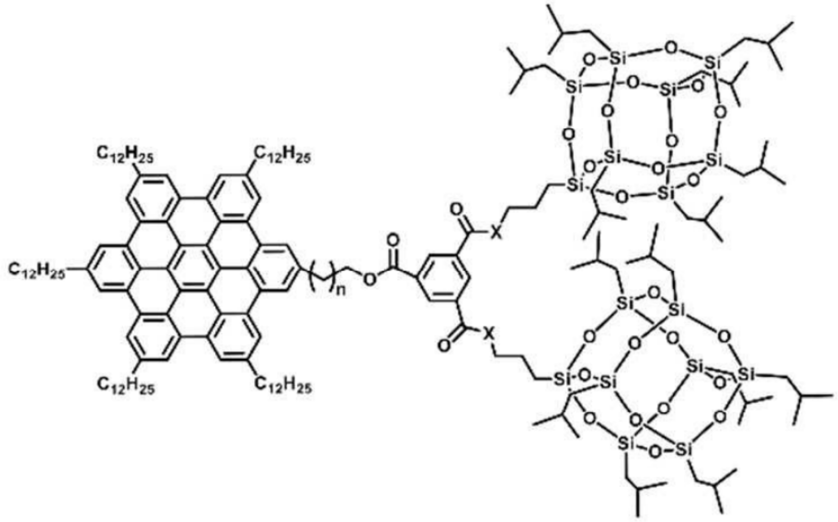

HBC-C4-2POSS-COO (**63-E**) n = 3 X= O
HBC-C4-2POSS-NH (**63-A**) n = 3 X= NH
HBC-C11-2POSS-COO (**64-E**) n = 10 X= O
HBC-C11-2POSS-NH (**64-A**) n = 10 X= NH

Fig. 15 Structural representation of four triads. Reproduced from ref. 156 with permission from the Royal Society of Chemistry.

varying temperatures using techniques such as wide-angle X-ray scattering (WAXS), two-dimensional wide-angle X-ray diffraction (2D WAXD), polarized light microscopy (PLM), and transmission electron microscopy (TEM). All four triads exhibited columnar hexagonal Col_h mesophases at elevated temperatures, regardless of the type of linkage connecting the POSS units.[156]

Jux *et al.* (2020) synthesized two distinct HBC–tetrabenzoporphyrin (TBP) conjugates, designed with varying points of connectivity: one incorporating a maleimide linker at the TBP periphery and the other involving direct *meso*-position attachment, as shown in Fig. 16 (**65**, **66**). The synthetic route for both dyads involved intramolecular oxidative cyclodehydrogenation following the introduction of the corresponding HBC precursor. Especially, the Scholl reaction proceeded with near-quantitative efficiency and minimal side reactions such as chlorination or decomposition, affording isolated yields of 56% and 29% for the respective conjugates. Upon photoexcitation, both dyads exhibited efficient energy transfer from the HBC unit to the TBP core, consistent with prior studies on π-extended porphyrin systems. Preliminary findings indicate that both the mode of connectivity and the extent of π-conjugation significantly influence their light-harvesting properties. Specifically, the *meso*-linked HBC–TBP conjugate demonstrated approximately 20% greater absorptivity compared to HBC–porphyrin, while the N-HBC–phthalimidoporphyrin analogue showed a further 10% increase. These results highlight the potential of these conjugates as promising candidates for artificial light-harvesting systems, capable of covering a broad spectral range from near-ultraviolet to near-infrared.[157]

Jux *et al.* (2020) developed an innovative approach for synthesizing a twisted nanographene featuring a helical motif

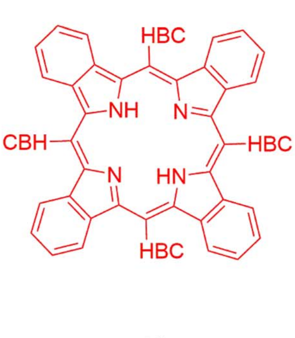

65

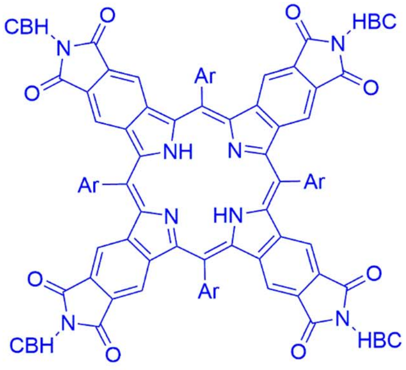

66

Fig. 16 Structural representation of HBC tetrabenzoporphyrin architectures.[157]

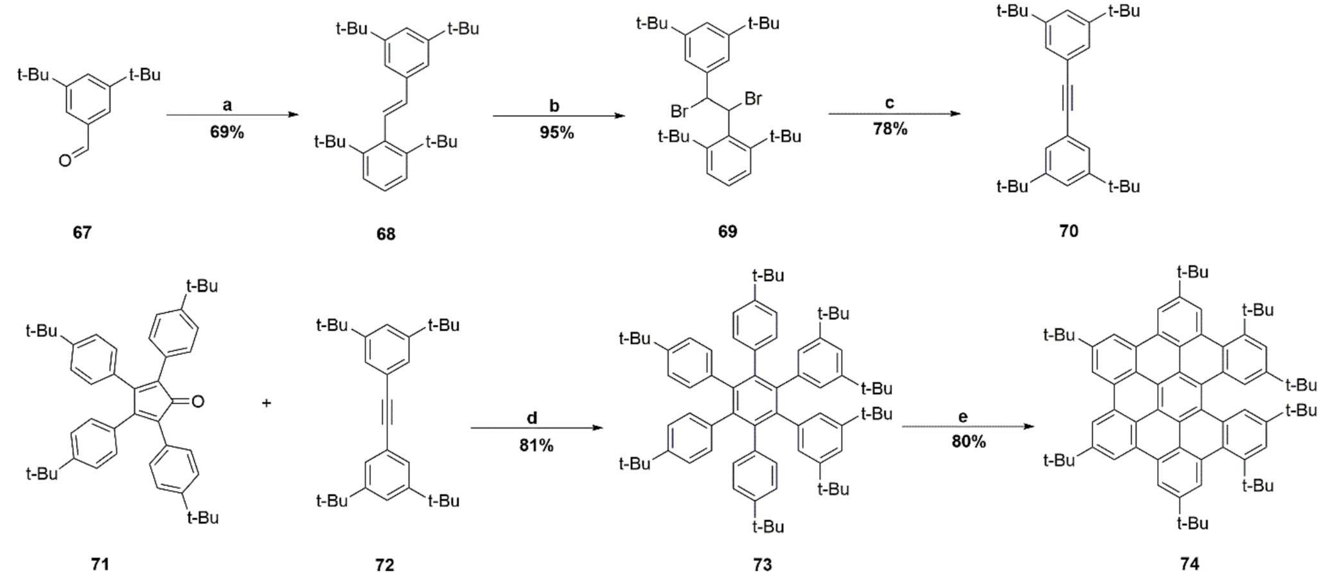

Scheme 5 Synthesis of HBC-based helicene. (a) Zn, TiCl$_4$, THF, 70 °C, 22 h; (b) Br$_2$, CHCl$_3$, rt, 30 min; (c) KO*t*Bu, THF, 0 °C, 20 min; (d) Ph$_2$O, 260 °C in microwave reactor, 12 h; (e) FeCl$_3$, CH$_3$NO$_2$, CH$_2$Cl$_2$, 0 °C, 100 min.[158]

derived from a HBC core (**67–74**), as illustrated in Scheme 5. The strategy involved the incorporation of sterically bulky substituents to prevent complete planarization during the oxidative cyclodehydrogenation step, thereby inducing helicity in the resulting π-system. These findings are consistent with previous work by the authors, where the formation of nitrogen-doped, helicene-like HBC structures was governed primarily by electronic effects. Current efforts are focused on the enantioselective separation and detailed chiroptical characterization of the helical nanographene, as well as exploring its potential as a versatile scaffold for constructing advanced hybrid materials. This includes the development of functional systems analogous to previously reported porphyrin–HBC conjugates.[158]

Hirsch *et al.* (2021) reported the synthesis and characterization of the first π-extended aza-helicene, **77**. This molecule was constructed by *ortho*-fusing two naphthalene diimide (NDI) units onto HBC core *via* a benzimidazole linker, as depicted in Scheme 6 (**75–77**). The resulting structure constitutes a fully conjugated diaza[7]helicene, representing a novel helical hybrid with substantial lateral π-extension of the helicene framework. Among the three theoretically possible enantiomeric isomers anticipated following the final Scholl oxidation, only the 7-helical HBC-based isomer was isolated, indicating a pronounced stereoselectivity favoring a single stereoisomer. Ongoing work aims to optimize the Scholl reaction conditions to improve the yield of the target helical product while minimizing side reactions related to the hexaphenylbenzene (HPB) precursor. Furthermore, this molecular scaffold holds promise for the design of novel chiral nanotweezers incorporating extended ryleneimide units, such as perylene diimide, facilitating the development of supramolecular architectures with rigid, expanded π-conjugated surfaces.[159]

An *et al.* (2023) synthesized helical nanographenes derived from Seco-HBC featuring a secondary amine at the periphery, which served as a reactive site for functionalization of the nanographene core, as illustrated in Fig. 17 (**78**, **79**). The helical conformations and the presence of *P* and *M* enantiomers were confirmed by single-crystal X-ray diffraction analysis. This study

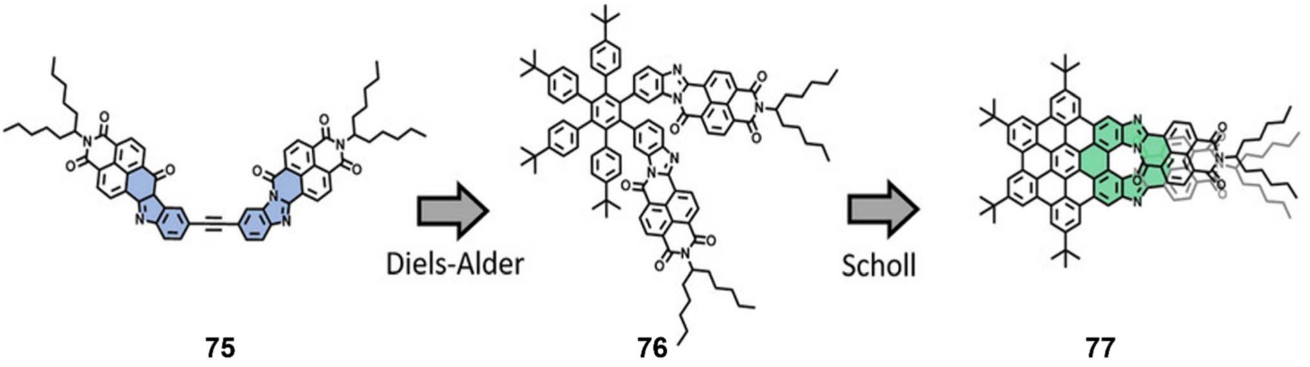

Scheme 6 Synthetic approach for synthesis of 7-helical HBC. Reproduced from ref. 159 with permission from John Wiley & Sons, Copyright © 2021, Wiley-VCH Verlag GmbH & Co. KGaA, Weinheim.

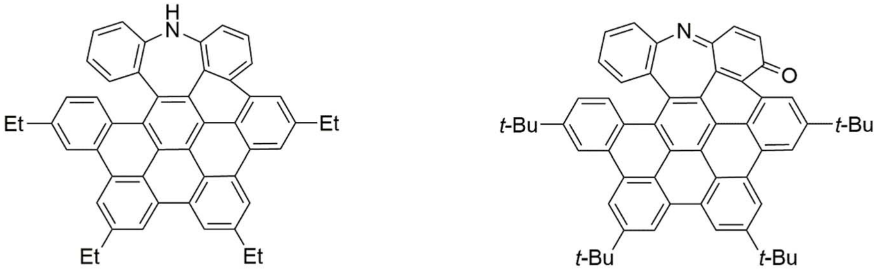

78 **79**

Fig. 17 Azepine-embedded seco-HBC-based helix nanographenes.[160]

demonstrates that the reactive NH group enables rational modification of the nanographene core. Notably, attachment of a phenyl substituent at the NH position in the non-emissive nanographene **78** significantly enhanced both quantum yield and fluorescence intensity, with the substituent's electronic and emissive properties allowing fine-tuning of photophysical behavior. Furthermore, the benzoic acid-functionalized derivative **79** exhibited sufficient brightness and cell membrane permeability for effective live-cell imaging applications.[160]

An *et al.* (2024) developed a novel series of nitrogen-doped nanographenes (**80–84**) through the selective π-extension of nitrogen-doped HBC, as depicted in Scheme 7. DFT calculations revealed that the π-extended structures adopt a unique three-dimensional conformation featuring a π-conjugated concave surface. Investigations into the electronic properties and aromaticity indicated an uneven electron density distribution and the presence of localized antiaromatic regions within the nanographene framework. Due to the large concave π-surface and electron-rich character, supramolecular interactions and electron transfer processes between the nanographene and C_{60} were evaluated. This study demonstrates that regioselective π-extension enables access to curved polyaromatic architectures with diverse geometries and electronic features.[161]

2.2. Recent advancements in HBCs synthesis

Chen *et al.* (2015) investigated a series of HBC derivatives characterized by reduced molecular symmetry and deviations

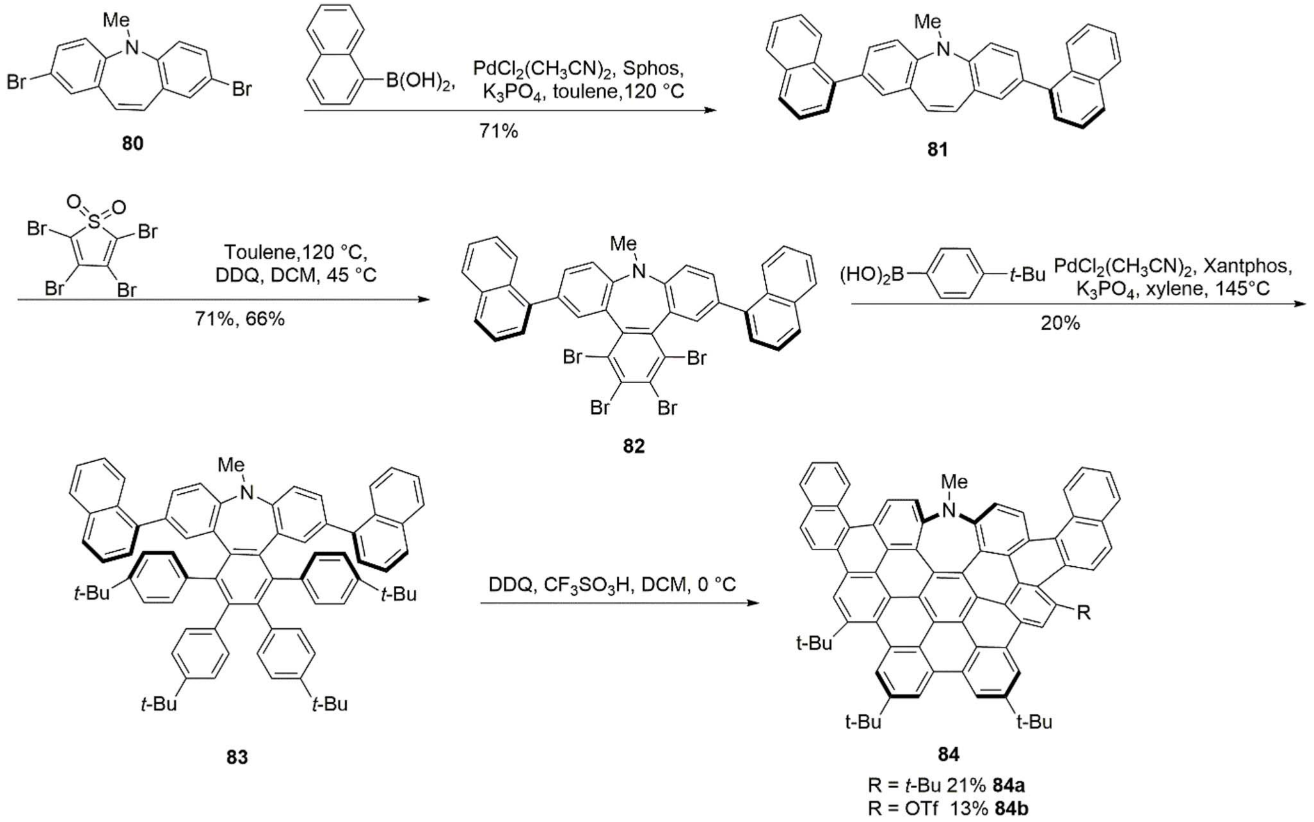

Scheme 7 Synthesis of aza-nanographenes **84a** and **84b**.[161]

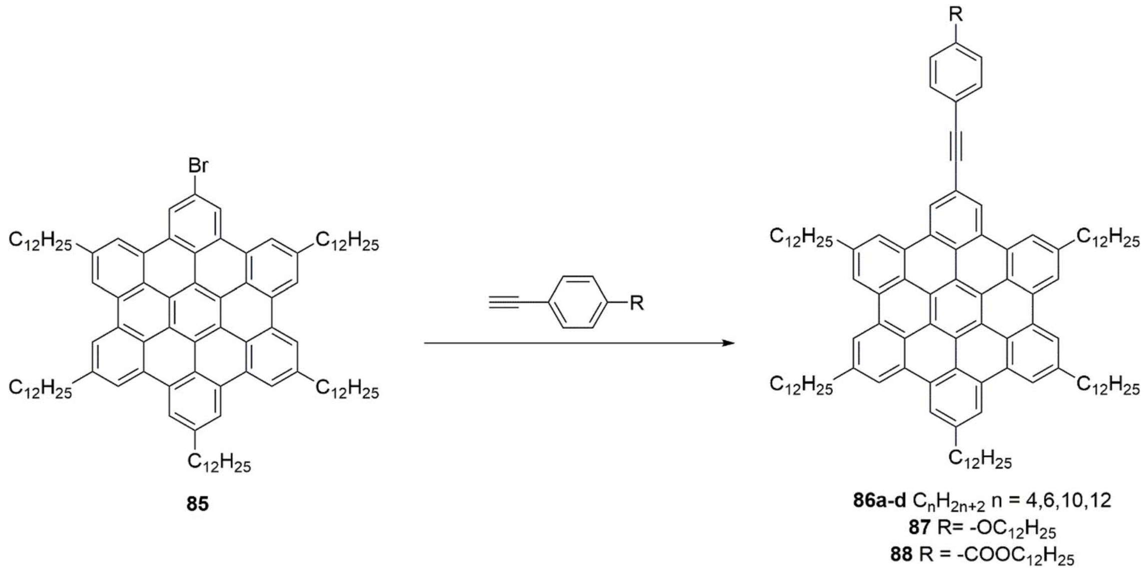

Scheme 8 Sonogashira coupling reaction producing hexabenzocoronene derivatives **85–88**.[162]

from ideal disc-like geometry, factors that typically impede efficient molecular packing. Utilizing mono-bromo-substituted HBC (HBC-Br) as a reactive intermediate, they synthesized various novel functionalized HBC derivatives through Sonogashira cross-coupling, as illustrated in Scheme 8 (**85–88**). This functionalization strategy resulted in a notable decrease in the melting points of the target compounds. Furthermore, the incorporation of distinct protruding substituents enhanced intermolecular interactions, leading to an expanded and more stable mesophase temperature range. Additionally, this approach effectively mitigated thermal degradation. These results indicate that this functionalization methodology holds

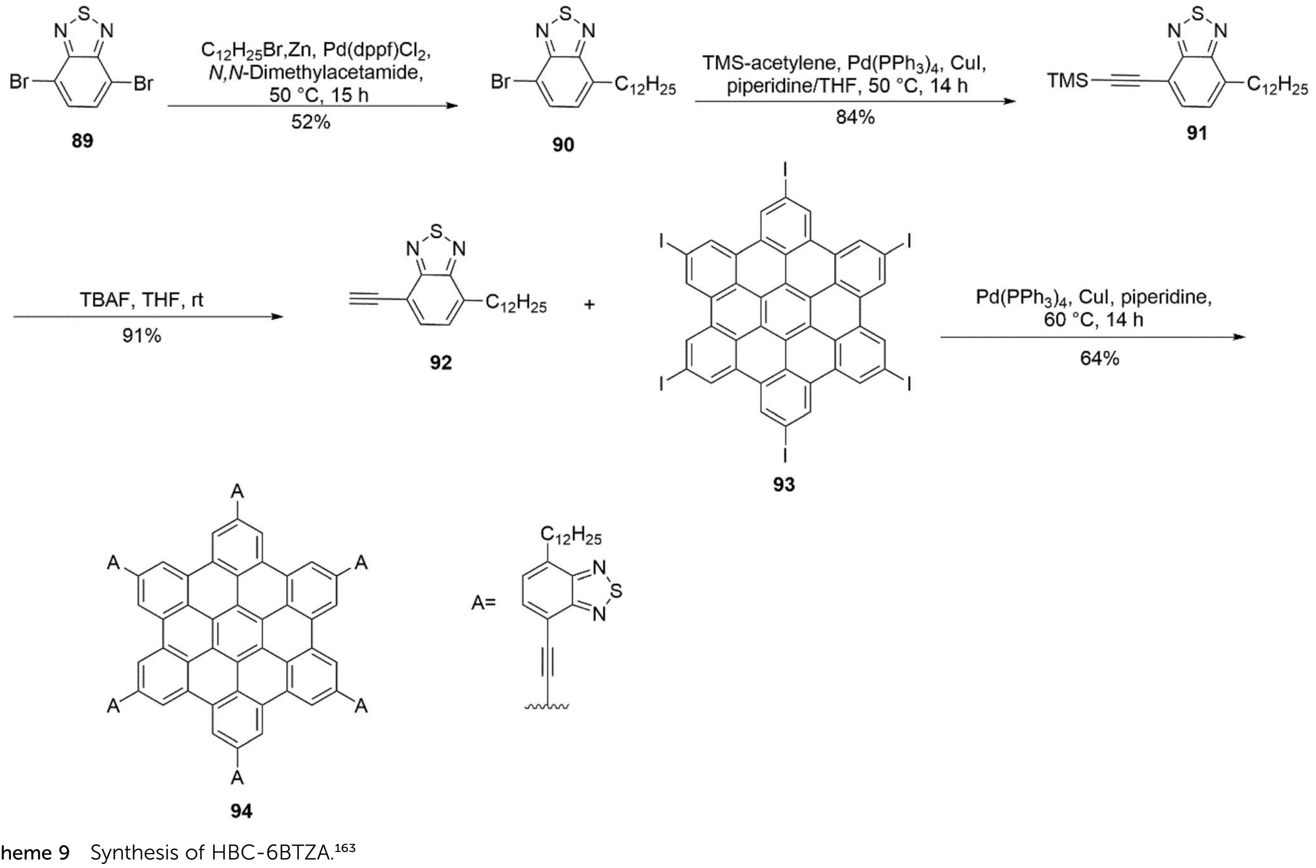

Scheme 9 Synthesis of HBC-6BTZA.[163]

potential for application to other discotic columnar liquid crystalline systems, offering a viable route toward the development of thermally stable materials suitable for advanced processing and device integration.[162]

Narita *et al.* (2017) developed a novel donor–acceptor system by functionalizing the periphery of HBC core with six benzothiadiazole (BTZ) units connected *via* ethynylene linkers, as depicted in Scheme 9 (**89–94**). DFT calculations indicated that the rigid triple bonds effectively reduced torsional distortions between the HBC core and BTZ moieties, resulting in a predominantly planar molecular framework. The incorporation of electron-deficient BTZ acceptor groups enabled precise modulation of the electronic properties. Optical studies, including UV-visible absorption and fluorescence spectroscopy, revealed distinct spectral features, with absorption and emission peaks observed at 424 nm and 650 nm, respectively. These results demonstrate that the electronic characteristics of HBC derivatives can be systematically tuned by integrating strong acceptor units through rigid π-conjugated linkers.[163]

Shinokubo *et al.* (2017) successfully synthesized tetracyanoethylene-bridged HBC dimers **96** and **98** *via* the oxidation of dicyanomethyl-substituted HBC precursors **95** and **97**, as illustrated in Scheme 10. These HBC oligomers exhibited notable near-infrared (NIR) mechanochromic behavior. Electron spin resonance (ESR) measurements confirmed the formation of highly stable radical species, which persisted for extended periods following mechanical grinding. The observed mechanochromic NIR absorption and long-lived colored states (exceeding four months) highlight the potential application of these materials in optoelectronic devices such as molecular memory and switching systems. These results demonstrate that the incorporation of dicyanomethyl groups into PAHs imparts stimuli-responsive properties, enabling dynamic control over their π-conjugated frameworks.[164]

Lein *et al.* (2018) investigated the site selectivity of the $[\mathrm{RuCp^*}]^+$ complex on hexa-*tert*-butyl-substituted HBC **99**, focusing on the interplay between steric hindrance from bulky *tert*-butyl groups and electronic factors, as depicted in Fig. 18.

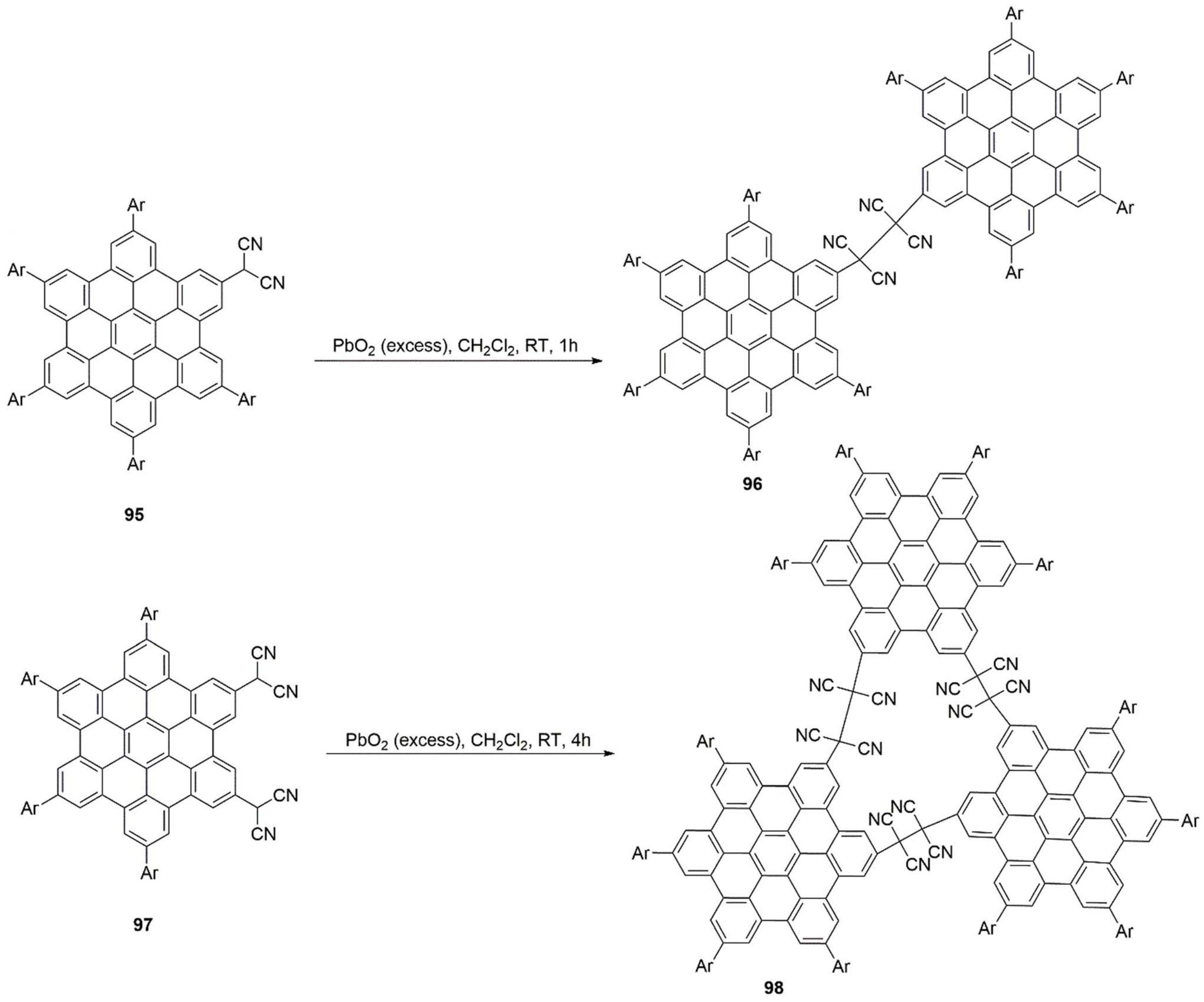

Scheme 10 Synthesis of tetracyanoethylene-bridged HBC dimer and trimer.[164]

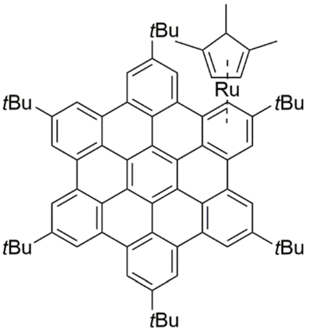

99

Fig. 18 Structure of the Ru^{II} sandwich complex with hexa-*tert*-butyl HBC.[165]

Despite the significant steric congestion near the peripheral aromatic rings, the reaction preferentially occurs at these sites. Potential energy surface scans indicated that this steric crowding does not impose an energetic penalty. Contrary to previous assumptions, the study revealed that ruthenium selectively coordinates to the aromatic ring exhibiting the highest electron density rather than the most aromatic site. Further analysis of related systems with varied substitution patterns supported this conclusion, emphasizing the dominant role of electronic effects over steric factors in determining the regioselectivity of $[RuCp^*]^+$ binding.[165]

Müllen *et al.* (2021) successfully synthesized two dicyclopenta-fused hexabenzocoronenes (PHBCs), namely *m*PHBC and *p*PHBC, with the latter generated *in situ*, as illustrated in Scheme 11 **100–114.** Their synthetic strategy involved the incorporation of a pair of preinstalled fluorenyl groups as key intermediates during the cyclodehydrogenation of appropriately designed precursors. Combined DFT calculations alongside variable-temperature NMR and EPR analyses revealed that both PHBC isomers possess a distinctive singlet biradical ground state. The pronounced singlet biradical character of the PHBCs is attributed to the high spin density partially localized at the methine carbons, while the overall benzenoid framework is locally preserved. This design principle, informed by comparisons to other fully benzenoid PAHs reported in the literature, offers a promising route to access novel cyclopenta-fused PAHs. Such compounds hold potential applications in quantum information science, optoelectronic devices, and spintronic technologies.[166]

Fan *et al.* (2022) reported the synthesis of two novel organic–inorganic hybrid molecules incorporating a central HBC core functionalized with two oligo(dimethylsiloxane) (ODMS) side chains exhibiting C_2 symmetry. These compounds, designated *p*-HBC-4Si$_7$ and *p*-HBC-6Si$_7$, were prepared *via* esterification, as depicted in Scheme 12 **115–117.** The synthetic approach utilized the previously reported intermediate *p*-HBC-2C$_{11}$OH, along with ODMS-containing carboxylic acid derivatives, 2Si$_7$-COOH and 3Si$_7$-COOH, which were synthesized through hydrosilylation followed by benzyl group deprotection. This methodology successfully afforded HBC-based organic–inorganic block molecules, providing promising candidates for applications in soft matter and supramolecular assemblies.[167]

Hirsch *et al.* (2023) investigated the synthesis and optoelectronic properties of nine π-extended monosubstituted derivatives of 5,8,11,14,17-pentakis-(*tert*-butyl)-HBC derivatives **118–126.** The synthetic route began with 2-iodo-5,8,11,14,17-pentakis-(*tert*-butyl)-HBC, which underwent a Sonogashira coupling with ethynyltrimethylsilane, as illustrated in Fig. 19. This acetylene-functionalized intermediate acted as a versatile platform for further Sonogashira couplings with a range of aryl substituents. The derivatives included various electron-withdrawing groups such as nitriles, pyridines, and carbonyl-based moieties, including aldehydes, methyl esters, and carboxylic acids. Additionally, three quinoxaline-based frameworks—diphenylquinoxaline, dibenzo[*a*,*c*]phenazine, and phenanthro[4′,5′-*a*,*b*,*c*]phenazine—were synthesized. UV-Vis absorption spectra revealed redshifts up to 7 nm compared to the parent iodo-HBC, indicative of enhanced π-conjugation and modified electronic structures. Especially, phenanthro[4′,5′-*a*,*b*,*c*]phenazine substitution resulted in a pronounced decrease in absorption intensity. Fluorescence studies showed that most derivatives preserved the typical HBC emission profile, whereas substitution with dibenzo[*a*,*c*]phenazine and phenanthro[4′,5′-*a*,*b*,*c*]phenazine produced broad, featureless emission bands, highlighting substantial alterations in the photophysical characteristics of the π-system. These results demonstrate the significant impact of substituent variation on the electronic and emissive behavior of HBC-based compounds.[168]

Kriegel *et al.* (2023) performed a comparative investigation into the photodoping properties of indium tin oxide (ITO) nanocrystals (NCs) and a hybrid system comprising ITO NCs integrated with graphene quantum dots (GQDs) functionalized with HBC–AOM units, as illustrated in Scheme 13 (**127–135**). The study demonstrated that photodoped electrons in the hybrid material exhibit significantly enhanced stability. Time-resolved absorption spectroscopy under extended UV illumination revealed that maximal electron accumulation in the ITO NCs occurs only when the oxidation of GQDs effectively neutralizes the photoinduced holes generated within the NCs. These findings emphasize the essential function of hole scavengers in preserving charge neutrality throughout the photodoping process. Moreover, the results highlight the potential of coupling electron-donating GQDs with metal oxide nanocrystals to improve the performance of light-driven charge storage systems. The authors further suggest that embedding redox-active groups into the GQD structure could facilitate reversible and repeatable photodoping, thereby advancing the development of next-generation optoelectronic energy storage devices.[169]

Hirsch *et al.* (2023) described the synthesis of a series of novel mono-, di-, tri-, tetra-, and hexafluorinated HBC derivatives and their subsequent transformation into corresponding thioether-functionalized analogs (**136–144**), as depicted in Scheme 14. To markedly shorten reaction durations, a microwave-assisted substitution method using appropriate thiolates was employed. It was found that the molar extinction coefficients of the HBC derivatives decreased progressively with increasing fluorination and thioether substitution levels.

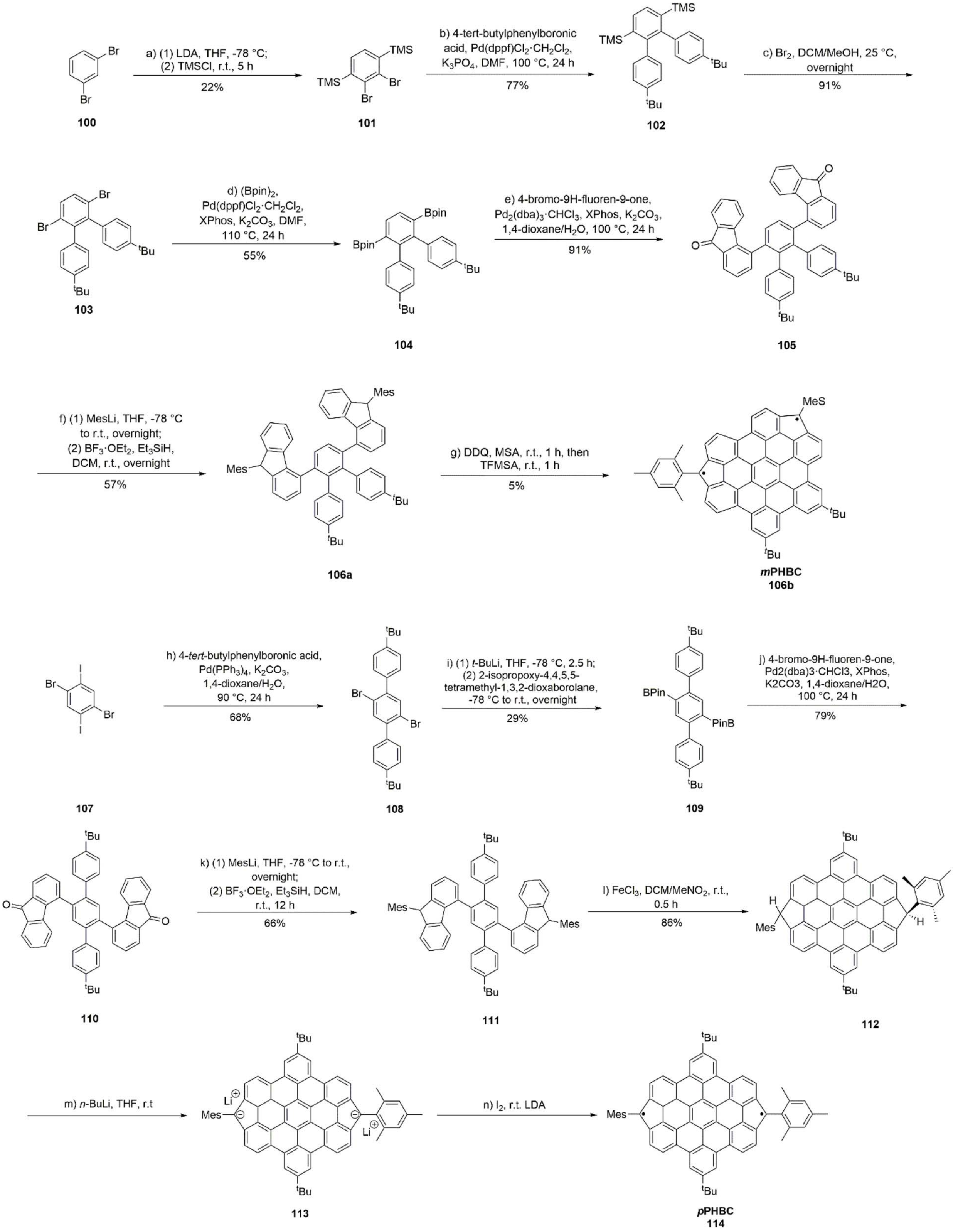

Scheme 11 Synthesis of *m*PHBC (A) and *p*PHBC.[166]

Although the specific identity of the thioether substituents had negligible influence on the optoelectronic properties, the incremental addition of thioether groups induced a bathochromic shift in both absorption and emission spectra. Further tuning of the HBC core's electronic environment was achieved by oxidizing thioethers to sulfones, followed by the

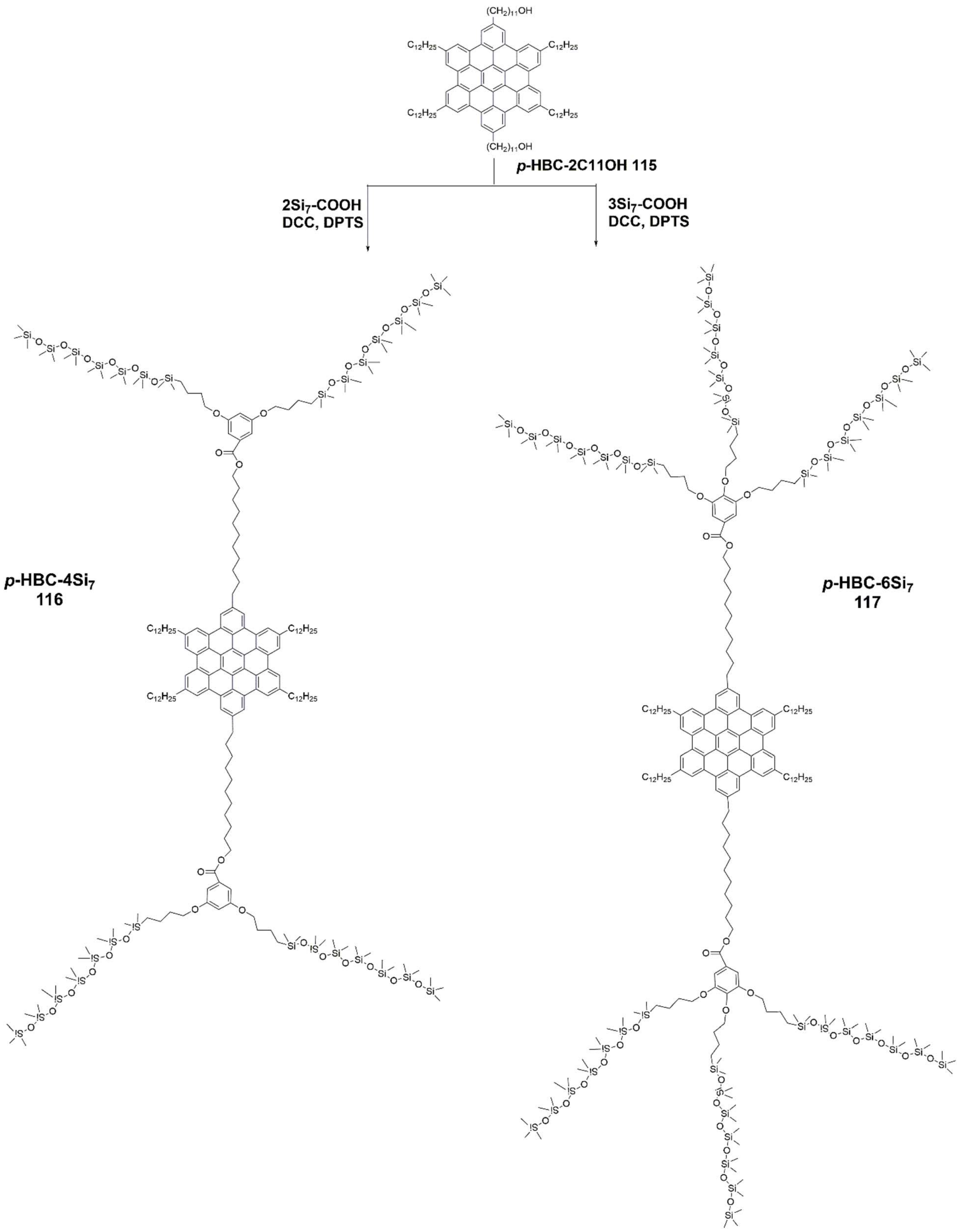

Scheme 12 Synthesis of p-HBC-4Si$_7$ **116** and p-HBC-6Si$_7$ **117**.[167]

preparation of sulfonium salts. This oxidation converted the electron-donating thioether moieties into electron-withdrawing substituents at the molecular periphery, resulting in broadened absorption and emission bands accompanied by diminished extinction coefficients, reflecting significant electronic modulation of the HBC framework.[170]

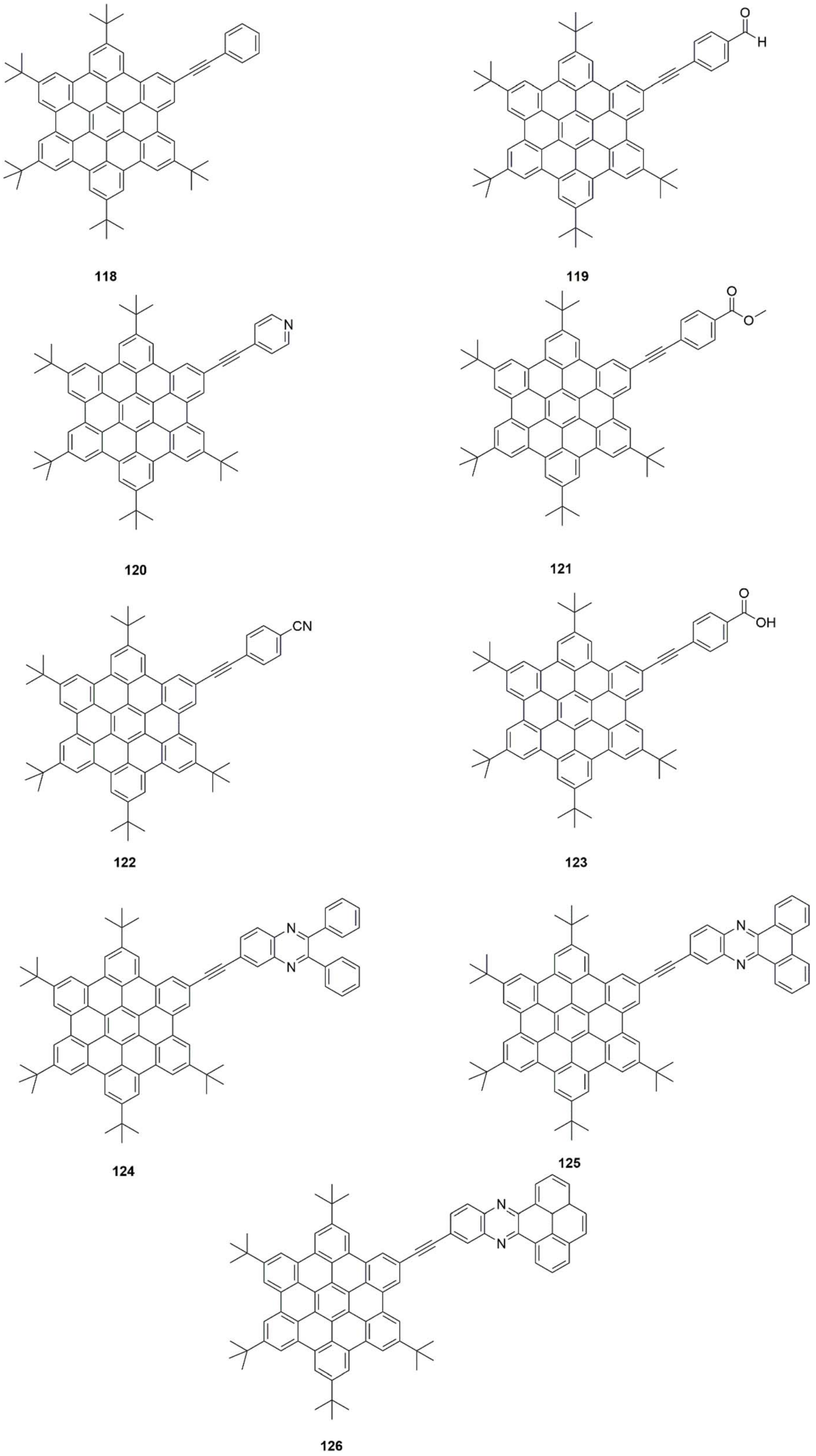

Fig. 19 Chemical structures of functional HBC–alkyne by Sonogashira coupling reaction.[168]

Gordon *et al.* (2023) reported the synthesis and photophysical characterization of a novel dppz-functionalized HBC (dppz-HBC) ligand and its corresponding metal complexes with $ReCl(CO)_3$ and $[Ru(bpy)_2]^{2+}$, as detailed in Scheme 15 (**145–154**). DFT calculations indicated the existence of a delocalized charge-transfer state encompassing both the HBC core and the

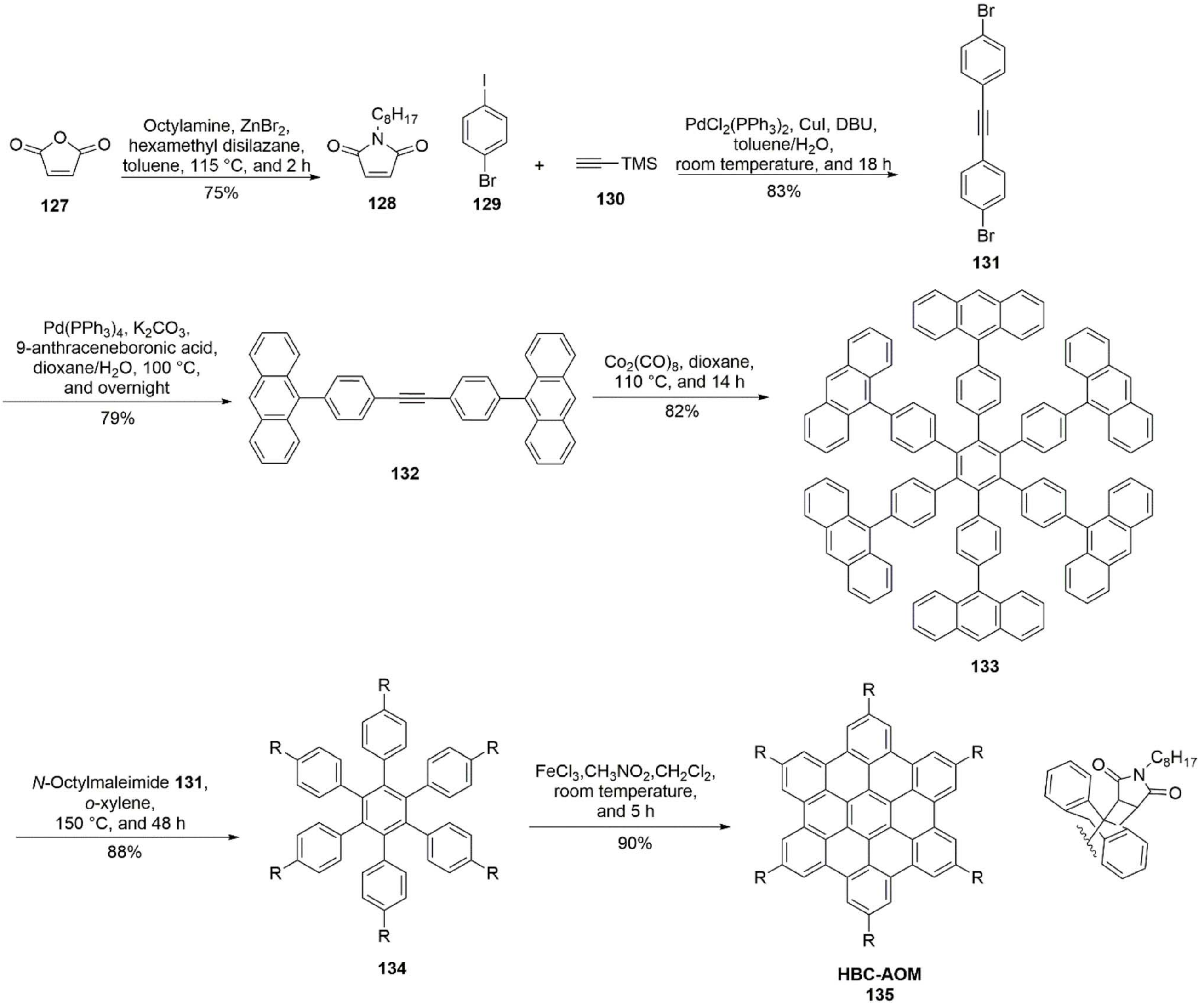

Scheme 13 Synthetic route towards HBC–AOM **135**.[169]

attached dppz unit. This electronic arrangement was supported by absorption spectra showing broadened bands with extended tails into the visible region, attributed to decreased molecular symmetry compared to the parent HBC. Photoluminescence studies revealed that both the free ligand and the rhenium complex emitted from the delocalized excited state, while the Re-dppz-HBC complex additionally exhibited a short-lived emission originating from a low-energy triplet state. Time-resolved transient absorption spectroscopy identified long-lived excited states: a delocalized HBC-centered state in the metal complexes and a non-emissive, dppz-localized excited state in the free ligand. Aggregation behavior remained largely unaffected by the dppz substitution. Emission analyses dependent on excitation wavelength and concentration demonstrated the formation of a lower-energy emissive state upon aggregation relative to unsubstituted HBC, with the dppz unit not significantly hindering supramolecular organization. This work presents an effective approach to tailor and enhance the photophysical properties of HBC systems through targeted functionalization and metal coordination, advancing their potential applications in optoelectronics and supramolecular chemistry.[171]

An *et al.* (2023) investigated novel class of chalcogen-doped nanographenes (NGs) by strategically incorporating chalcogen atoms (O, S, Se) into the core of HBC **159** or seco-HBC **165** frameworks, specifically targeting the fjord regions (Scheme 16). Due to the differing atomic sizes of the chalcogens, two distinct molecular topologies were formed during the final oxidative ring-closure step: oxygen doping yielded saddle-shaped structures, while sulfur and selenium doping produced helically twisted configurations (**155–165**). Furthermore, the highly distorted helical selenium oxide NGs could be reversibly converted into planar HBC structures in acidic environments. Given that planar HBC typically suffers from low solubility and strong aggregation tendencies, the use of helical selenium oxide NGs as soluble, processable precursors presents a practical

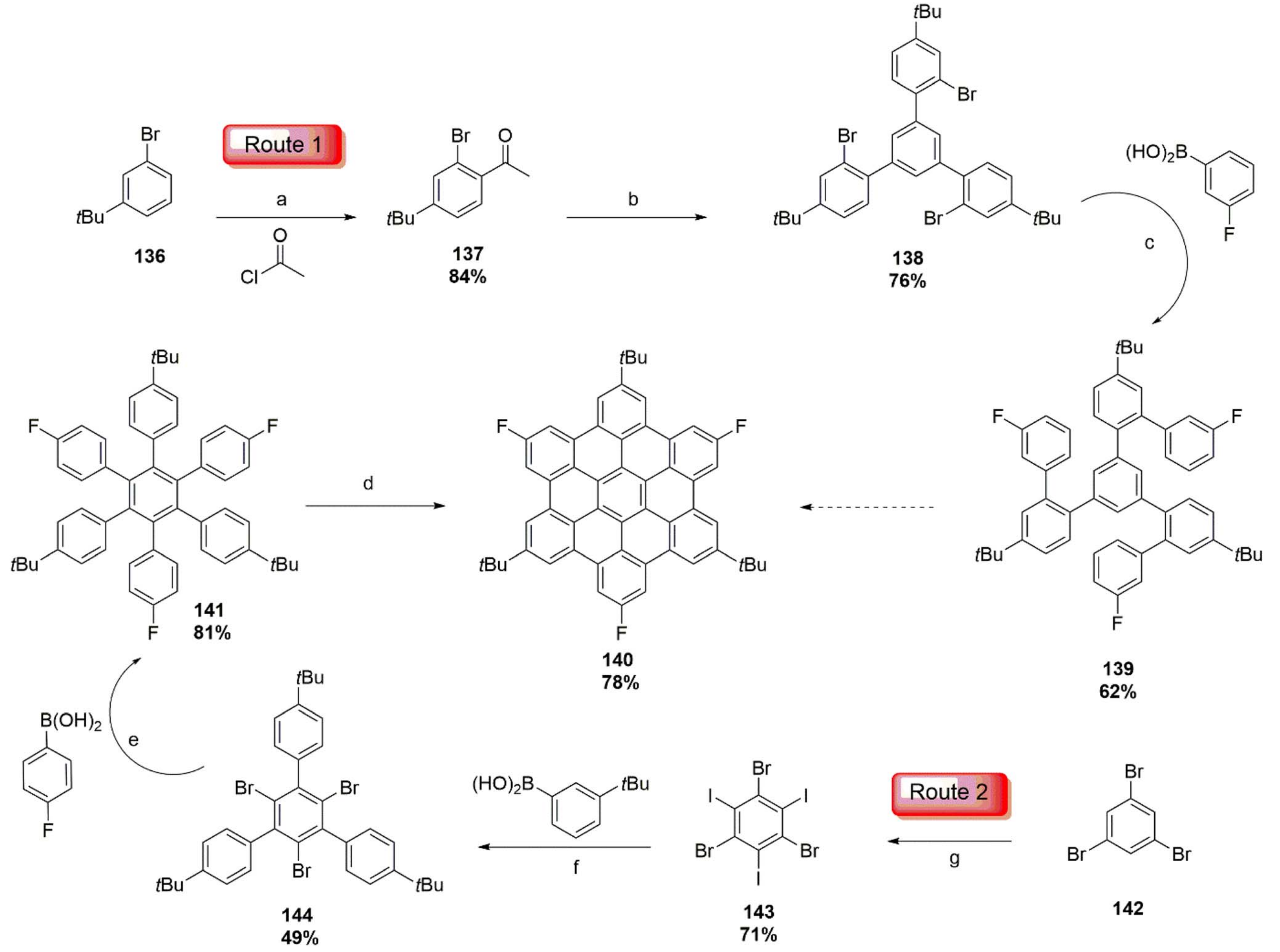

Scheme 14 Synthesis of F_3-HBC. (a) N_2, $AlCl_3$, CH_2Cl_2, 0 °C, r. t., 1 h; (b) N_2, $SiCl_4$, EtOH, 0 °C, r. t., 22 h; (c) Ar, $Pd(PPh_3)_4$, K_2CO_3, toluene, EtOH, H_2O, 110 °C, 19 h; (d) N_2, DDQ, TfOH, CH_2Cl_2, 0 °C, r. t., 2 h; (e) N_2, $Pd(dppf)Cl_2$, K_3PO_4, toluene, H_2O, 100 °C, 23 h; (f) N_2, $Pd(dppf)Cl_2$, K_3PO_4, toluene, H_2O, 100 °C, 17 h; (g) H_5IO_6, KI, H_2SO4, 0 °C, r. t., 4 d.[170]

route toward scalable fabrication of HBC-based materials. This strategy paves the way for advanced applications of HBC derivatives in electronic and optoelectronic devices, offering post-synthetic tunability and enhanced processability through smart molecular design.[172]

Jux *et al.* (2024) reported the synthesis of three porphyrin-HBC conjugates wherein one or two *meso*-linked HBC units are covalently attached to the β-positions of porphyrins through additional carbon–carbon bonds, as depicted in Scheme 17 (**166–171**). This streamlined synthetic approach allows for the preparation of these conjugates in a few steps without necessitating elaborate precursor designs. The critical oxidative cyclodehydrogenation step proceeds with high efficiency and minimal formation of side products. The antiaromatic character of the intervening pentalene unit significantly influences the photophysical properties, causing redshifts and broadening of absorption bands. Despite these structural modifications, the conjugates maintain good solubility and processability in common organic solvents, overcoming limitations previously observed in fused porphyrin systems. Demetalation of the conjugates enabled detailed optoelectronic studies, revealing that an increased biradicaloid character accelerates the decay of excited states by up to six orders of magnitude, with excited-state lifetimes decreasing from microseconds to the picosecond timescale. Especially, the excited-state deactivation bypasses the triplet state (T_1), occurring solely *via* the singlet excited state (S_1). These findings offer valuable insights for the rational design of molecular materials that demand precise control over both the dynamics and nature of excited states. Current synthetic efforts are directed towards the development of new conjugates featuring similar fusion motifs.[173]

Hirsch *et al.* (2025) reported the first synthesis of a new class of triskelion-shaped HBC derivatives functionalized with ethynyl groups, as illustrated in Fig. 20 (**172** and **173**). This methodology utilizes tris-iodinated HBC intermediates, enabling the selective introduction of various substituents *via* a key Suzuki coupling step that ensures C_3-symmetric prefunctionalization. The substitution of *tert*-butyl groups with mesityl moieties markedly enhanced the solubility of the compounds, thereby simplifying their purification. Through

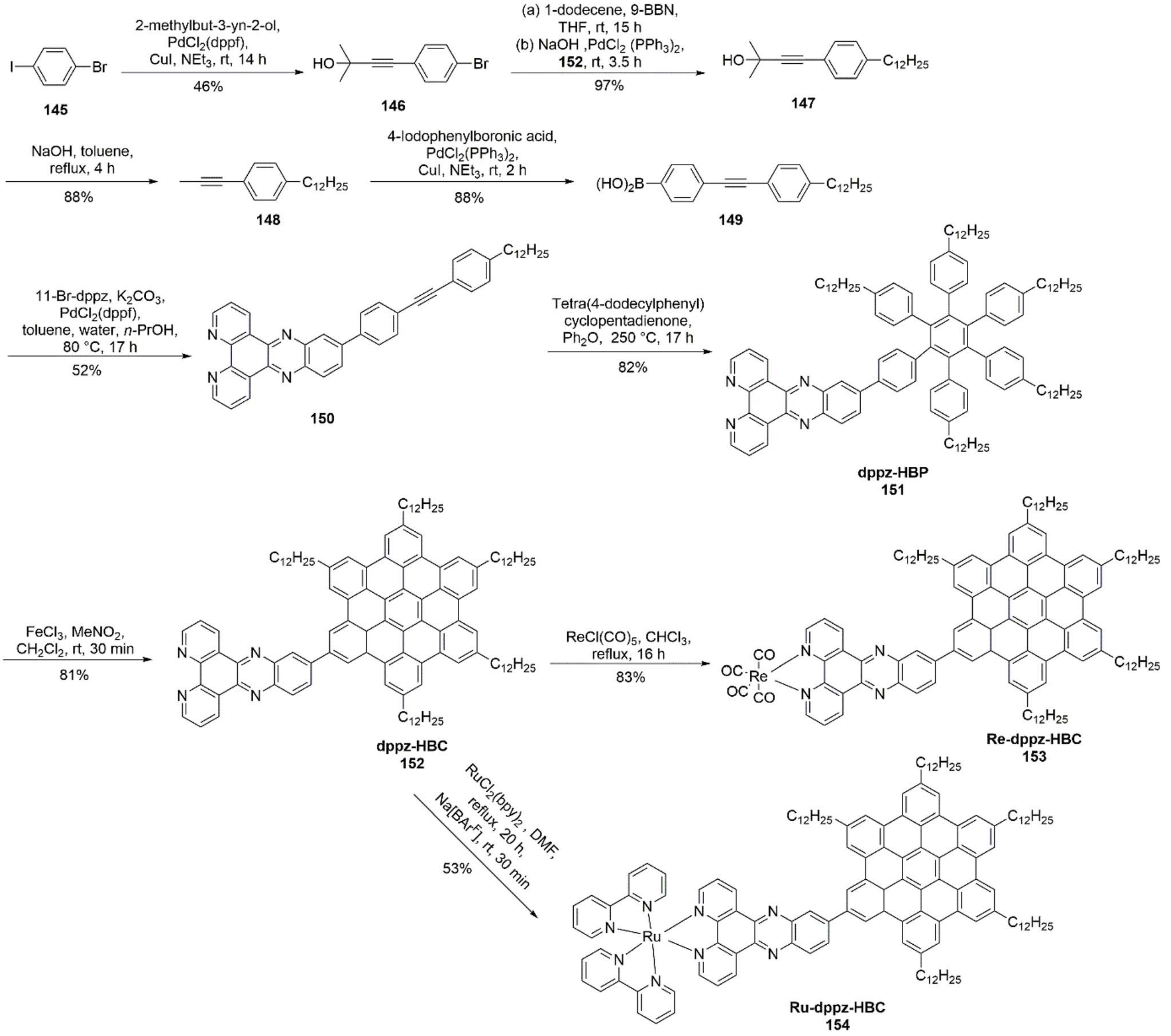

Scheme 15 Synthesis of the target ligand and complexes of HBC.[171]

this strategy, seven unique triskelion-shaped HBC derivatives were obtained. Spectroscopic analysis revealed that, relative to the iodinated precursors **172** and **173** ($\lambda_{max} = 365$ nm), the tris-substituted HBCs displayed a bathochromic shift of up to 23 nm in their absorption maxima, underscoring the significant influence of substitution on their electronic absorption characteristics.[174]

3. Molecular structure and physical properties of HBCs

The properties of PAHs are influenced by the size, shape, and molecular architecture of their aromatic cores. PAHs exhibit a wide variety of sizes and structural arrangements depending on how their rings are fused, either angularly or linearly, such as *peri-* or *cata-*fusion. This fusion pattern significantly affects their chemical and physical behavior. For example, linearly fused PAHs tend to be less stable than angularly fused isomers and are more susceptible to degradation processes like dimerization or endoperoxide formation.[61,62] The benzenoid character rule states that a molecule's aromatic stabilization increases with the number of distinct aromatic sextets it contains. This principle aids in explaining differences in chemical stability and reactivity among structurally related compounds.[175] The crystal packing arrangements of PAHs are significantly influenced by ring fusion. The relative orientation of molecular planes within the crystal lattice defines the four common packing motifs observed in PAH crystals.[176,177] PAH crystal packing can be categorized into four main types: (a) sandwich herringbone arrangement, where pairs of π-stacked molecules align in a herringbone-like fashion, as observed in pyrene; (b) traditional herringbone pattern, dominated by edge-to-face

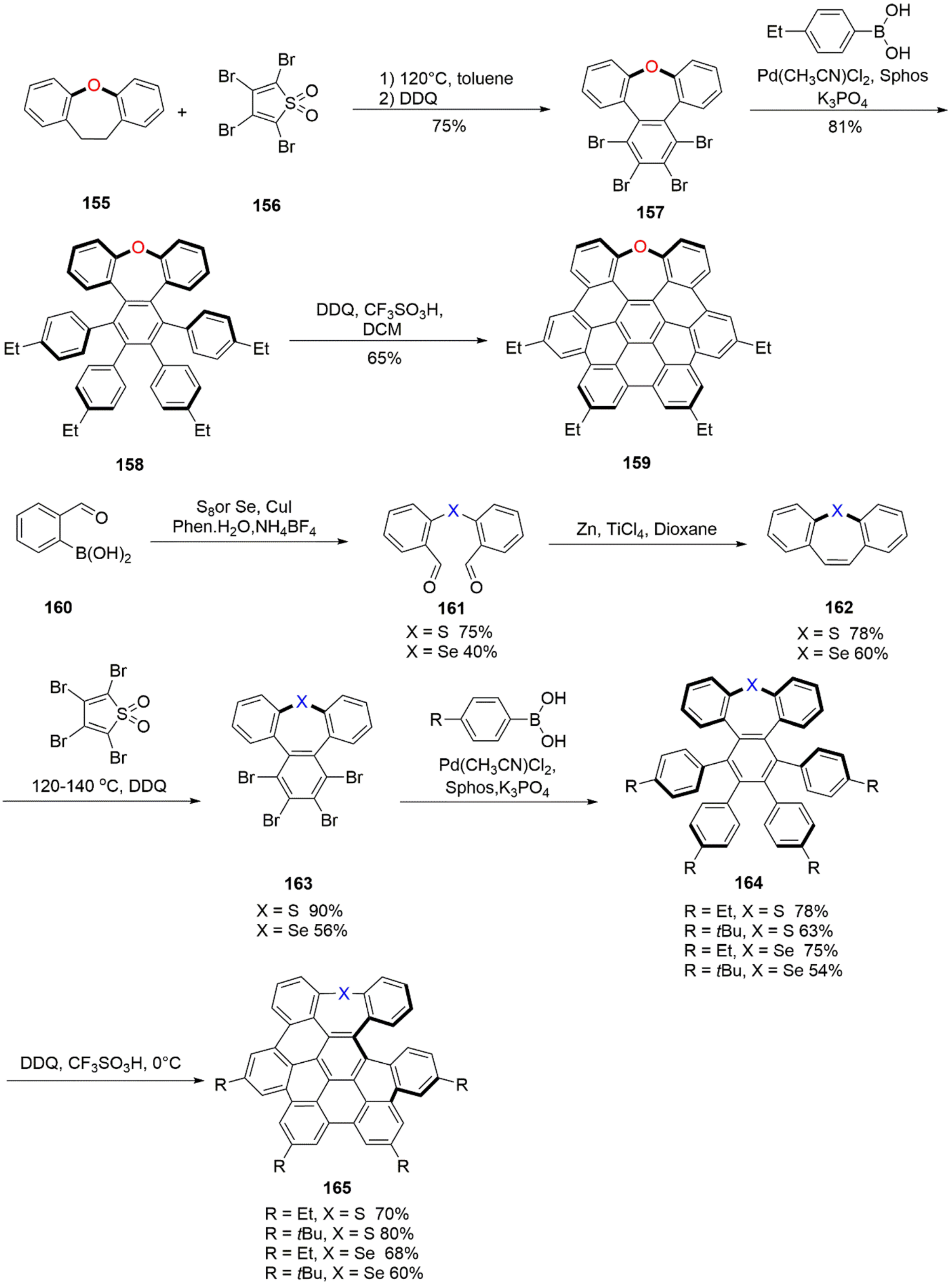

Scheme 16 Synthesis of oxygen-doped NG, sulfur-doped NGs, and selenium-doped NGs.[172]

interactions, typical of coronene; (c) γ configuration, a more planar variant of coronene's herringbone structure; and (d) β motif, consisting of stacked layers resembling graphitic sheets, exemplified by tribenzopyrene. Variations in the carbon-to-hydrogen ratio among PAHs influence these packing motifs, determining the predominance of either π–π stacking or C–H⋯π interactions in the solid state. PAHs with lower C–H ratios generally favor edge-to-face C–H⋯π interactions, whereas those with higher C–H ratios, such as disc-shaped molecules like coronene, predominantly exhibit strong π–π stacking. These

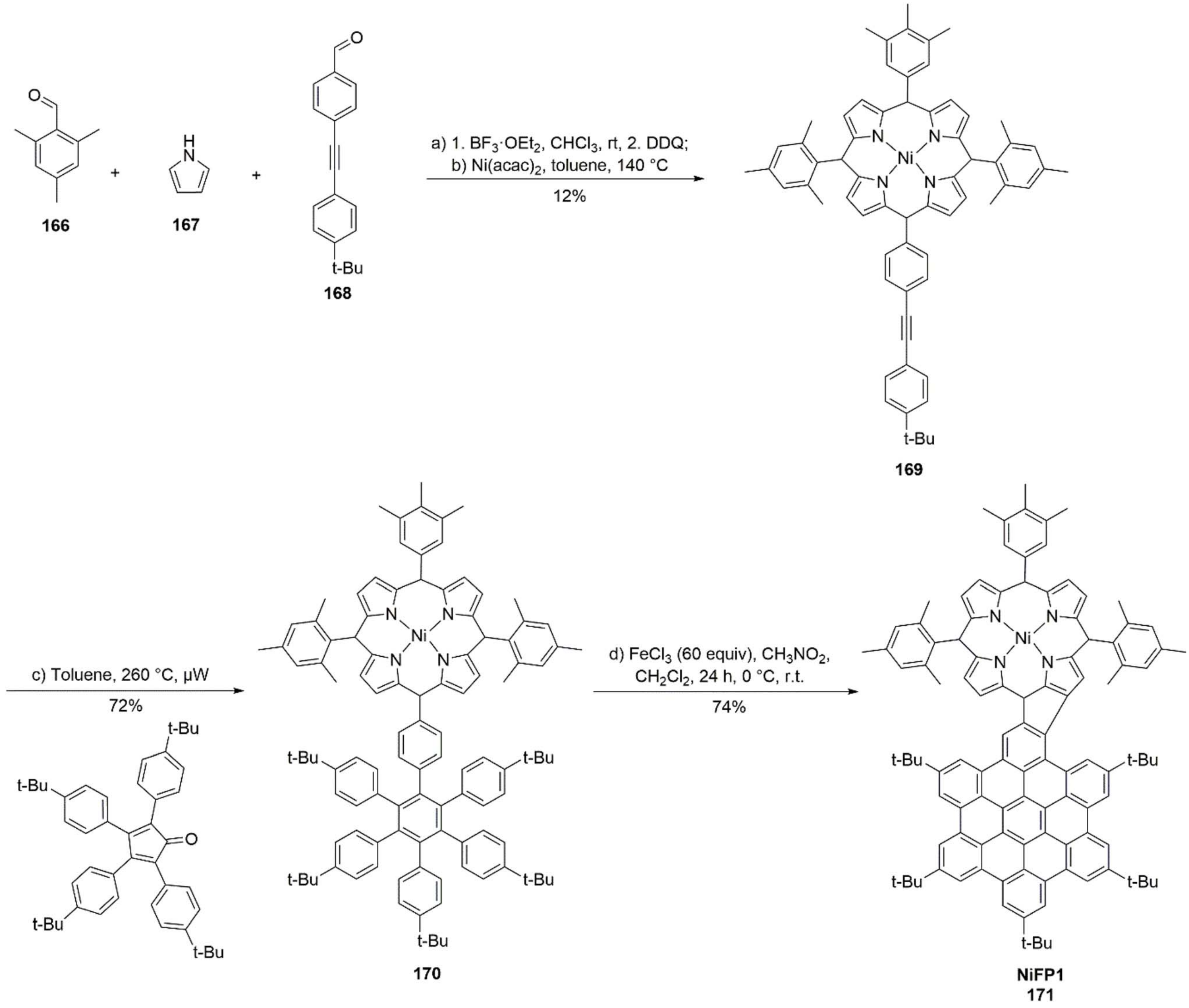

Scheme 17 Synthesis of fused porphyrin NiFP1.[173]

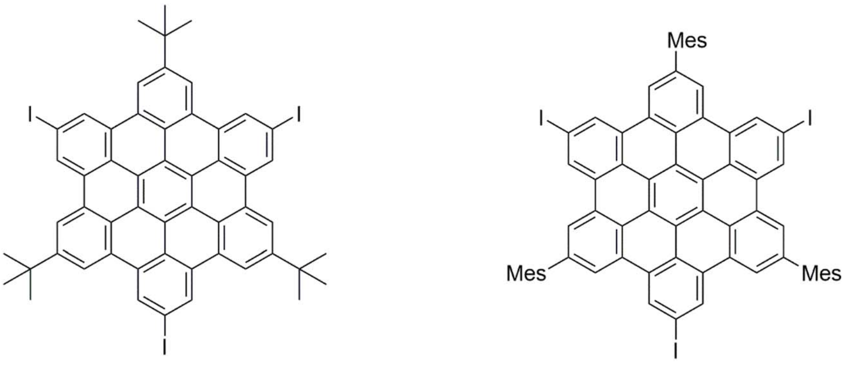

172 **173**

Fig. 20 Chemical representation of tris-iodinated HBC derivatives synthesized using Suzuki coupling reaction.[174]

distinct packing arrangements are of significant importance in organic electronics, where π–π stacked and herringbone structures are extensively investigated for their role in enhancing charge carrier mobility.[178] Clar reported the UV-Vis absorption spectrum of unsubstituted HBC dissolved in trichlorobenzene.[179]

In Clar's classification, HBC displays three distinctive electronic absorption bands—α, p, and β—similar to those found in other PAHs.[180] The α-band, observed at the longest wavelength near 440 nm with low intensity, corresponds to the electronic transition from the second-highest occupied molecular orbital (HOMO$-$1) to the lowest unoccupied molecular orbital (LUMO), commonly identified as the 0–0 transition.[181] Substitution of the HBC core with either electron-donating or electron-withdrawing groups caused negligible changes in its absorption profile. However, conjugation with thiophene dendrimers through fluorene linkers induced a slight redshift and broadened the absorption spectrum.[113] The symmetry of substituents on the HBC core had little effect on absorption characteristics, whereas photoluminescence studies showed that lower-symmetry derivatives exhibited a stronger 0–0 emission band compared to higher-symmetry analogs, which displayed reduced intensity in this transition.[182] The high carbon-to-hydrogen ratio in unsubstituted HBC leads to pronounced π–π stacking interactions in its single-crystal X-ray structure, where molecules adopt a γ-type packing arrangement (Fig. 21).[182,183] The interplanar spacing between aromatic cores is 3.42 Å, slightly larger than that of graphite (3.35 Å). Due to dense molecular packing, the HBC molecules tilt approximately 48° relative to the basal (010) plane, resulting in an offset of 3.8 Å between adjacent molecular centers within the π-stack. A characteristic feature of HBC is its nearly planar geometry, supported by minimal distortion in the bay regions and uniform C–C bond lengths in the central benzene ring.

HBC inherently suffers from poor solubility, which limits its application in cost-effective solution-processing techniques despite its strong π-stacking interactions in the solid state. Advances in synthetic methodologies have enabled the functionalization of HBC with solubilizing groups, whose nature and position critically influence molecular properties. For example, single-crystal X-ray diffraction analysis of permethoxylated HBC revealed that steric repulsion among methoxy substituents in the bay regions induces a nonplanar, double-concave molecular conformation.[183] Conversely, the introduction of extended solubilizing chains at the *peri* positions of the peripheral phenyl rings preserved the planar geometry of the HBC core.[184,185] The presence of flexible side chains separating the rigid aromatic core promotes an isolated columnar packing motif; however, structural defects within these columns can significantly impair charge carrier mobility along the π-stacking axis.

The thermotropic phase behavior of substituted HBC derivatives has been extensively characterized using various analytical techniques, including polarized optical microscopy POM (polarized optical microscopy),[186,187] solid-state NMR spectroscopy,[188,189] differential scanning calorimetry (DSC),[186,187] and 2D wide-angle X-ray scattering (2D WAXS).[125] While DSC is effective in detecting phase transitions, 2D WAXS provides detailed insight into molecular packing within each phase. These studies indicate that substituted HBC undergoes a pronounced phase transition from a tilted columnar crystalline arrangement to a more ordered liquid-crystalline phase, in which molecules stack perpendicularly to the columnar axis.[190,191] This transition enables molecular self-healing and facilitates reorganization into highly ordered structures upon annealing near the phase transition temperature. The melting and isotropization temperatures are strongly influenced by the length and branching of the alkyl substituents. For instance, an HBC derivative bearing dodecyl chains exhibits a slightly lower isotropization temperature (417 °C) compared to its octyl-substituted analog (430 °C).[186] Incorporation of branched alkyl chains further reduces the melting point,[116,184,186] likely due to altered π–π interactions between aromatic cores mediated by the substituents.

Beyond solubility and thermal properties, substituents on the HBC core significantly affect aggregation behavior in solution, which in turn governs self-assembly processes and film morphology. Techniques such as photoluminescence spectroscopy, UV-Vis absorption, and ^{1}H-NMR spectroscopy have been employed to probe aggregation phenomena. For example, bulky *t*-butyl substituents effectively inhibit aggregation due to steric hindrance. ^{1}H-NMR studies demonstrated that HBC derivatives with long, linear dodecyl chains remain predominantly monomeric in 1,1,2,2-tetrachloroethane-d$_2$ at concentrations below 10^{-6} M, while higher concentrations induce self-aggregation. Derivatives with longer branched chains exhibit reduced aggregation compared to shorter-branched analogs, underscoring the critical role of alkyl chain branching on solution-phase aggregation.[187]

Fluorene-substituted HBC (FHBC) derivatives tend to aggregate in solution, with concentration-dependent ^{1}H-NMR experiments confirming pronounced π–π stacking

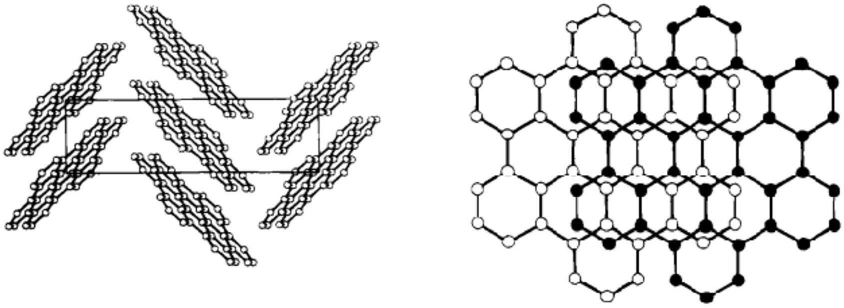

Fig. 21 Crystal structure and packing of HBC **1**.[183]

interactions centered on the HBC core.[141–144] Steric effects from fluorene groups induce a staggered arrangement of HBC discs within columnar stacks. Introduction of various substituents into FHBC molecules has been shown to promote helical packing motifs and drive a transition from columnar to lamellar structures in the solid state.[142,143]

Asymmetrically substituted HBC molecules featuring carboxylic acid termini on their alkyl chains have been designed to exploit hydrogen bonding for stabilizing columnar phases in the solid state.[187] Monocarboxylic acid-functionalized HBCs assemble into dimers *via* hydrogen bonding between carboxyl groups, resulting in a compact hexagonal lattice with vertically aligned columns. Extending the alkyl spacer linking the carboxylic acid to the HBC core weakens these interactions and induces a tilted columnar packing due to steric effects from the longer linker. The addition of a second para-substituted carboxylic acid group substantially enhances supramolecular stability by forming hydrogen-bonded polymers, producing non-tilted, highly ordered columnar arrangements.

Fig. 22 illustrates a series of Gemini-shaped amphiphilic HBC derivatives exhibiting unique self-assembly behavior compared to other HBC systems.[75,77,109,122,134–140,192–196] These molecules form bilayer assemblies in solution, with hydrophilic segments exposed to the solvent and interdigitated alkyl chains from adjacent HBC layers generating densely packed structures. This two-dimensional pseudo-graphitic arrangement further organizes into nanotubular architectures observed by scanning electron microscopy (SEM). Along the nanotube axis, HBC cores stack *via* π–π interactions with an interplanar spacing of approximately 3.6 Å. Although these nanotubes exhibit significant thermal stability, elevated temperatures eventually disrupt their structure. Detailed analyses indicate that the presence of lipophilic side chains and phenyl substituents is critical for successful nanotube formation.[75]

Symmetric, disc-shaped HBC derivatives typically self-assemble into columnar structures that align preferentially along the extrusion axis (Fig. 23). Solid-state samples produced by extruding the pure compounds demonstrate significant macroscopic alignment of these HBC derivatives.[184]

A recent study demonstrated the use of anodized aluminum oxide templates in an imprinting method to fabricate nanostructured patterns on HBC sheets.[197] Precise replication of nanoscale columnar architectures was achieved utilizing an HBC derivative functionalized with cross-linkable acrylate groups. Additionally, methods such as zone casting, magnetic field-assisted alignment, and deposition onto pre-patterned substrates have been employed to regulate the orientation of HBC-based materials across different surfaces.

The molecular structure of HBC-based triptycene **36a** was elucidated through single-crystal X-ray diffraction analysis. Single crystals suitable for crystallographic examination were obtained by the slow diffusion of diethyl ether into a dichloromethane solution of **36a**. As illustrated in Fig. 24a, the HBC moiety exhibits a twisted planar conformation with an approximate diameter of 11 Å. One-dimensional chain structures are established *via* C–H⋯π interactions, with contact distances of 2.803 and 2.855 Å, occurring between the hydrogen atoms of the triptycene framework and the π-electron system of the HBC core. Furthermore, adjacent chains are linked into layered assemblies through additional C–H⋯π interactions involving hydrogens from the *tert*-butyl groups and the benzene rings of the triptycene unit, with an interaction distance of 2.880 Å. These layers subsequently stack to form a porous three-dimensional network, as depicted in Fig. 24c.[146]

To elucidate the crystallization behavior of FHBC materials in thin films, single crystals were grown by the slow evaporation of isopropanol into a dichloromethane solution of FHBC. The asymmetric unit comprises a central π-stacked FHBC molecule flanked above and below by two half-molecules located on crystallographic inversion centers, with all three π-systems nearly parallel in orientation. The interplanar spacings of approximately 3.42 Å and 3.04 Å, together with centroid-to-centroid distances of 4.141 Å and 4.498 Å between the central hexabenzocoronene core and the adjacent molecules, reveal significant slippage within the π-stacking arrangement. Additionally, the structure contains three disordered dichloromethane solvent molecules. Remarkably, except for the π–π stacking parameters, the dimensional data derived from

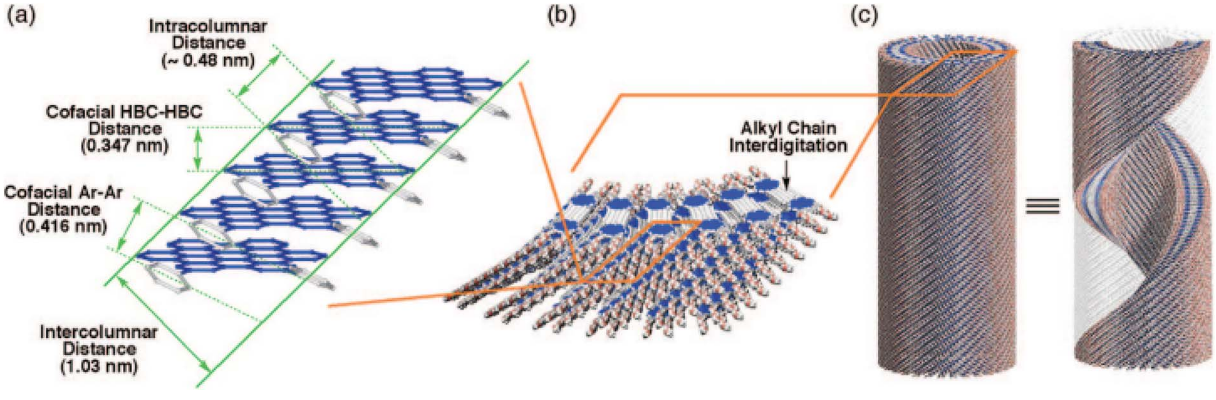

Fig. 22 Diagram representing the packing arrangements in nanotubes ((a)–(c)). Reproduced from ref. 75 with permission from American Chemical Society, Copyright © 2008.

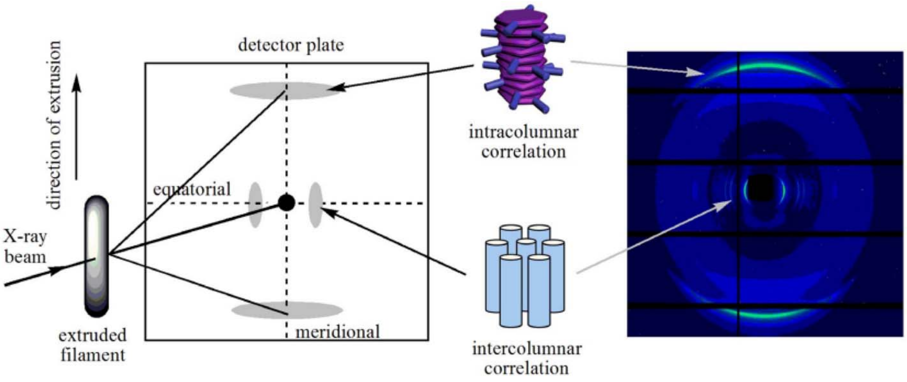

Fig. 23 Diagrammatic illustration of the experimental assembly (left) and 2D WAXS pattern of HBC scaffold **28** represent intra- and inter-columnar organization (right). Reproduced from ref. 184 with permission from American Chemical Society, Copyright © 2005.

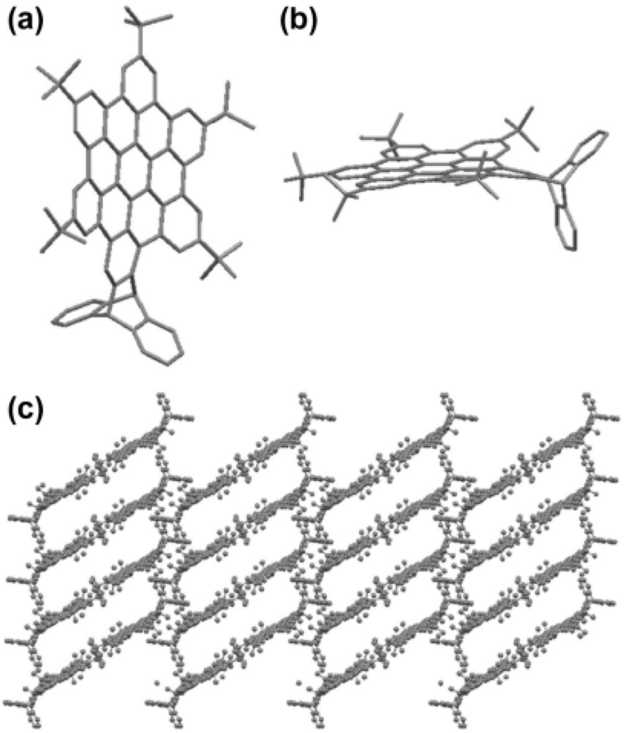

Fig. 24 Schematic representation of top (a), side view (b) and crystal packing of HBC-based triptycenes (c). Reproduced from ref. 146 with permission from Elsevier, Copyright © 2014.

grazing-incidence wide-angle X-ray scattering (GIWAXS) of thin films diverge from those obtained *via* single-crystal analysis. As illustrated in Fig. 25, these discrepancies indicate that the crystallization pathways of FHBC in thin films differ markedly from those in solution, leading to distinct crystalline polymorphs.[198]

The physical properties of unsymmetrically substituted HBC derivatives were investigated using differential scanning calorimetry (DSC), polarized optical microscopy (POM), and small- and wide-angle X-ray scattering (SAXS/WAXS) to characterize their thermotropic liquid crystalline behavior of compounds **48** and **49.** Despite the nonplanar configuration of their aromatic cores, the molecules exhibited dense packing within the mesophase, resulting in the formation of highly ordered structures. Especially, the tri-alkoxy-substituted derivative organized into a well-defined columnar rectangular mesophase, whereas the di-substituted analogue formed a columnar hexagonal mesophase, as depicted in Fig. 26.[150]

The molecular structures of compounds **60a** and **60b** were definitively characterized by X-ray diffraction analysis. In **60a,**

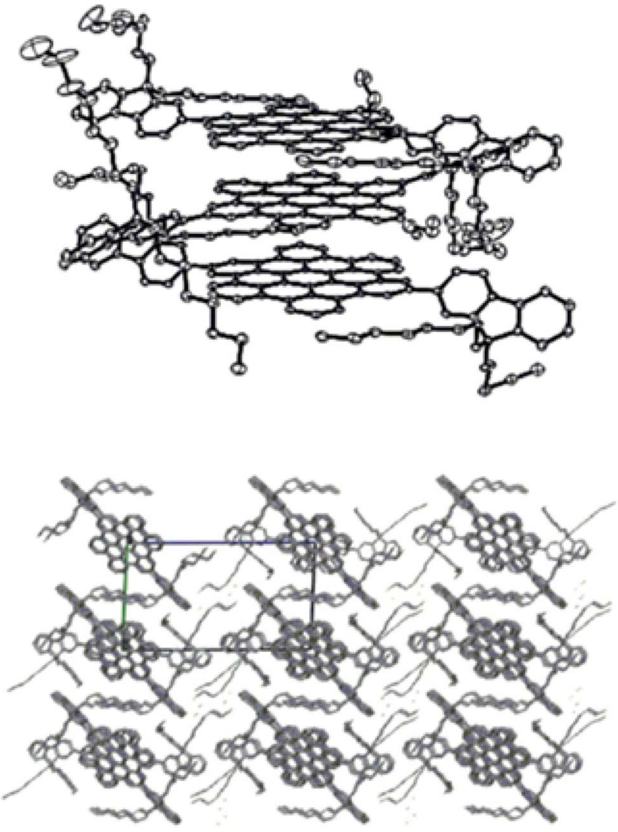

Fig. 25 The thermal ellipsoid representation of the FHBC structure (top) and the crystal packing arrangement (bottom) along the *a*-axis are depicted. Reproduced from ref. 198 with permission from American Chemical Society, Copyright © 2014.

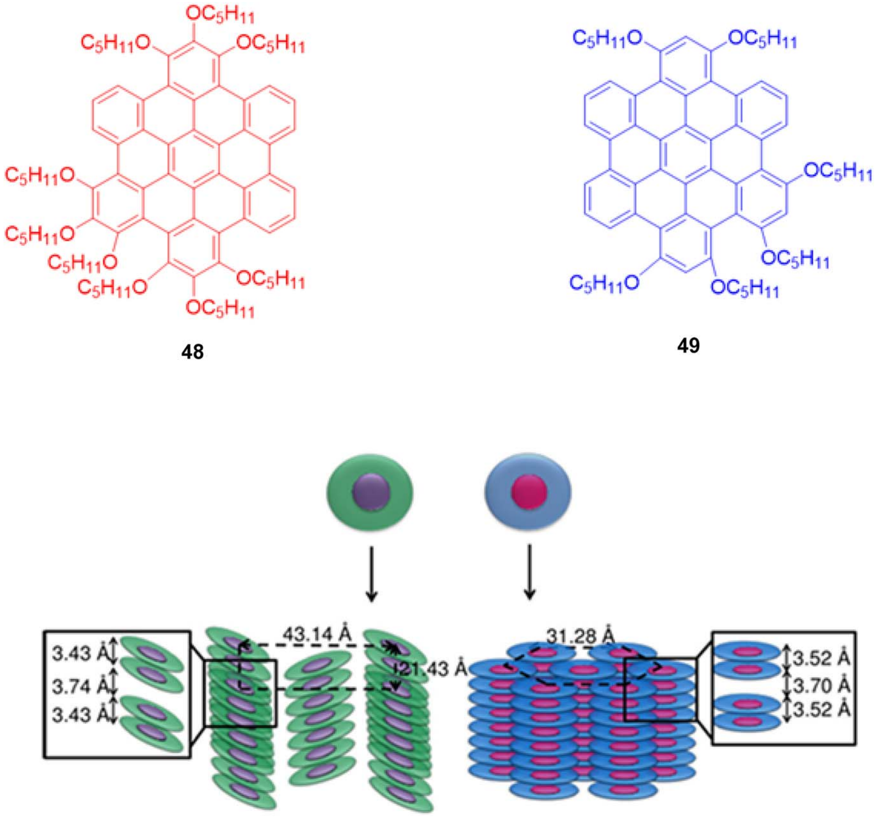

Fig. 26 Supramolecular arrangements of mesogens in mesosphere. Reproduced from ref. 150 with permission from John Wiley & Sons, Copyright © 2016, Wiley-VCH Verlag GmbH & Co. KGaA, Weinheim.

the ethene linker adopts a cis configuration, resulting in a partial overlap between the two HBC cores. This arrangement corresponds to the two significantly upfield-shifted signals observed in the ^{1}H-NMR spectrum of **60a**. The dihedral angle between the HBC planes in **60a** was measured at 38.44°, while the average torsion angle between the central dicyanoethene moiety and the HBC core was 36.95°. The central C═C bond length in **61a** was determined to be 1.342 Å, slightly longer than typical sp^2–sp^2 carbon–carbon bonds (∼1.34 Å) and within the range reported for fumaronitrile derivatives (1.34–1.36 Å). Additionally, a consistent CH–π interaction was inferred from the 3.345 Å distance observed between the *para*-methyl carbons of the mesityl groups and the HBC surfaces. In contrast, compound **60b** features a *trans* configuration of the HBC units, with the ethene linker oriented in opposite directions. The two HBC planes in **60b** are perfectly parallel, exhibiting a dihedral angle of 0.0°. However, the average tilt angle between the HBC cores and the central dicyanoethene unit increased to 46.79°, attributed to steric repulsions between the cyano substituents and the HBC framework, which cause the dicyanoethene segment to tilt relative to the HBC planes. The central C═C bond length in **60b** was recorded as 1.343 Å, comparable to that of **60a**, as illustrated in Fig. 27.[153]

Du *et al.* (2017) employed the DMol^3 software to perform DFT calculations aimed at investigating the structural and electronic properties of the nanoring [4]CHBC **61**. To simplify the initial geometry optimization, all peripheral methyl groups were replaced by hydrogen atoms, as these substituents exert minimal influence on the conjugated framework (Fig. 28a and b). The entire molecular structure was fully relaxed without any constraints, maintaining D_2 symmetry. Each HBC monomer is linked to its adjacent units *via* a C–C single bond approximately 1.485 Å in length, exhibiting a torsion angle near 35.988°. Analysis of the frontier molecular orbitals revealed that both the HOMO−1 and LUMO+1 correspond to tap-type antibonding orbitals localized on opposite sides of the macrocycle, rather than around the equatorial region. The calculated HOMO–LUMO energy gap of 1.81 eV suggests that the nanoring structure possesses considerable stability.[154]

X-ray diffraction analysis demonstrated that the π-system of SB-HBC (**62**) is arranged in an orthogonal manner, with adjacent molecules stacking *via* a characteristic one-dimensional π–π overlap. Single crystals of SB-HBC were obtained by the gradual diffusion of pentane vapor into a tetrahydrofuran solution. As illustrated in Fig. 29, the SB-HBC molecule exhibits a nearly orthogonal spiro configuration, characterized by a dihedral angle of 87.01° between the two fused five-membered rings. This angle closely corresponds to the previously reported torsion angle of approximately 89.01° for SBF and is consistent with the 88.71° value predicted by gas-phase DFT calculations at the B3LYP/6-31G(d,p) level. The HBC units within SB-HBC display a slight twist, with a maximum deviation of 0.48 Å between the central

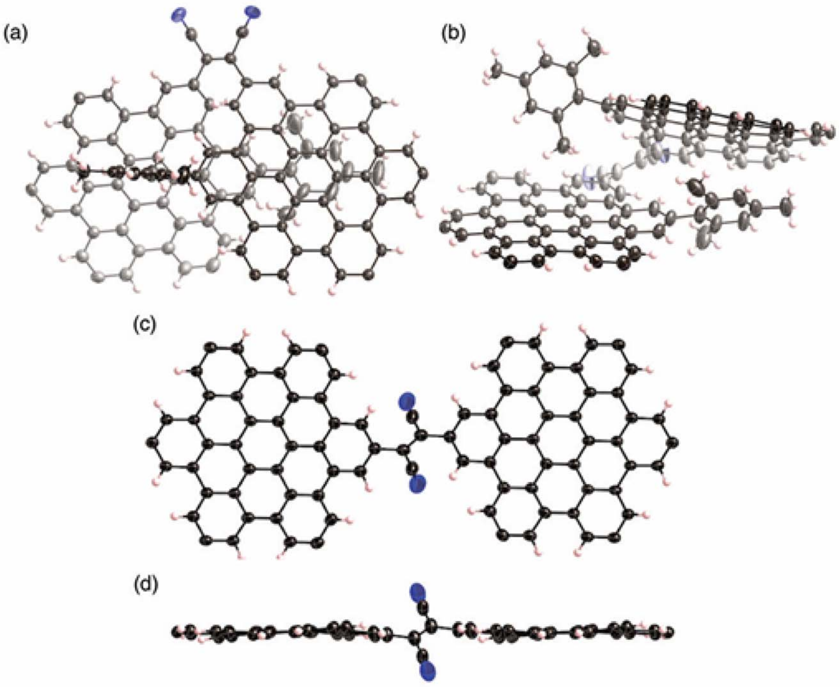

Fig. 27 X-ray crystal representation of (a) **60a** and (b) **60b** along with top and side view of (c) **60a** and (d) **60b**. Reproduced from ref. 153 with permission from the Royal Society of Chemistry.

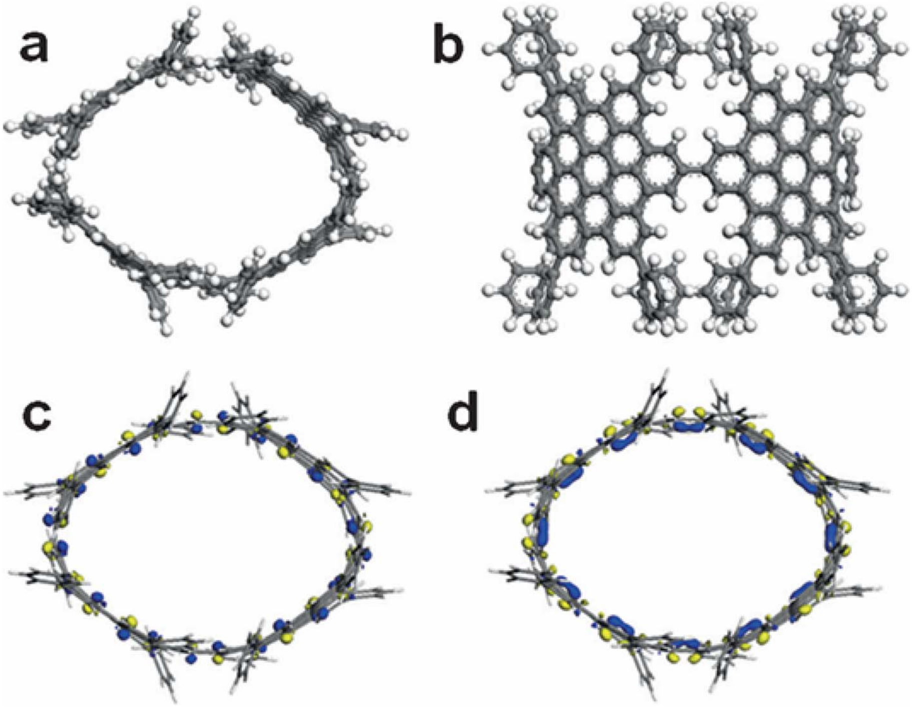

Fig. 28 Frontier MOs and optimized geometry of [4]CHBC: (a) molecular structure top view; (b) molecular structure side view; (c) [4]CHBC HOMO; (d) [4]CHBC LUMO. Reproduced from ref. 154 with permission from John Wiley & Sons, Copyright © 2017, Wiley-VCH Verlag GmbH & Co. KGaA, Weinheim.

benzene plane and the peripheral carbon atoms, attributed to steric strain induced by the *tert*-butyl substituents on the five-membered rings. Importantly, neighboring SB-HBC molecules assemble into one-dimensional chains through π–π interactions between their HBC cores along the *c*-axis, as depicted in Fig. 29c, with π–π stacking distances ranging from 3.42 to 3.63 Å. This

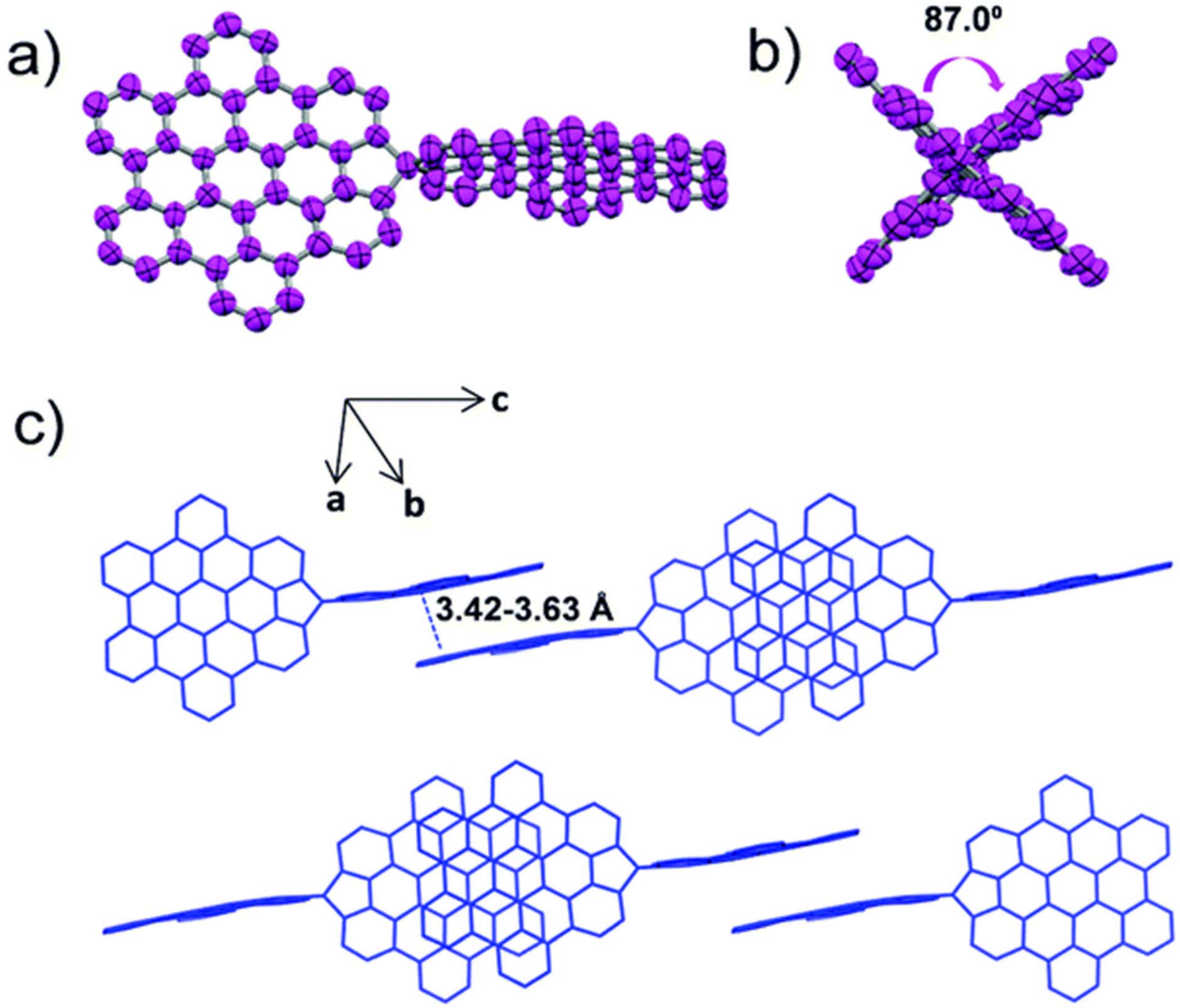

Fig. 29 Crystal structure analysis of SB-HBC: (a) top-down perspective, (b) lateral perspective, and (c) molecular arrangement of SB-HBC within a single unit cell. Reproduced from ref. 155, https://doi.org/10.1039/C8CC07405D, under the terms of the CC BY-NC 3.0 license, https://creativecommons.org/licenses/by-nc/3.0/.

stacking arrangement is analogous to the extended one-dimensional charge transport pathways previously reported for spirobiphenalenyl neutral radicals.[155]

Fan *et al.* (2018) developed and synthesized a group of disc-cube triads called HBC-2POSS, featuring a single HBC unit linked to two polyhedral oligomeric silsesquioxane (POSS) groups, as illustrated in Fig. 30. With a short spacer, **63-A** exhibits weak hydrogen bonding at room temperature. As a result, the self-assembled structures of **63-A** and **63-E** are similar. In both cases, the presence of POSS crystals within the nanophase-separated LamCol$_{ob}$ structures leads to the formation of hierarchical architectures. When the spacer length in **64-A** is increased compared to **63-A**, the hydrogen bonding becomes stronger. As a result, the self-assembly behavior of **64-A** differs from that of **64-E**. While **64-E** generates a K$_{POSS}$-in-LamCol$_r$ structure, **64-A** forms a three-dimensional ordered Col$_{ob}$ structure without the crystallization of POSS. It is believed that strong hydrogen bonding, enabled by the appropriately extended spacer, inhibits POSS crystallization. Additionally, hydrogen bonding promotes π–π stacking and drives the formation of highly ordered assemblies. This study offers an approach to balancing multiple interactions within hybrid

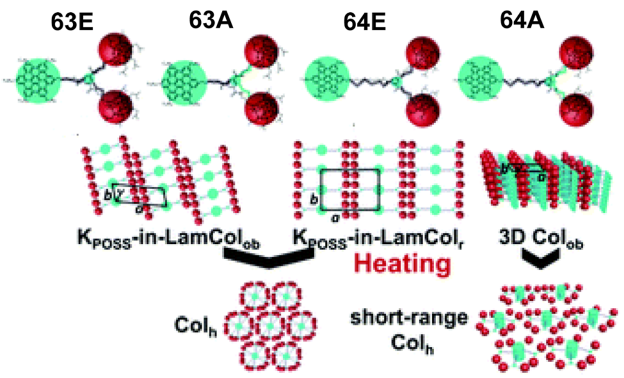

Fig. 30 WAXS profile of four triads HBC-2POSS. Reproduced from ref. 156 with permission from the Royal Society of Chemistry.

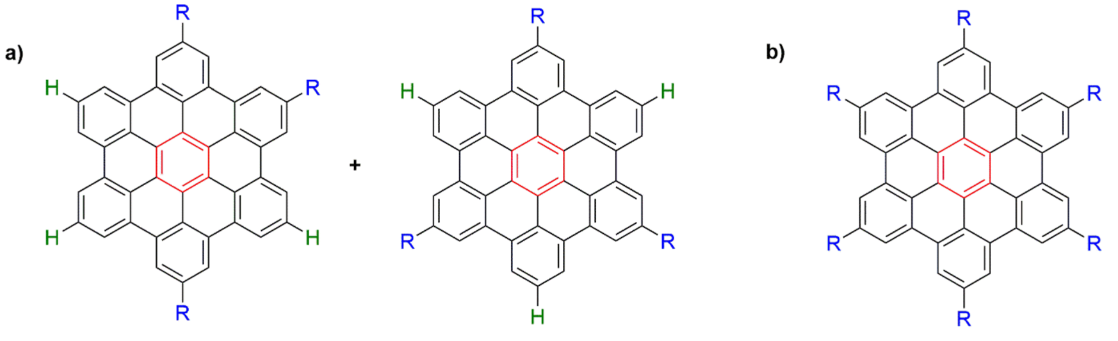

174 **175** **176**

$R = C_nH_{2n+1}$ n = 4, **174a + 175a**
n = 6, **174b + 175b**
n = 8, **174c + 175c**
n = 12, **174d + 176d**

Fig. 31 (a) HBC derivatives with C_1- and D_{3h}-symmetry (where n represents the alkyl chain length). (b) HBC-C12 with D_{6h}-symmetry.[199]

systems to achieve materials with high etching contrast and well-organized hierarchical structures.[156]

Unsymmetrical HBC derivatives generally display reduced melting points and narrower phase transition intervals, attributable to their lowered molecular symmetry, which results in less efficient molecular packing. In this case, Chen *et al.* (2019) demonstrated that blending low-symmetry HBC molecules (C_1 symmetry) with higher-symmetry counterparts (D_{3h} symmetry) resulted in a uniform phase transition and a significant reduction in isotropic transition temperatures compared to the D_{6h}-symmetric analogs. Among the studied series, a 2 : 1 mixture of the long-chain-tethered compounds **174d** and **175d** yielded a shifted and more stabilized mesophase range along with the lowest melting point. This approach offers an effective strategy for addressing thermal decomposition issues in highly symmetric columnar liquid crystalline systems, as shown in Fig. 31 **174–176**.[199]

To determine the three-dimensional structure, single crystals of NG **84a** suitable for X-ray diffraction were obtained by growing them from a biphasic solution of DCM and *n*-hexane. As illustrated in Fig. 32a and b, X-ray analysis revealed that NG **84a** adopts a unique half-curved conformation. The MDBA unit and the fused naphthalene rings together form a concave surface measuring 14.0 Å across (between atoms C6 and C6′) and a depth of 4.0 Å, supported by hydrogen bonding interactions: C(H)⋯π contacts at 2.67 and 2.72 Å, and a C(H)⋯O interaction at 2.52 Å.[161]

The three-dimensional structure of the HBC compounds was ascertained by semi-empirical computations, suggesting that the compounds have a D_{3h}, C_{3h}, or C_3 symmetry based on the substitutions. The calculations for the mesityl-substituted molecule **177** also show a planar structure, with the exception that the mesityl substituent is angled roughly 45° out of the plane. This was anticipated since the mesityl groups improved

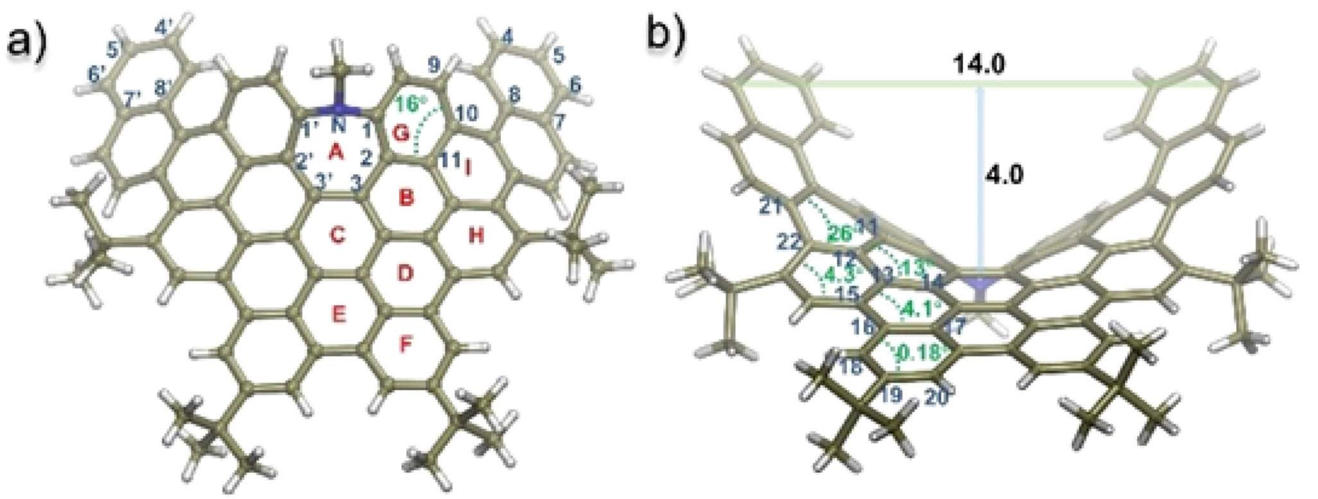

Fig. 32 Top (a) and side (b) views X-ray crystallographic structures of NG **84a** with 50% probability of thermal ellipsoids. Reproduced from ref. 161 with permission from John Wiley & Sons, Copyright © 2024, Wiley-VCH Verlag GmbH & Co. KGaA, Weinheim.

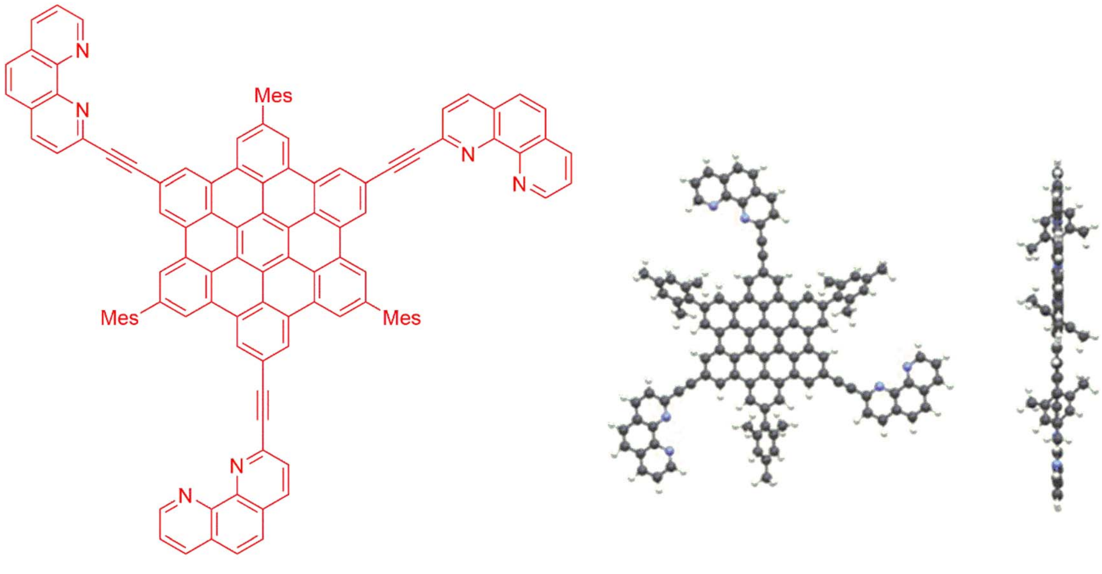

177

Fig. 33 Semi-empirical methods were used to calculate the top and side views of structure of **177** (for example C_3 symmetry) along with the chemical structure. Reproduced from ref. 174 with permission from John Wiley & Sons, Copyright © 2025, Wiley-VCH Verlag GmbH & Co. KGaA, Weinheim.

the compounds' solubility by preventing the π–π stacking of the HBCs. This resulted in the determination of no extra rotation axes or mirror planes, suggesting a C_3 symmetry for all mesityl substituted HBCs that were provided as indicated in Fig. 33.[174]

Two-dimensional wide-angle X-ray scattering (2D-WAXS) confirmed that the molecules spontaneously organized into liquid crystalline columns, maintaining high stability over a broad temperature range. Scanning tunneling microscopy (STM) revealed that the donor–acceptor (D–A) molecules could assemble into well-ordered bilayers featuring star-shaped patterns. Additionally, STM imaging of HBC-6BTZA at the solution–solid interface provided molecular-level insight into its self-assembly characteristics. The results indicated that HBC-6BTZA formed well-organized adlayers at the interface between highly oriented pyrolytic graphite (HOPG) and 1,2,4-trichlorobenzene (TCB). As shown in the large- and small-scale

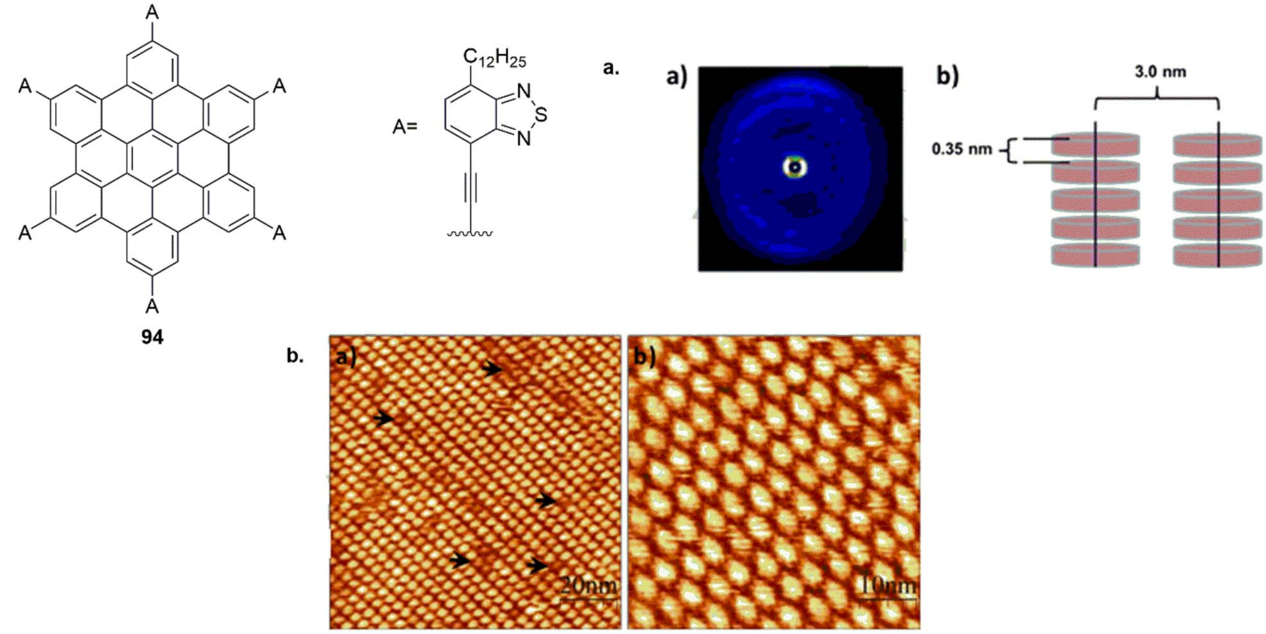

Fig. 34 (a) 2D-WAXS image of HBC-6BTZA (b) Schematic representation of the columnar organization and STM pictures of the HBC-6BTZA-formed bilayer at the TCB/HOPG interface. (b) (a) Large-scale STM image of the bilayer (b) Small-scale STM image. Reproduced from ref. 163 with permission from John Wiley & Sons, Copyright © 2025, Wiley-VCH Verlag GmbH & Co. KGaA, Weinheim.

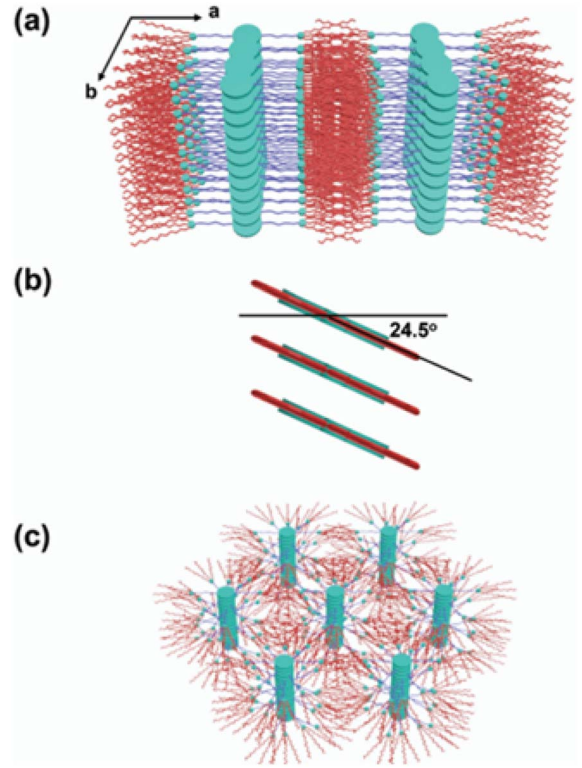

Fig. 35 Schematic packing model of p-HBC-6Si$_7$ LamCol$_r$ structure (a), LamCol$_r$ structure HBC core arrangement (b), and p-HBC-6Si$_7$ Col$_h$ structure schematic packing model (c). The ODMS chains and HBC cores are shown by the red lines and green discs, respectively.[167]

STM images in Fig. 34, distinct bright, disk-like patterns were observed. The broader STM images revealed that the molecular domains extended over several hundred square nanometers. Analysis of the STM data showed that the HBC-6BTZA molecules within the adlayer displayed two types of contrast, suggesting the formation of a true bilayer structure. The peripheral BTZ groups likely remained unresolved due to their dynamic behavior during the STM measurement timescale. Supporting these findings, two-dimensional wide-angle X-ray scattering (2D-WAXS) experiments also confirmed the vertical stacking of the molecular discs. As depicted in Fig. 33 **177**, similar stacking behavior was observed for a related HBC derivative adsorbed onto a gold substrate.[163]

Fan *et al.* (2022) designed and synthesized the organic–inorganic hybrid molecules p-HBC-4Si$_7$ (**116**) and p-HBC-6Si$_7$ (**117**), which feature different quantities of ODMS chains connected to the HBC core. The thermal stability of the two Block molecules is very high. Self-assembled structures exhibit a similar phase transition behavior, transitioning from the LamCol$_r$ phase to the Col$_h$ phase and ultimately to the Iso phase as the temperature increases. Fig. 35 illustrates that p-HBC-6Si$_7$ **117** has a larger unit size when their phase structures are identical and, as expected, a lower phase transition temperature than p-HBC-4Si$_7$ **116** when it has more ODMS chains. Moreover, their self-assembled bulk structures may be successfully converted into thin films. Sub-5 nm line patterns and flat sheets are produced by parallel supramolecular columns, as observed in thin films. The sub-5 nm nanostructures, which may be useful for nanopatterning, need further investigation. Expanding this family by designing additional HBC systems with ODMS groups positioned differently around the HBC core (such as three for C_3 symmetry, four for conjugated C_2 symmetry, or random placements) would be fascinating. It would also be worth investigating whether the LamCol$_r$ phase persists or if new mesophases emerge.[167]

4. Applications for HBCs

The big, disc-shaped polycyclic aromatic hydrocarbon (PAH) HBC has a strongly conjugated π-electron system, which makes it useful in optoelectronics, materials science, and nanotechnology.

4.1. Applications in organic and optoelectronics electronics

Müllen *et al.* (2012) synthesized and systematically investigated a series of fluorenyl-hexabenzocoronene (FHBC) and diketopyrrolopyrrole (DPP)-based compounds to develop liquid crystalline chromophores. All FHBC–DPP derivatives exhibited

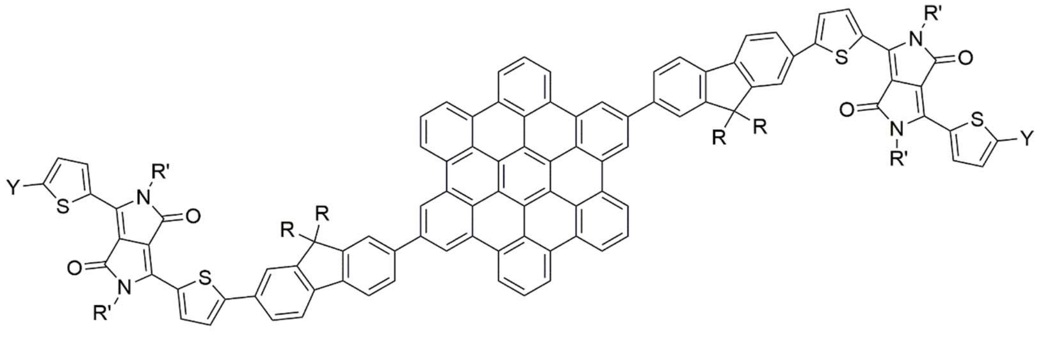

178 R = Octyl R' = 2-ethylhexyl Y= H 73%
179 R = Octyl R' = 2-ethylhexyl Y= Benzothiophene 74%
180 R = Octyl R' = 2-ethylhexyl Y= H 82%

Fig. 36 HBC derivatives for photovoltaic applications.[200]

supramolecular liquid crystalline organization, primarily driven by π–π stacking interactions among the FHBC units. The DPP moieties were responsible for extending the absorption into the visible region. Interestingly, minor structural modifications led to pronounced differences in molecular self-assembly. In particular, molecular extension in dyes **178** and **179** broadened their absorption compared to dye **178** alone; however, this also altered the molecular aspect ratio, resulting in distinct packing arrangements (Fig. 36). Dyes **179** and **180** adopted lamellar packing, while dye 174 formed columnar-structured extruded fibers. Despite these morphological differences, charge carrier mobilities measured *via* OFET and SCLC techniques were comparable across all dyes. Particularly, dye **178** demonstrated superior performance in bulk heterojunction (BHJ) solar cells fabricated under ambient conditions, achieving a high open-circuit voltage of 0.86 V and a power conversion efficiency of 1.59%. The observed variations in BHJ performance are attributed to differences in blend film morphology. This work highlights how subtle structural changes can significantly influence bulk properties, device efficiency, and molecular behavior.[200]

Mende *et al.* (2012) reported the application of a donor–acceptor system based on large PAHs for photovoltaic devices. Specifically, vacuum-sublimated HBC **1** was shown to exhibit a remarkably long exciton diffusion length of approximately 25 nm. In a novel approach, a photovoltaic device was constructed using nanographene derivatives as both donor and acceptor components, incorporating a hexafluorinated HBC analogue as the acceptor. This bilayer configuration yielded an unusually high open-circuit voltage of 1.39 V. Given that the employed photoactive materials absorb primarily at wavelengths below 500 nm (Fig. 37, **1** and **181**), the system demonstrates considerable potential for integration into multilayer or tandem solar cell architectures, as well as for the development of semi-transparent photovoltaic devices.[201]

Müllen *et al.* (2012) described the synthesis and detailed photophysical characterization of a series of rigidly connected dyads consisting of HBC as the electron donor and perylene-tetracarboxy diimide (PDI) as the electron acceptor, covalently joined *via* conjugated bridges. The study explored variations in the donor–acceptor stoichiometry and electronic characteristics of the linkers to assess their impact on self-assembly behavior and on the dynamics of energy and electron transfer processes. In both solution and solid states, these dyads exhibited a propensity to form highly ordered two-dimensional supramolecular structures, as confirmed by scanning tunneling microscopy (STM) and two-dimensional wide-angle X-ray scattering (2D-WAXS) analyses. The resulting nanostructures displayed tunable spatial arrangements between donor and acceptor units, governed by the molecular symmetry and design of the dyads. Depending on their symmetry, the molecules assembled into either columnar architectures with phase-segregated HBC and PDI domains or into interdigitated frameworks featuring alternating donor–acceptor motifs, as shown in Fig. 38. Spectroscopic measurements indicated that upon excitation of the HBC moiety, photoinduced electron transfer to the PDI unit occurred only when adequate orbital overlap was ensured through close π–π stacking. In contrast, configurations lacking sufficient electronic coupling predominantly favored Förster resonance energy transfer (FRET). While interdigitated assemblies supported efficient energy delocalization, directional charge transport across the bulk phase was achieved exclusively in the segregated columnar systems. These findings emphasize the critical role of molecular architecture in dictating the optoelectronic properties of donor–acceptor dyads and provide strategic insights for their implementation in organic field-effect transistors (OFETs) and bulk heterojunction photovoltaic devices.[202]

Li *et al.* (2016) investigated the integration of HBC, a discotic π-conjugated molecule recognized for its pronounced self-assembling characteristics, strong π–π stacking ability, and notable charge carrier mobility, into organic photovoltaic (OPV) applications. Despite these advantageous properties, small-molecule HBC derivatives have generally underperformed in terms of power conversion efficiency (PCE) in OPV systems. To overcome these limitations, the authors synthesized a series of novel copolymers by combining HBC units bearing bulky

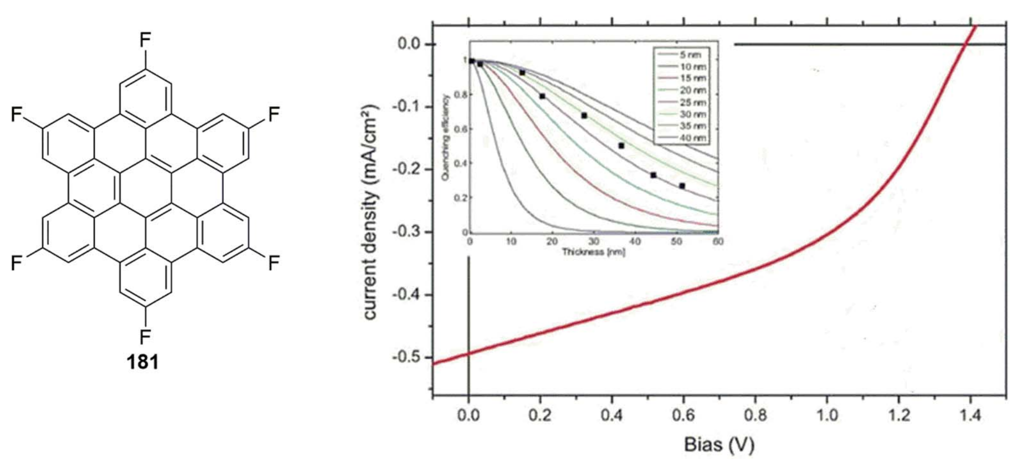
181

Fig. 37 Devices based on vacuum sublimated HBC and their photovoltaic performance. Reproduced from ref. 201 with permission from John Wiley & Sons, Copyright © 2012, Wiley-VCH Verlag GmbH & Co. KGaA, Weinheim.

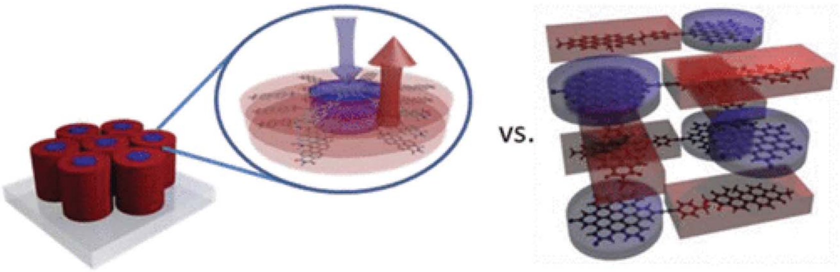

Fig. 38 Schematic representation of the columnar stacks of star-shaped dyads (left) and interdigitating stacks of the linear dyad (right). Reproduced from ref. 202 with permission from American Chemical Society, Copyright © 2012.

mesityl substituents with diketopyrrolopyrrole (DPP), an electron-deficient acceptor unit. These copolymers incorporated varying π-bridging motifs and alkyl side chains, leading to the generation of four distinct materials: PHBCDPPC20, PHBCDPPC8, PHBCDPPF, and PHBCDPPDT. The introduction of the DPP segment into the polymer backbone contributed to broadening the absorption spectra and reducing the optical band gaps. Furthermore, the steric hindrance provided by the mesityl groups on the HBC core effectively limited over-aggregation, promoting finer phase separation in the active layers of OPV devices. The electronic and structural nature of the π-bridging units significantly influenced the coplanarity of the polymer backbone and the extent of conjugation. Among the synthesized materials, PHBCDPPDT, incorporating a bithiophene spacer, exhibited the most extensive absorption range due to its enhanced planarity and extended π-delocalization compared to its thiophene-bridged analogue. Charge transport characteristics, evaluated *via* field-effect transistor measurements, revealed hole mobilities of 1.35×10^{-3}, 2.31×10^{-4}, 2.79×10^{-4}, and 8.60×10^{-3} cm^2 V^{-1} s^{-1} for PHBCDPPC20, PHBCDPPC8, PHBCDPPF, and PHBCDPPDT, respectively. Correspondingly, OPV devices fabricated from these polymers achieved PCEs of 2.12%, 2.85%, 1.89%, and 2.74%, as presented in Fig. 39. Especially, the polymer PHBCDPPC8 attained the highest recorded efficiency among HBC-based photovoltaic systems, with a PCE of 2.85%. This study offers a promising design approach for the development of efficient HBC-containing conjugated polymers, advancing the potential of these materials for next-generation OPV applications.[203]

Li *et al.* (2016) explored the development of high-performance D–A optoelectronic materials by employing HBC as the donor and benzothiadiazole (BT) as the acceptor unit, as illustrated in Fig. 40. The study focused on three molecular architectures with varying D–A arrangements: DA, ADA (specifically BHB **182**), and DAD. Among these, the ADA-type molecule (BHB **182**) demonstrated superior properties, including more ordered molecular packing in thin films and significantly broader and stronger absorption in the UV-visible region. These structural advantages translated into enhanced performance in both OFETs and OPV devices when compared to the DA and DAD analogues. Despite these findings, the realization of high-efficiency HBC-based D–A molecular systems remains a substantial challenge, as none of the tested devices have yet achieved performance metrics suitable for practical applications.[204]

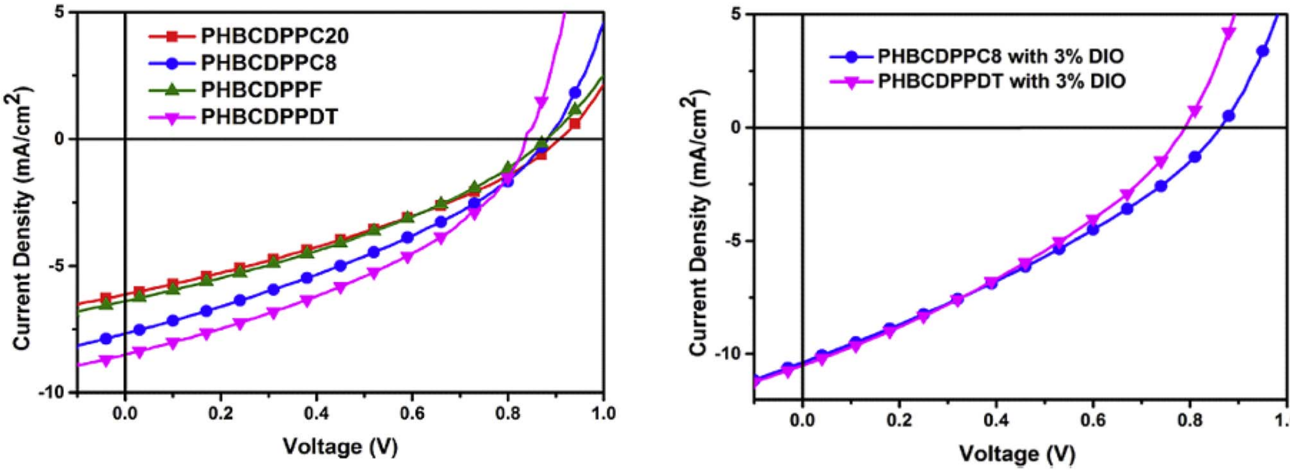

Fig. 39 (Left) Current density–voltage characteristics of polymer/PC$_{71}$BM-based PSCs with AM 1.5 G, 100 mW cm^{-2} illumination (right) features of the current density and voltage of PSC devices of PHBCDPPC8 and PHBCDPPDT following processing with DIO additive under 100 mW cm^{-2} of AM 1.5 G illumination. Reproduced from ref. 203 with permission from Elsevier, Copyright © 2016.

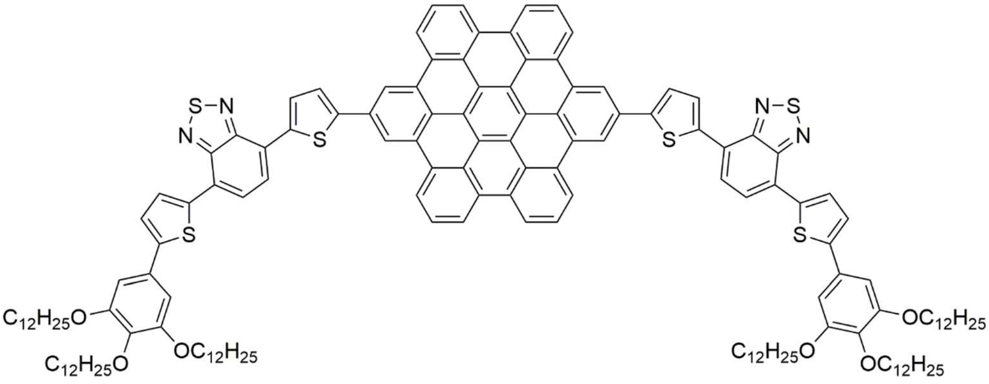

BHB
182

Fig. 40 Molecular structure of BHB.[204]

Tao *et al.* (2019) investigated the semiconducting potential of two discotic liquid crystalline compounds—HBC-1,3,5-Ph-C_{12} and HBC-1,2,4-Ph-C_{12}—for application in OTFTs. These molecules, owing to their planar aromatic cores, exhibit the ability to self-assemble into columnar mesophases through strong π–π stacking, facilitating one-dimensional charge transport. Thin films were fabricated *via* a brush-coating technique, which enabled the alignment of columnar domains along the direction of coating. Among the two derivatives, HBC-1,3,5-Ph-C_{12}, possessing higher molecular symmetry, showed superior molecular ordering when deposited on silicon substrates modified with self-assembled monolayers (SAMs). Particularly, films cast on octadecyltrichlorosilane (OTS)-treated surfaces adopted an edge-on orientation, displaying enhanced crystallinity and a pronounced dichroic ratio. Field-effect transistors derived from these aligned films achieved a maximum charge carrier mobility of 0.1 $cm^2 V^{-1} s^{-1}$ and an average value of 0.083 $cm^2 V^{-1} s^{-1}$ exceeding by nearly two orders of magnitude the mobilities observed in devices fabricated through conventional spin-coating methods. In contrast, the less symmetrical HBC-1,2,4-Ph-C_{12} yielded films with discernible intra- and inter-columnar order, albeit with reduced structural organization and electronic performance. Devices based on this derivative exhibited peak and average mobilities of 0.056 $cm^2 V^{-1} s^{-1}$ and 0.038 $cm^2 V^{-1} s^{-1}$, respectively, as depicted in Fig. 41. This work highlights an efficient, scalable approach for inducing directional alignment in HBC-based discotic materials, thereby advancing the development of high-performance OTFTs.[205]

Tao *et al.* (2019) reported the successful synthesis and structural characterization of a series of functionalized hexa-*cata*-HBC derivatives, as illustrated in Fig. 42. It was observed that the nature of the peripheral substituents exerted a more pronounced influence on the crystal packing arrangements than on intrinsic molecular properties such as oxidation potentials and UV-visible absorption characteristics. Single-crystal X-ray diffraction analysis revealed that the substituent type modulates the degree of twist in the peripheral benzene rings surrounding the HBC core. While the structural

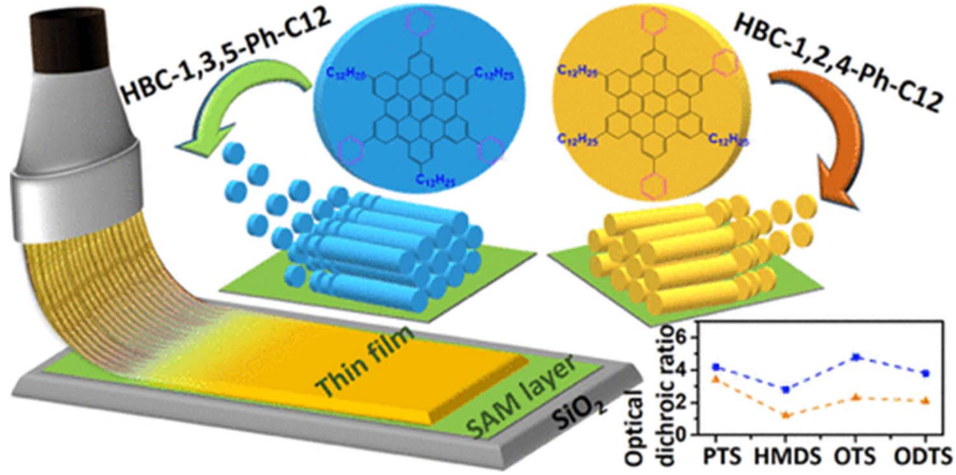

Fig. 41 Graphical representation of brush-coated molecularly aligned HBCs films and application in thin-film transistors. Reproduced from ref. 205 with permission from American Chemical Society, Copyright © 2019.

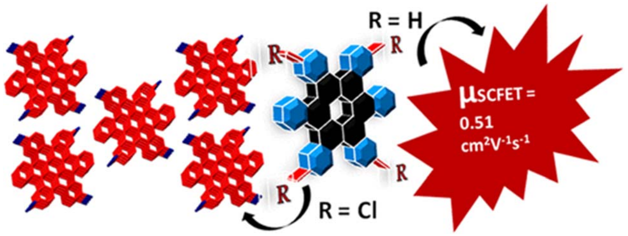

Fig. 42 Graphical representation of polysubstituted hexa-*cata*-HBC and its applications in transistors. Reproduced from ref. 206 with permission from American Chemical Society, Copyright © 2019.

distortions at the fjord regions remained largely unaffected by peripheral functionalization, variations in substituent size, dipole moment, and heteroatom content significantly altered the overall molecular packing. The parent HBC compound demonstrated p-type semiconducting behavior, with field-effect mobilities ranging from 0.34 to 0.51 cm^2 V^{-1} s^{-1} and on/off current ratios between 10^5 and 10^7. Especially, thin-film transistors incorporating MeHBC-2 achieved a peak hole mobility of 0.61 cm^2 V^{-1} s^{-1} with an on/off ratio of 10^6. These results underscore the potential of tailored HBC derivatives as effective charge-transport materials for OFET applications.[206]

Wöll *et al.* (2024) reported the fabrication of HBC-incorporated metal–organic framework (MOF) thin films using a layer-by-layer assembly technique (Fig. 43). Addressing the aggregation challenges of large polycyclic aromatic systems like HBC, the team employed controlled MOF synthesis to create highly oriented, uniform thin films. Both HBC and its non-annulated analog, hexaphenylbenzene (HPB), were integrated into crystalline frameworks *via* customized linkers. Optical studies revealed strong electronic coupling between chromophores within the SURMOF structures, indicating efficient excitonic interactions. Photoconductivity tests showed that Cu-based SURMOFs outperformed their Zn counterparts, exhibiting superior charge separation and faster photoresponse, likely due to enhanced ligand-to-metal charge transfer at the Cu centers. These results underscore the potential of HBC-based SURMOFs in optoelectronic applications and emphasize the influence of metal node selection on device performance.[207]

4.2. Energy storage devices and supercapacitors

Ma *et al.* (2015) reported a facile, cost-effective approach to fabricate self-assembled fibrous aggregates of HBC on indium tin oxide (ITO) substrates *via* chronoamperometric electrochemical deposition (Fig. 44). These fibers, ~70 nm in diameter, consist of columnar π–π-stacked HBC molecules aligned longitudinally, forming a porous morphology that enhances ion transport and rapid charge–discharge performance. Electrochemical analysis showed excellent capacitance stability, with an initial slight decline during the first 200 cycles attributed to the loss of loosely bound, low-molecular-weight HBC molecules. Subsequently, capacitance stabilized, indicating robust structural integrity of the HBC network. These results highlight the promise of electrochemically assembled HBC films as high-performance supercapacitor electrodes and demonstrate the viability of *in situ* synthesis of large planar PACs for energy storage applications.[208]

Müllen *et al.* (2017) developed a bottom-up, wafer-scale method to synthesize ultrathin, continuous sulfur-doped graphene (SG) films using sulfur-functionalized nanographene precursors and a thin gold layer as a 2D confinement template (Fig. 45). This approach enabled precise control over film morphology and uniform sulfur doping. The SG films exhibited enhanced interlayer spacing, high electrical conductivity, and outstanding electrochemical performance, including a time constant of 0.26 ms, power density of ~1191 W cm^{-3}, volumetric capacitance of ~582 F cm^{-3}, and stability at scan rates up to 2000 V s^{-1}. These properties make the films promising for applications in micro-supercapacitors, electrochemical sensors, metal-free oxygen reduction catalysts, and energy storage devices such as lithium–sulfur batteries.[209]

Jin *et al.* (2019) demonstrated that the self-assembly of HBC with optimal *d*-spacing significantly enhances lithium-ion battery (LIB) anode capacity and cycling stability due to HBC's

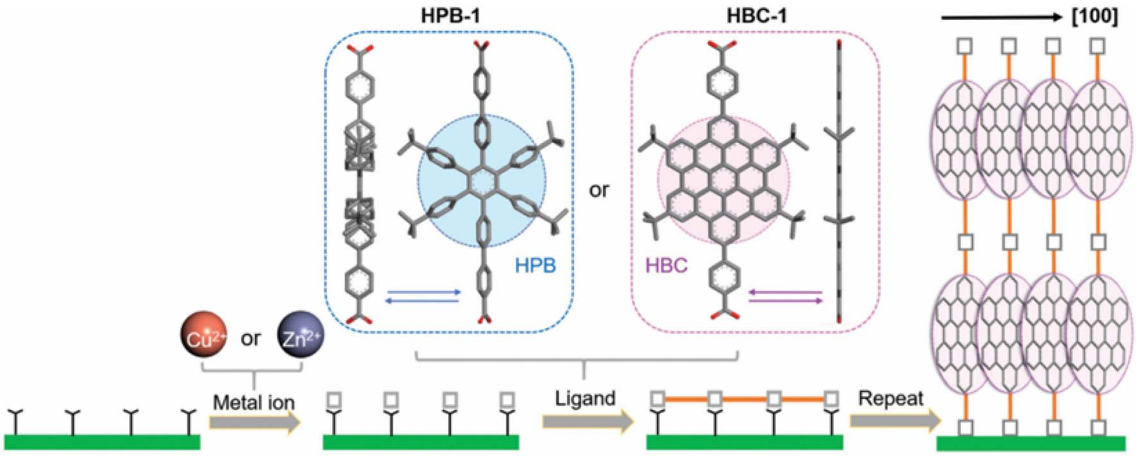

Fig. 43 Diagrammatic representation of the layer-by-layer synthesis of SURMOFs based on HPB-1 and HBC-1 linkers. Reproduced from ref. 207 with permission from John Wiley & Sons, Copyright © 2024, Wiley-VCH Verlag GmbH & Co. KGaA, Weinheim.

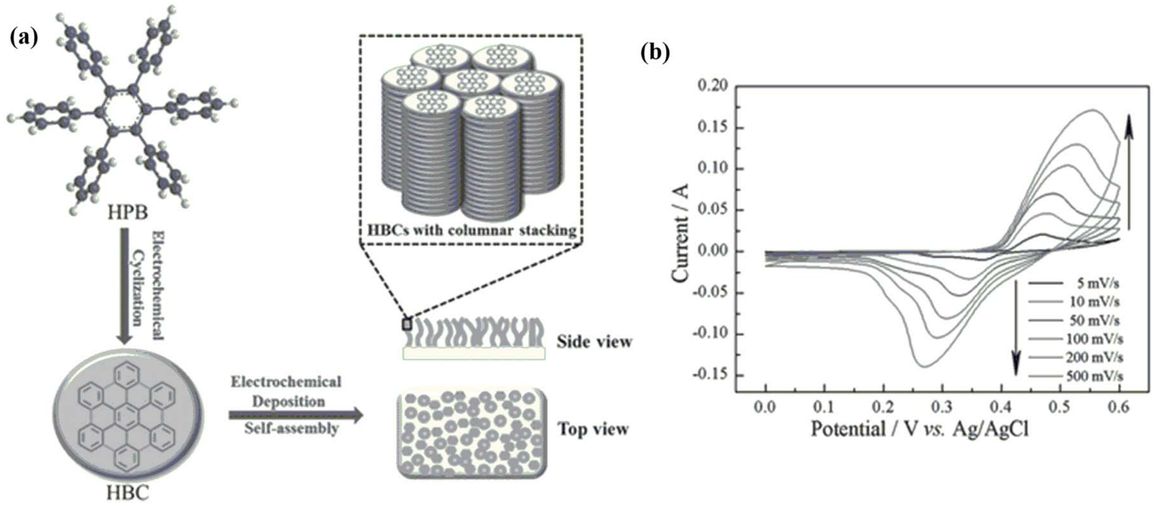

Fig. 44 (a) Diagram showing the assembling of HBC on an electrode and it's *in situ* electrochemical production. (b) Representative cyclic voltammograms of the HBC assembly on ITO, obtained in a 6 M KOH solution at different scan speeds between 5 and 500 mV s^{-1}. Reproduced from ref. 208 with permission from John Wiley & Sons, Copyright © 2015, Wiley-VCH Verlag GmbH & Co. KGaA, Weinheim.

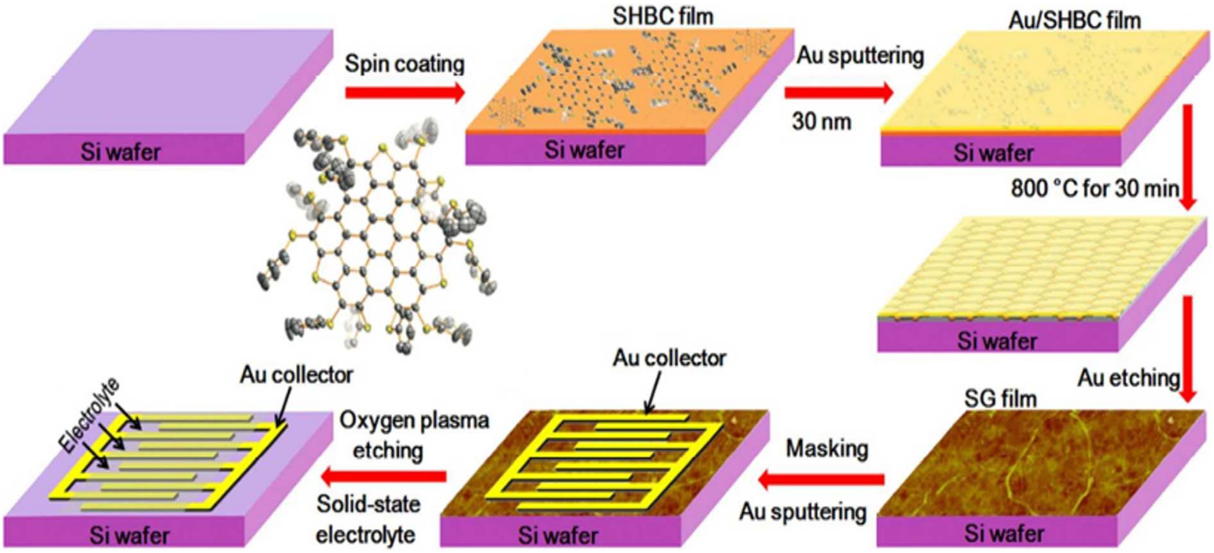

Fig. 45 Diagrammatic representation of SG films for planar MSCs on a Si/SiO$_2$ wafer produced from SHBC. Reproduced from ref. 209 with permission from American Chemical Society, Copyright © 2017.

strong structural durability. Their study revealed a clear structure–property relationship between lithium storage performance and functional group type. The self-assembly process involves angular rearrangement of graphene nanosheets under applied energy, facilitating lithium ion diffusion both between and through graphene layers, as supported by TEM analysis (Fig. 46). This hierarchical nano-graphene architecture exhibits excellent lithium storage and diffusion capabilities. Future research will focus on understanding the microscopic interior structure and the dynamic hierarchical self-assembly of individual nano-graphene sheets to optimize battery performance and utilization.[210]

Beheshtian *et al.* (2020) used DFT to assess pristine and doped HBC nanographenes—B-HBC, N-HBC, and BN-HBC—as anode materials for sodium-ion batteries (NIBs). Calculated Na$^+$ adsorption energies were −33.2, −29.8, −43.6, and −31.2 kcal mol^{-1} for HBC, B-HBC, N-HBC, and BN-HBC, respectively, while neutral Na adsorption energies were near −0.8, −41.9, −0.5, and −0.5 kcal mol^{-1} as shown in Fig. 47. Results highlight the key role of doping: nitrogen enhances Na$^+$ adsorption and suppresses neutral Na binding, increasing cell voltage (∼1.87 V for N-HBC), whereas boron favors neutral Na adsorption, lowering voltage (−0.53 V for BN-HBC). Pristine HBC showed intermediate behavior (∼1.41 V). These findings indicate N-doped HBC as a promising anode candidate for NIBs due to its favorable electronic properties and high voltage. Given the limitations of lithium-ion batteries, sodium-ion

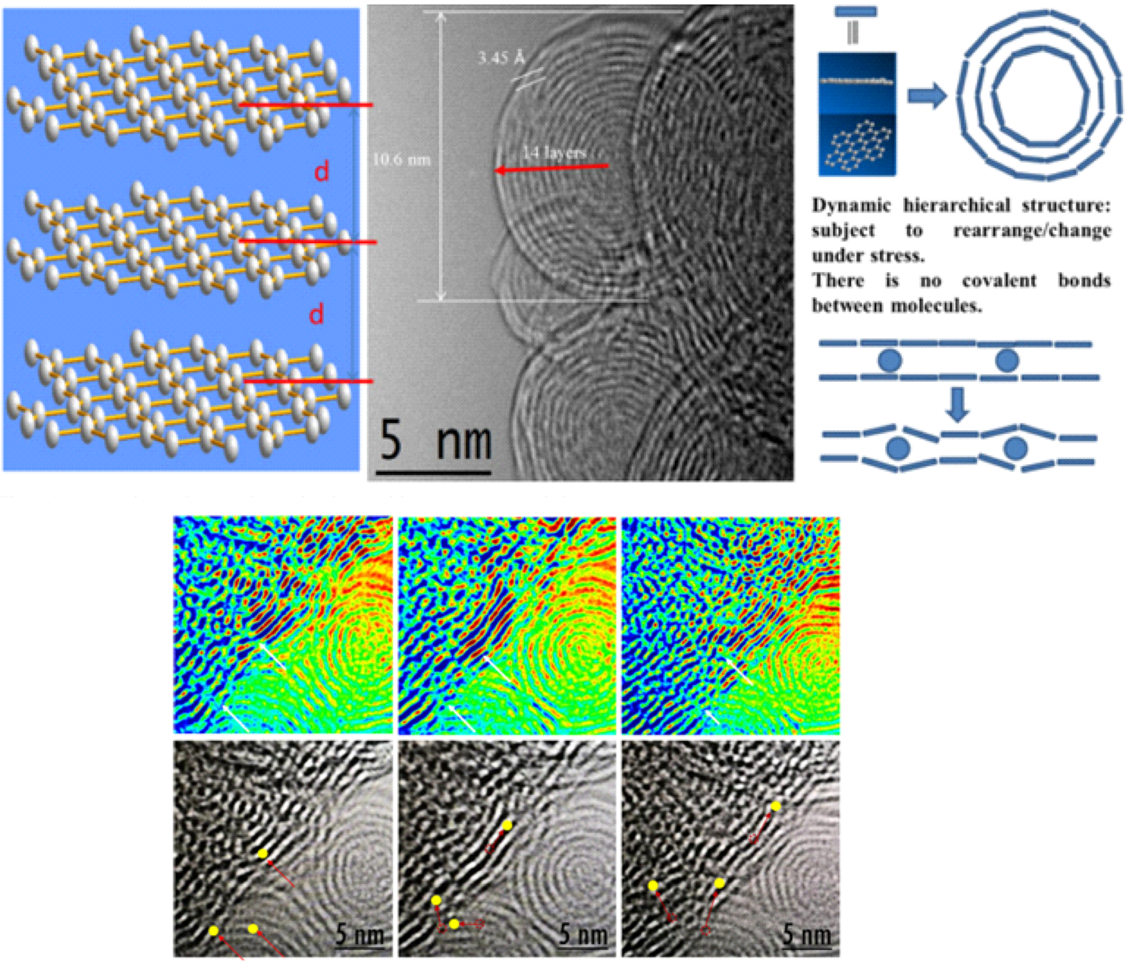

Fig. 46 Dynamic hierarchical assembly of nano-graphene to reorganize and modify (above) and TEM picture of the multi-stage self-assembly structure of nanographene (below) Reproduced from ref. 210 with permission from Springer, Copyright © 2019.

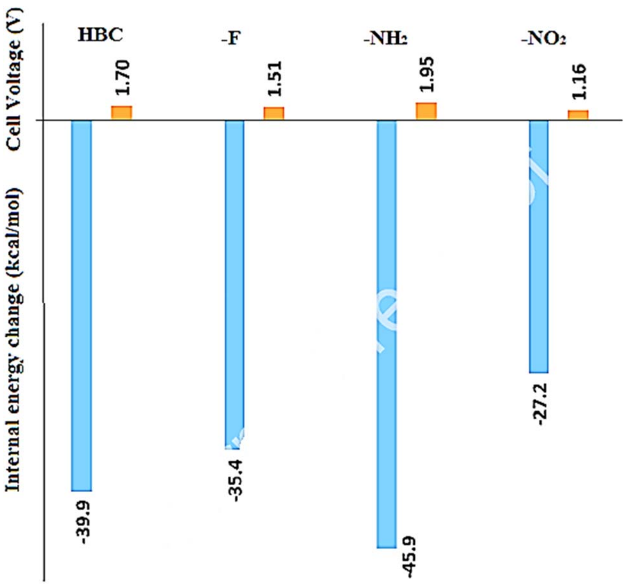

Fig. 47 Li-ion battery cell voltage and the plot of eternal energy change for Li and Li^+ adsorption on various HBC-based nanosheets. Reproduced from ref. 212 with permission from Elsevier, Copyright © 2020.

systems offer an attractive, cost-effective, and safer alternative for future energy storage.[211]

Soleymanabadi *et al.* (2020) used DFT to assess pristine HBC and its functionalized derivatives ($–NO_2$, $–NH_2$, and –F substituted) as anode materials for lithium-ion batteries (LIBs). Both neutral Li and Li^+ preferentially adsorb on the peripheral rings of HBC, with adsorption energies of -53.7 kcal mol^{-1} and -13.8 kcal mol^{-1}, respectively. Li^+ adsorption increases the nanographene's work function, while Li adsorption decreases it. The calculated cell voltage for pristine HBC anodes is about 1.70 V, which rises by 0.25 V upon $–NH_2$ functionalization, indicating improved performance. In contrast, $–NO_2$ substitution lowers the voltage to ∼1.16 V, suggesting reduced electrochemical suitability. Overall, NH_2-functionalized HBC shows the most favorable properties for LIB anode applications, as summarized in Fig. 47.[212]

Due to limitations of lithium-ion batteries, there is growing interest in alternative battery technologies with higher energy density and lower cost. Calcium-ion batteries (CIBs) have attracted attention because of calcium's abundance and higher cell voltages. Buenaño *et al.* (2024) employed DFT to evaluate the potential of HBC nanographene and its doped derivatives

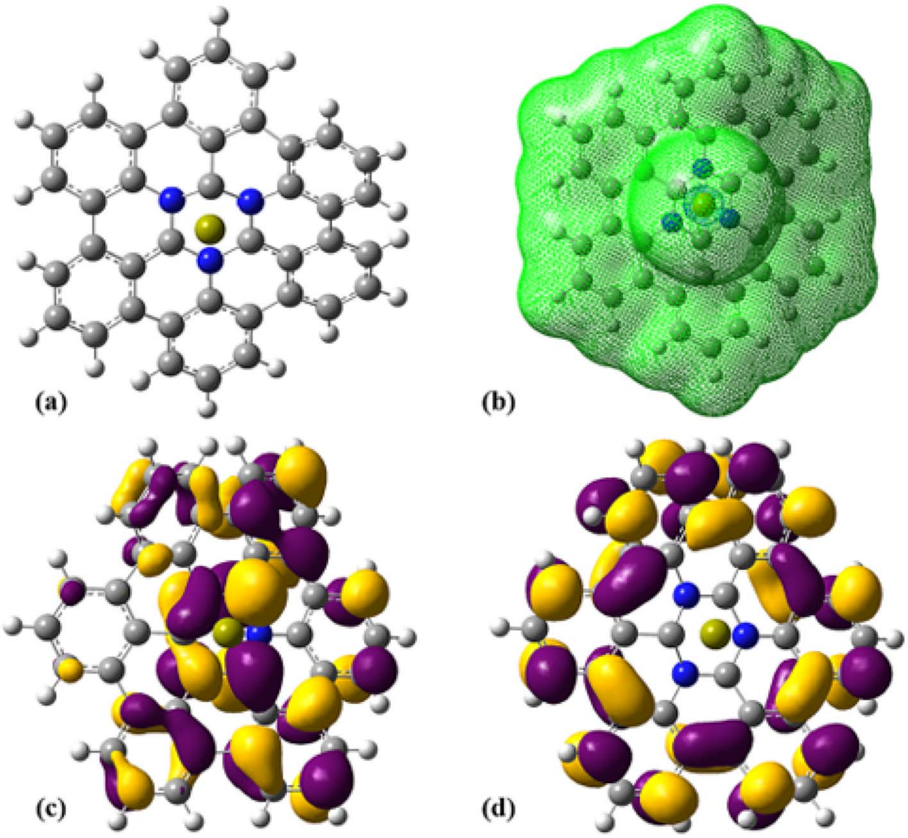

Fig. 48 The most stable N-HBC:Ca complex's (a) optimized framework, (b) MEP plot, (c) HOMO, and (d) LUMO profiles. Reproduced from ref. 213 with permission from Elsevier, Copyright © 2024.

(N-, BN-, and AlN-HBC) as anode materials for CIBs. The study found that nitrogen doping significantly increased the cell voltage (V_{cell}), while BN doping had minimal effect. The calculated cell voltages followed the trend: N-HBC (~1.01 V) > AlN-HBC (~0.63 V) > HBC (~0.56 V) > BN-HBC (~0.52 V), as depicted in Fig. 48. These results suggest that N-HBC is a promising anode candidate for CIBs. Overall, the findings highlight the potential of N-HBC-based CIBs as alternatives to current battery technologies, warranting further investigation and development in this area.[213]

Sun *et al.* (2025) used DFT to investigate the adsorption of Li^+, Li, Mg^{2+}, and Mg on twelve pristine and doped HBC nanostructures, including N-, BN-, and Si-substituted variants as shown in Fig. 49. Molecular electrostatic potential analysis showed that doping with heteroatoms increased the electron density of HBC frameworks. Both doped and undoped HBC exhibited strong affinity for cations, particularly Li^+ and Mg^{2+}, with adsorption energies ranging from −47.65 kcal mol^{-1} (Li^+ on $B_{21}H_{18}N_{21}$) to −47.44 kcal mol^{-1} (Mg^{2+} on m-$C_{40}H_{18}N_2$). A correlation between lower minimum MESP values and weaker electrostatic interactions was observed. Charge transfer analysis confirmed electron donation from the nanoflakes to the adsorbed cations. For neutral metals, adsorption energies varied widely, from −33.94 kcal mol^{-1} (Li on $C_{38}H_{18}B_2N_2$) to −2.14 kcal mol^{-1} (Mg on $B_{21}H_{18}N_{21}$). Among the materials studied, $B_{21}H_{18}N_{21}$ showed the highest cell voltage for lithium-ion batteries (1.90 V), while m-$C_{40}H_{18}N_2$ achieved the highest voltage for magnesium-ion batteries (5.29 V). The study concluded that cell voltage in LIBs is mainly governed by neutral metal adsorption energy, whereas in MIBs, it is more influenced by cation adsorption energy.[214]

4.3. Catalysis and chemical sensing

Kumar *et al.* (2013) synthesized two HBC-based derivatives incorporating dual rotors to achieve controlled aggregation-induced enhanced emission (AIEE) by adjusting water content in the aggregation medium. Both derivatives formed aggregates that exhibited highly sensitive and selective detection of picric acid. The study also explored their distinct quenching mechanisms, influenced by the functional groups attached to the coronene core. Both compounds demonstrated high Stern–Volmer constants and low detection limits, essential for practical chemosensor applications. Additionally, they showed efficient fluorescence quenching in response to picric acid vapor at room temperature, broadening their sensing capabilities. Fluorescent test strips incorporating these aggregates were developed, capable of detecting picric acid at attogram sensitivity.[215]

Yin *et al.* (2014) developed pH-responsive perylene-cored amphiphilic polymers (APHPs) to investigate self-assembly driven by π–π interactions of end groups and pH-sensitive

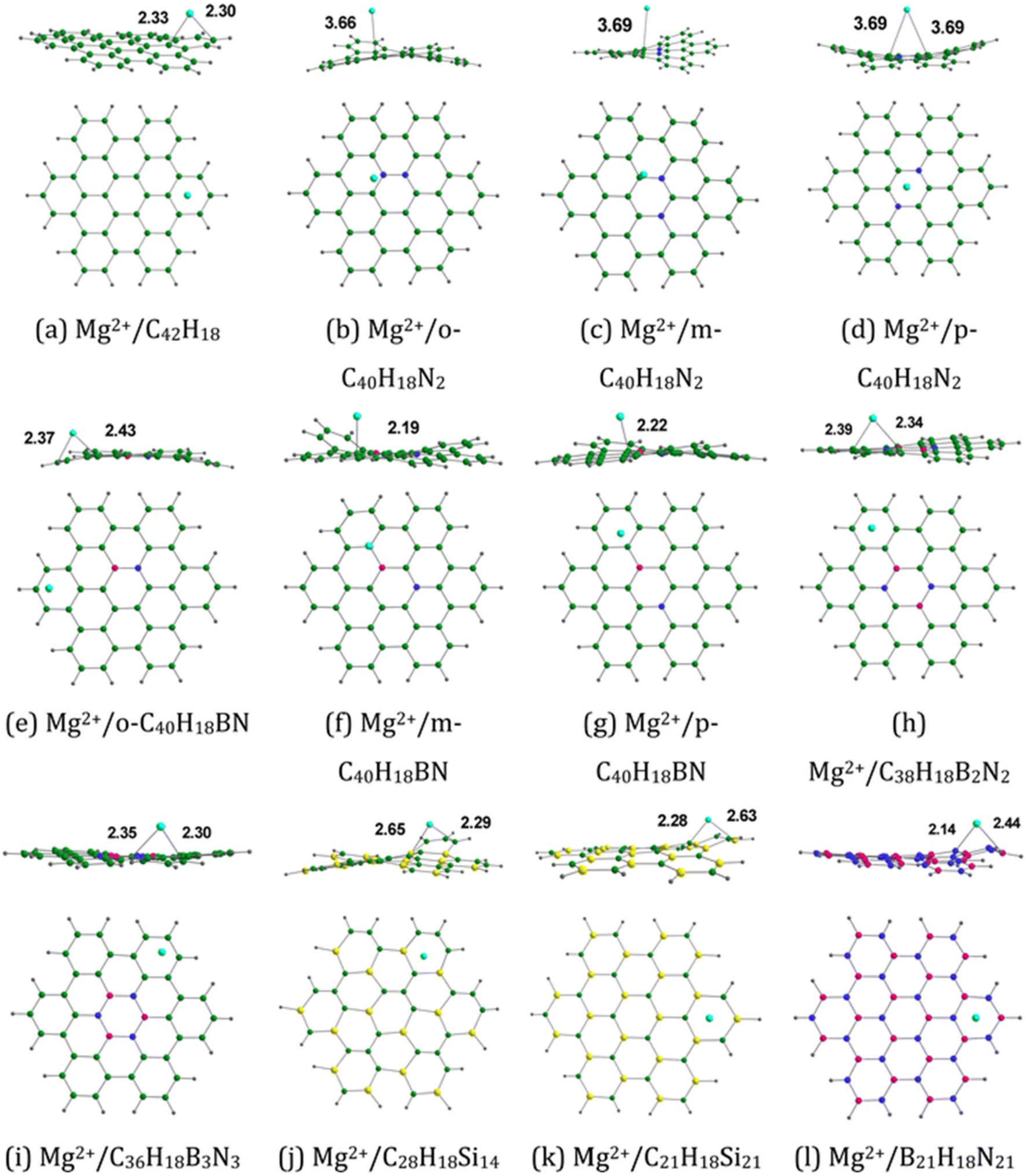

Fig. 49 Optimized structures of Mg adsorbed on (a) $C_{42}H_{18}$, (b) *o*-$C_{40}H_{18}N_2$, (c) *m*-$C_{40}H_{18}N_2$ (d) *p*-$C_{40}H_{18}N_2$, (e) *o*-$C_{40}H_{18}BN$, (f) *m*-$C_{40}H_{18}BN$, (g) *p*-$C_{40}H_{18}BN$, (h) $C_{38}H_{18}B_2N_2$, (i) $C_{36}H_{18}B_3N_3$, (j) $C_{28}H_{18}Si_{14}$, (k) $C_{21}H_{18}Si_{21}$, and (l) $B_{21}H_{18}N_{21}$. Reproduced from ref. 214 with permission from the Royal Society of Chemistry.

polymers at the micrometer scale. In these APHPs, flexible poly(amino ethyl methacrylate) (polyAEMA) served as a hydrophilic, pH-responsive segment, while perylene-3,4-dicarboxylic acid monoimide (PMI) provided a large, rigid hydrophobic core. PolyAEMA transitioned from flexible Gaussian coils to aggregated micelles in aqueous solution with pH changes. Below the pK_a, electrostatic repulsion maintained polymer coils; at pH near pK_a, combined electrostatic repulsion and π–π stacking induced micelle formation. Above pK_a, micelles further aggregated, and solvent evaporation led to flower-like self-assembled structures.[216]

Salari *et al.* (2017) employed DFT calculations to investigate the electronic sensitivity, reactivity, and structural properties of HBC toward NO_2 gas. Several energetically favorable NO_2/BNG complexes were identified, including two cycloaddition and one nitro configuration. Unlike graphene, HBC's electronic properties exhibit high sensitivity to NO_2 adsorption, causing a semiconductor-to-semimetal transition and a ∼62.6% reduction in its band gap. These results suggest HBC's potential as an effective NO_2 sensor. Moreover, NO_2 desorption at room temperature is rapid, occurring within 1.9 ns. HBC selectively

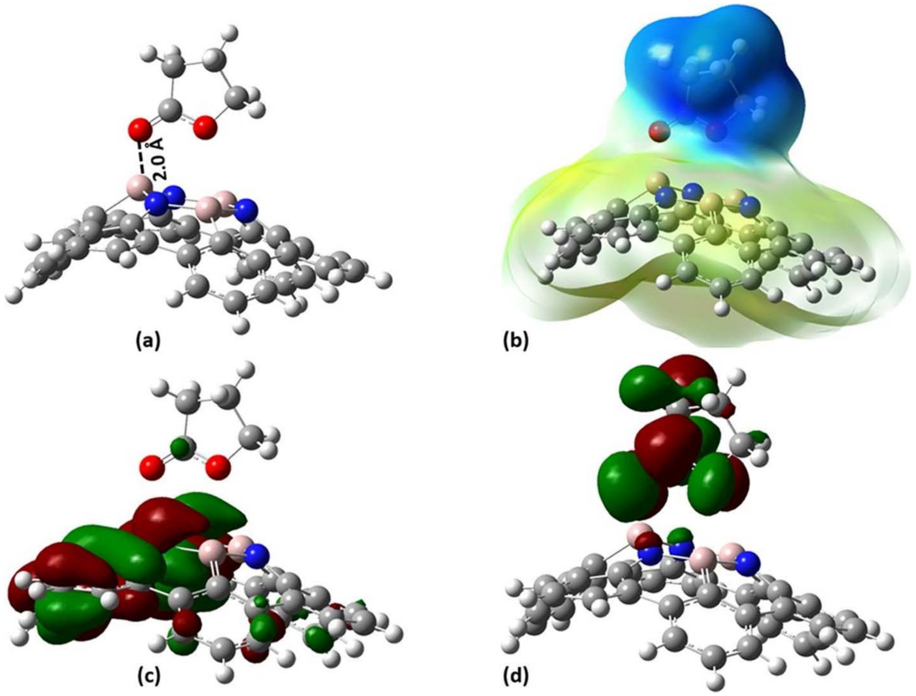

Fig. 50 AlN-HBC:GBL complex's (a) optimized structure, (b) MEP, (c) HOMO, and (d) LUMO profiles. Distances are measured in Å. Reproduced from ref. 219 with permission from Elsevier, Copyright © 2021.

detects NO_2 in the presence of H_2, showing minimal interference from N_2, H_2O, O_2 (triplet), and CO_2 molecules.[217]

Vatanparast *et al.* (2018) investigated NH_3 adsorption on pristine and B- and Al-doped HBC using B3LYP/6-31G(d) calculations. The study analyzed adsorption energies, thermodynamic parameters, binding distances, charge transfer, band gap variations, DOS, QTAIM, and NCI data. NH_3 weakly adsorbs on pristine HBC but shows significantly stronger adsorption on B- and Al-doped HBCs. Notably, B-doped HBCs exhibited a substantial band gap increase upon NH_3 adsorption, indicating high sensitivity, with m-$B_2C_{40}H_{28}$ displaying the largest band gap enhancement of 78.8%. In contrast, Al-doped HBCs showed negligible band gap changes. These findings suggest B-doped HBCs as promising candidates for ammonia sensing applications.[218]

Ebrahimiasl *et al.* (2021) employed DFT to study the sensing properties of BN- and AlN-doped HBC nanostructures toward gamma-butyrolactone (GBL) (Fig. 50). GBL adsorbs weakly on BN-HBC with an adsorption energy of 20.0 kcal mol^{-1}, causing minimal changes in HOMO–LUMO levels, band gap, and work function, indicating limited sensing capability. In contrast, GBL strongly binds to the AlN-doped site *via* its carbonyl oxygen with an adsorption energy of $\sim$44.1 kcal mol^{-1}, leading to a significant increase in electrical conductance (by 1.6×10^{9}). Desorption times suggest BN-HBC offers rapid recovery (4.4×10^{-2} s), whereas AlN-HBC exhibits strong retention (2.0×10^{16} s).

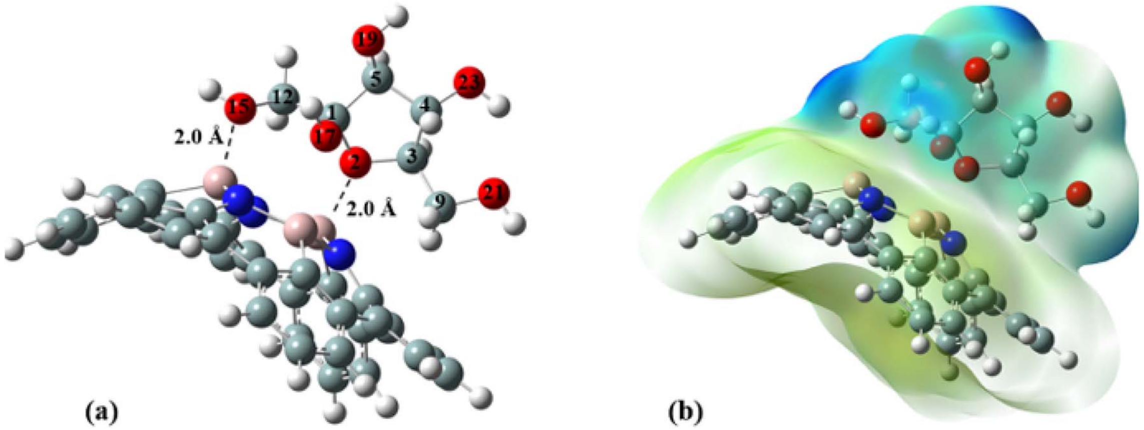

Fig. 51 AlN-HBC:FRU complex's (a) optimized structure and (b) MEP profile. Distances are measured in Å. Reproduced from ref. 220 with permission from Elsevier, Copyright © 2022.

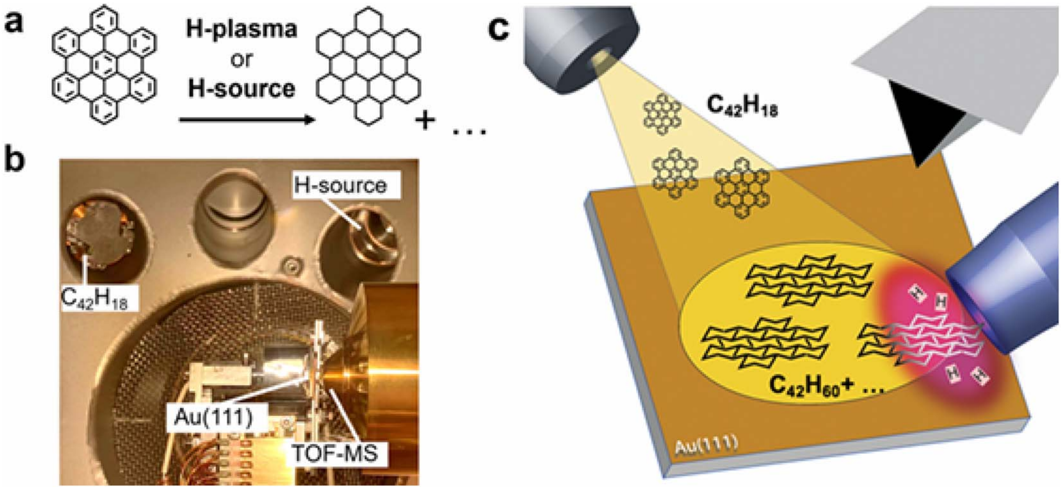

Fig. 52 (a) Hydrogenation of HBC nanographene in the direction of an archetype ((b) and (c)) Au(111) sample at the EI-TOF-MS measurement location within the chamber. Reproduced from ref. 221 with permission from American Chemical Society, Copyright © 2023.

Solvent effects decreased AlN-HBC:GBL complex stability by ~4.8 kcal mol^{-1}. Adsorption studies of gamma-hydroxybutyrate and 1,4-butanediol on AlN-HBC confirmed its selective sensing potential for GBL amid similar molecules.[219]

Awwad *et al.* (2022) employed DFT calculations to evaluate the potential of pristine and doped HBC nanographene structures as glucose (GLU) sensors, as depicted in Fig. 51. The computations were conducted using the B3LYP functional combined with the 6-31+G(d) basis set, incorporating Grimme's dispersion correction to accurately account for van der Waals interactions. Results indicated that both undoped HBC and BN-doped HBC exhibited negligible electronic sensitivity toward GLU, as the adsorption of GLU molecules did not significantly alter the HOMO or LUMO energy levels. In contrast, AlN-doped HBC demonstrated notable sensitivity upon GLU adsorption. Specifically, the electrical conductance of the AlN-HBC complex increased by a factor of approximately 1.2×10^2, while the energy gap (E_g) decreased by about 18.48%. To better approximate experimental conditions, further calculations were performed using an implicit solvent model for AlN-HBC, GLU, and the AlN-HBC:GLU complex. These simulations suggested weak interaction between GLU and the AlN-HBC surface due to solvation effects, wherein GLU molecules were predominantly stabilized by surrounding solvent molecules. To assess the selectivity of AlN-HBC in the presence of potential interfering agents, the adsorption behavior of fructose (FRU) on AlN-HBC was also investigated. The results showed that while the LUMO energy level increased from 1.11 eV (bare AlN-HBC) to 1.29 eV upon FRU adsorption, the HOMO level remained largely unchanged. These findings imply that AlN-HBC is capable of distinguishing GLU from FRU, highlighting its potential selectivity and applicability as a glucose sensor.[220]

Müllen *et al.* (2023) investigated the hydrogenation of HBC using Raman spectroscopy, EI-TOF mass spectrometry, and STM on Au(111)-supported PAHs (Fig. 52). Exposure to atomic hydrogen introduced C(sp^3)–H vibrational modes near 2900 cm^{-1} in naphthalene films, confirmed by decreased molecular mass. Hydrogenation of HBC monolayers and multilayers led to enhanced D and G Raman bands, indicating defect formation and partial sp^3 hybridization. STM revealed heterogeneous hydrogen coverage across HBC domains. Mass spectrometry identified fully hydrogenated $C_{42}H_{60}$ species after plasma treatment, confirming complete saturation. DFTB-MD simulations elucidated the random nature of hydrogen attachment and suggested that external factors like pressure or photoexcitation can facilitate thermodynamically favored hydrogenation. These results provide key insights for developing hybrid synthesis methods of hydrogenated nanographenes and nanodiamonds.[221]

4.4. HBCs in bioimaging and drug delivery

Zheng *et al.* (2007) synthesized a novel HBC-based chromophore (**25**) with enhanced two-photon absorption capabilities. This chromophore was incorporated into polymeric micelles to achieve water-compatible formulations. Concurrently, magnetic Fe_3O_4 nanoparticles were co-encapsulated within the micelles (Fig. 53), enabling magnetically guided cellular imaging under two-photon excitation. The system's efficiency arises from the micelles' uniform encapsulation and preservation of the chromophore's high two-photon fluorescence quantum yield.[132]

Müllen *et al.* (2009) demonstrated the use of HBC functionalized with distinct groups for bioprobing applications (Fig. 54). The negatively charged fiber surfaces of HBC facilitate the capture of positively charged biomolecules through electrostatic interactions. This two-step assembly represents the first example of an HBC derivative forming fibers suitable as a platform for biomolecule functionalization. The approach offers a novel strategy for designing diverse HBC analogs with tailored functional groups for targeted biological sensing.[222]

Shen *et al.* (2018) developed Fe_3O_4/HBC@F127 nanocomposites with water dispersibility, designed as multifunctional agents for both magnetic resonance (MR) and fluorescence imaging of cancer cells (Fig. 55). *In vitro* studies

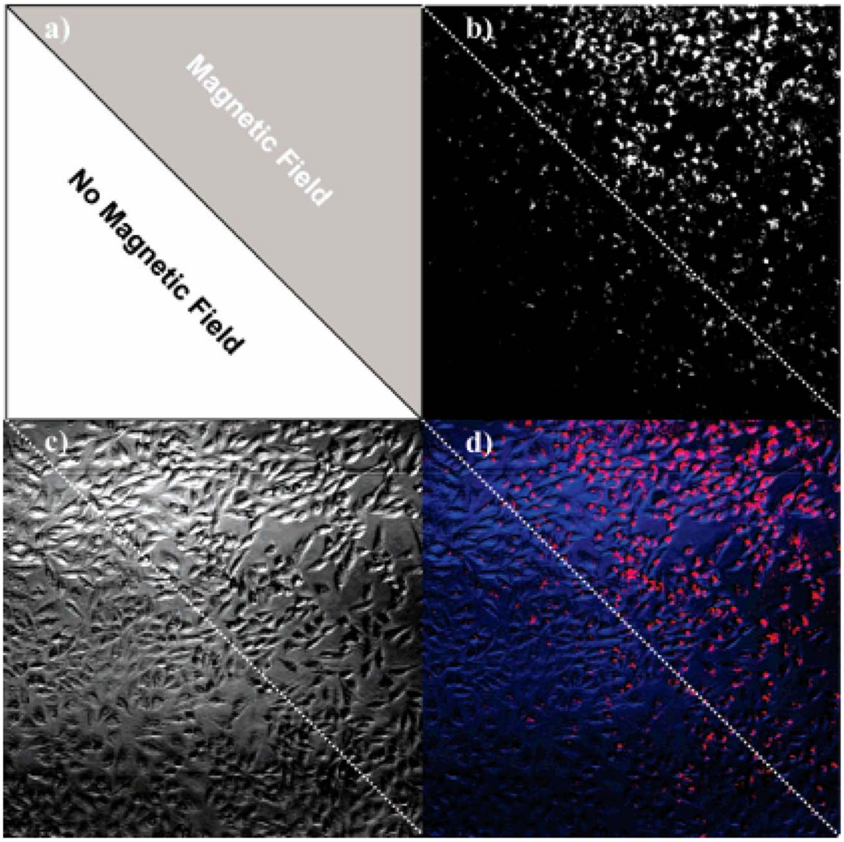

Fig. 53 Images of cells labeled with PEG-PE micelles that coentrap H_2 and magnetic nanoparticles using magnetically guided two-photon stimulated fluorescence microscopy. The sample's upper right triangle was subjected to a magnet. (a) A schematic representation of the region where a magnetic field is applied; (b) fluorescence from micelles tagged with H_2; (c) transmission; and (d) merged images for transmission and fluorescence. Reproduced from ref. 132 with permission from American Chemical Society, Copyright © 2007.

demonstrated that these nanocomposites enable highly sensitive MR and fluorescence imaging. Furthermore, Fe_3O_4/HBC@F127 effectively delivered anticancer drugs, inhibiting the proliferation of HepG2 cells. Exhibiting good biocompatibility, these nanocomposites show significant potential as multifunctional platforms for cancer diagnosis and targeted therapy delivery.[223]

Saadati *et al.* (2024) employed DFT calculations to evaluate the potential of HBC and its doped derivatives as carriers for the anticancer drug carmustine (BCNU), as illustrated in Fig. 56. Using the B3LYP functional with 6-31+G(d) and 6-311+G(d,p) basis sets, the study examined geometry optimization, vibrational frequencies, NBO analysis, and frontier molecular orbitals to assess drug–nanographene interactions. Strong binding was observed between BCNU and nanographenes including HBC, nitrogen-doped HBC (NHBC), and boron–nitrogen co-doped HBC (BNHBC), without significant structural distortions. HOMO–LUMO gap (E_g) analysis revealed slight decreases for HBC complexes (~6.2% and 4.6%), indicating maintained electronic stability. PDOS results showed HOMO contributions mainly from nanographene and LUMO influenced by both drug and carrier, with minimal charge transfer from NBO analysis. Nitrogen doping enhanced sensitivity, with NHBC exhibiting significant E_g reductions (~22.3% and 18.0%) and noticeable structural changes upon BCNU binding. BNHBC showed a stronger electronic response and higher adsorption energy (up to -19.1 kcal mol^{-1}), yet NHBC demonstrated the best balance of sensitivity and stability. Drug release times at 298 K further favored NHBC, with rapid release within 1.8–4.6 s compared to longer durations for HBC and BNHBC. These findings highlight NHBC's promise as an efficient and responsive nanocarrier for targeted drug delivery applications.[224]

4.5. Applications of HBCs in liquid crystal materials

Hirose *et al.* (2015) reported the design and synthesis of two distinct classes of discotic liquid crystalline (DLC) materials based on triphenylene (TP) and HBC as the central aromatic cores. To enhance solubility in conventional organic solvents, trialkylsilylethynyl substituents bearing one or two long alkyl chains were strategically introduced into the molecular framework. The thermal phase behavior and mesomorphic properties of these compounds were thoroughly characterized. The TP-based derivatives, denoted as TPSi (**183**), exhibited rectangular columnar (Col_r) mesophases, while compounds such as TPSi and the HBC-based series HBCSi(*m*) (with $m = 10$, 12, 14, and 16) displayed hexagonal columnar (Col_h) mesophases as show in Fig. 57. Interestingly, none of the TP derivatives

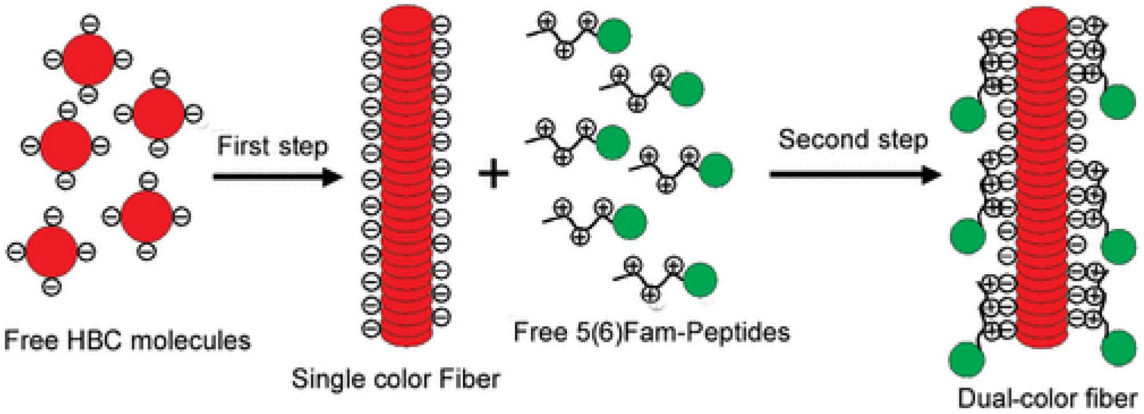

Fig. 54 Diagrammatic illustration of the two-step template approach. Reproduced from ref. 222 with permission from American Chemical Society, Copyright © 2009.

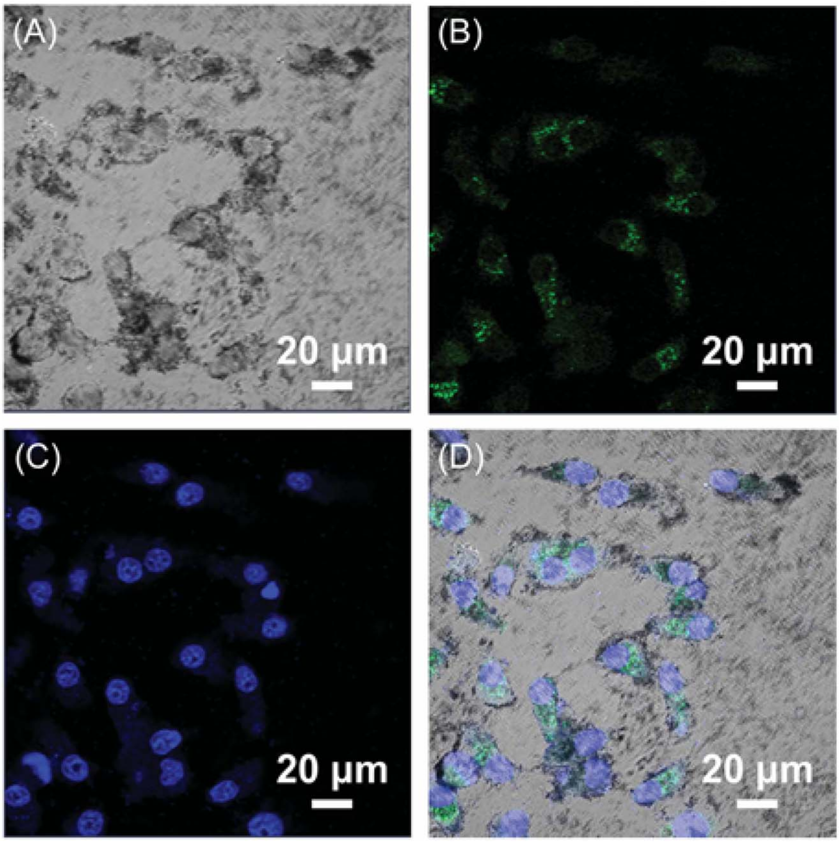

Fig. 55 HepG2 cells treated to 10 µg per mL Fe_3O_4/HBC@F127 nanocomposites for 24 hours were shown in CLSM pictures. Bright-field (A), Fe_3O_4/HBC@F127 nanocomposites (B), DAPI (C), and the combined image of (A)–(C) are shown in (D). Reproduced from ref. 223 with permission from the Royal Society of Chemistry.

demonstrated measurable charge mobility, likely due to disordered molecular stacking that hindered efficient π-electron transport. In contrast, the HBC derivative HBCSi (**184**) exhibited a hole mobility of approximately 1.5×10^{-3} cm^2 V^{-1} s^{-1} at 140 °C. Although this value is two orders of magnitude lower than the highest mobilities previously reported for HBC-based systems, the reduction is attributed to the presence of bulky side chains that may disrupt close π–π stacking despite the inherent self-organizing capability of the HBC core. This study highlights the crucial role of molecular design particularly side-chain architecture and core planarity in dictating the liquid crystalline behavior and charge transport efficiency of discotic systems. The findings also point to a trade-off between solubility and electronic performance, where bulky solubilizing groups may compromise charge transport by disrupting π-stacking. Future development of HBC liquid crystals should

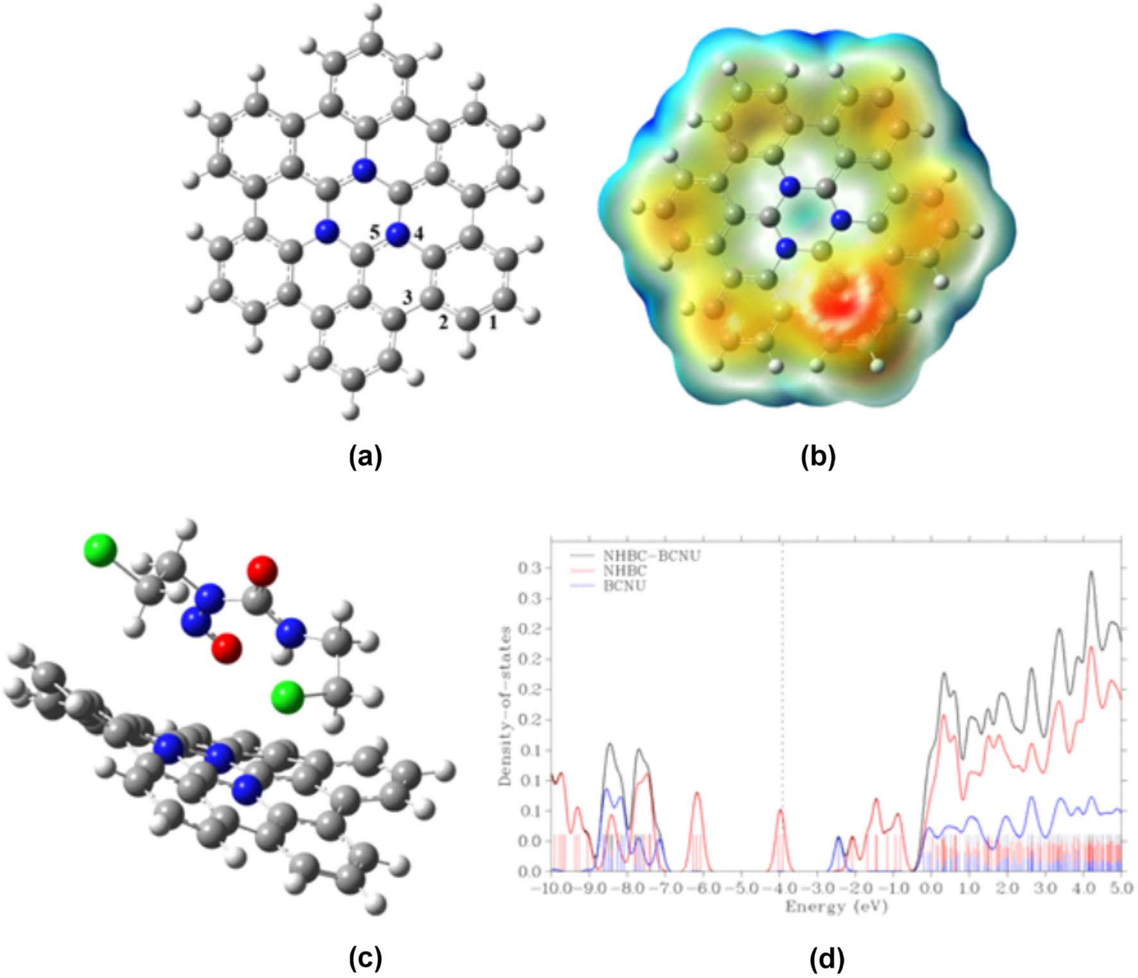

Fig. 56 (a) Optimized structure and (b) computed MEP plot of the NHBC (c) optimized structure (d) PDOS plot of the NHBC–BCNU complex. Reproduced from ref. 224 with permission from Elsevier, Copyright © 2024.

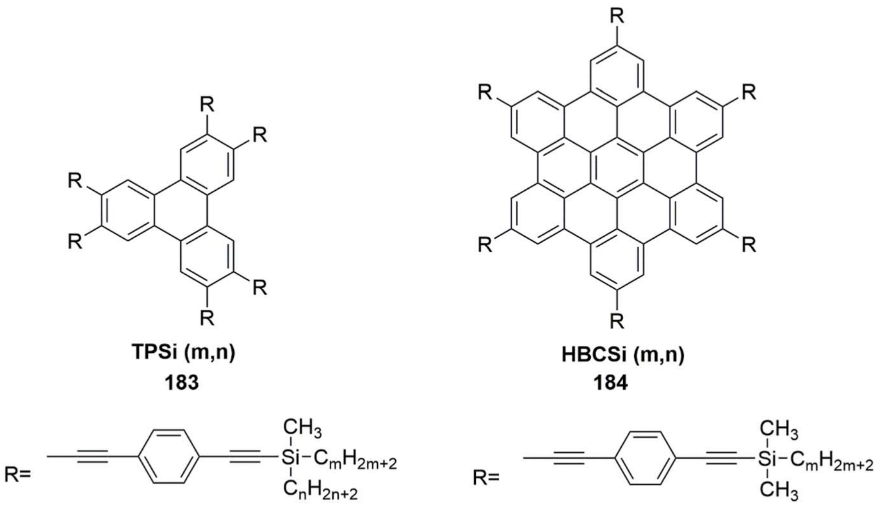

Fig. 57 Molecular structures of both series TPSi and HBCSi respectively.[225]

focus on optimizing side-chain length and flexibility to balance processability with functional performance, thus enabling their practical use in third-generation optoelectronic devices.[225]

Jones *et al.* (2019) explored a novel strategy for enhancing singlet fission (SF) in organic semiconductors by incorporating liquid crystalline behavior into an amorphous FHBC(TDPP)$_2$

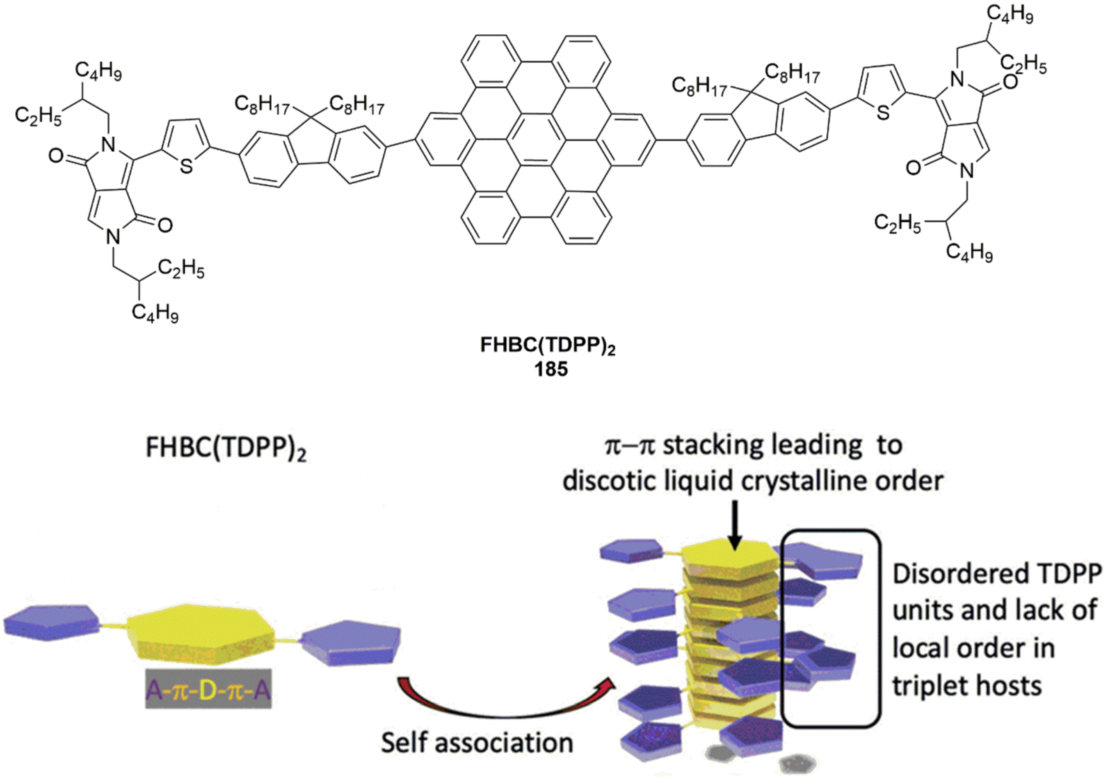

Fig. 58 The chemical structure of FHBC(TDPP)$_2$ (**185**) is characterized by an acceptor–π–donor–π–acceptor (A–π–D–π–A) configuration, where the central HBC moiety functions as the electron-donating core (D). Reproduced from ref. 226 with permission from John Wiley & Sons, Copyright © 2019, Wiley-VCH Verlag GmbH & Co. KGaA, Weinheim.

thin film as shown in Fig. 58. The molecule comprises a fluorene-functionalized hexa-*peri*-hexabenzocoronene (FHBC) core and two TDPP (thieno[3,2-*b*]pyrrolo[3,4-*c*]pyrrole-1,4-dione) units arranged in an acceptor–donor–acceptor (A–D–A) configuration. This molecular design promotes self-assembly *via* discotic liquid crystalline (LC) domains, aligning chromophores in proximity without inducing long-range crystallinity. GIWAXS analysis confirmed π–π stacking from the FHBC core, while the TDPP arms remained disordered. Thermal annealing significantly improved singlet fission dynamics, with a rate of 0.1–0.2 ps^{-1} and triplet yields reaching 150–170%. This work highlights a novel design paradigm for singlet fission materials, where liquid crystallinity is leveraged to induce short-range order without crystallinity, enabling effective chromophore proximity for Dexter-type triplet energy transfer. The architectural integration of a π-conjugated HBC discotic core with triplet-generating FHBC(TDPP)$_2$ (**185**) arms yields a system that supports SF despite lacking conventional crystalline packing. The high triplet yields, and rapid fission kinetics observed upon annealing demonstrate that self-organized domains can substitute for full crystallinity, offering more processable and versatile material systems. Importantly, the lack of SF activity in solution confirms the necessity of solid-state interactions. These findings open avenues for the application of HBC-based chromophores in third-generation photovoltaic technologies, where both efficiency and morphological tunability are critical. Further investigations into structure–property relationships, particularly the balance between core stacking and side-chain-induced disorder, are likely to yield impactful insights for the rational design of next-generation optoelectronic materials.[226]

Chen *et al.* (2020) described the development of a series of discotic mesogens based on D_{3h}-symmetric HBC frameworks functionalized with three diacetylene-substituted side chains and three saturated alkyl chains arranged in an alternating fashion. These compounds, denoted as HBC-1,3,5-C-DA-R, were synthesized *via* streamlined synthetic procedures and were found to exhibit thermotropic columnar liquid crystalline phases within the narrow temperature window of 26–33 °C as shown in Fig. 59. Among the series, compound **186c** displayed an unusual and highly desirable homeotropic alignment between glass slides, an uncommon characteristic in discotic liquid crystalline materials. This alignment facilitated a well-ordered mesophase at room temperature, enabling precise packing of the diacetylene (DA) side chains. Such organization is particularly beneficial for topochemical reactions, as it allows efficient polymerization or cross-linking within the columnar domains. Upon external stimulation, both UV irradiation and thermal treatment triggered polymerization through the diacetylenic functionalities localized around the HBC core. The thermally induced process yielded approximately 80% polymer conversion after 2 hours, while UV exposure under similar conditions achieved nearly complete polymerization, highlighting the system's high photo reactivity and process efficiency. Compound **186d** further demonstrated promising

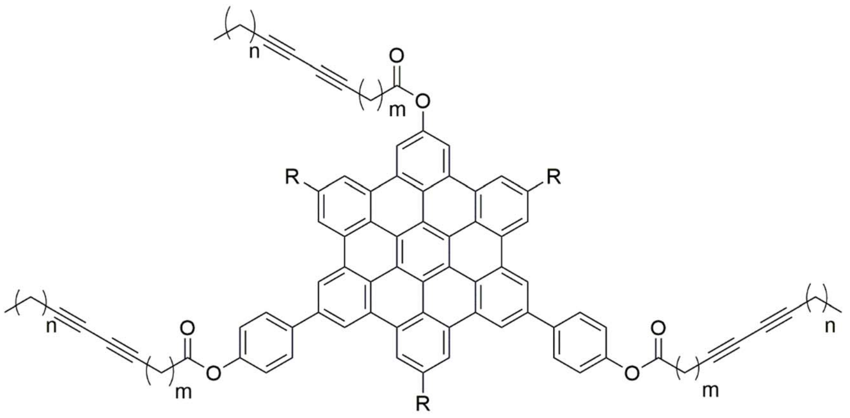

HBC-1,3,5-C$_{m,n}$-DA-R
186

R= $C_{12}H_{25}$ m = 2, n= 13 HBC-1,3,5-$C_{2,13}$-DA-C_{12} (186a)
m = 2, n= 7 HBC-1,3,5-$C_{3,7}$-DA-C_{12} (186b)
m = 8, n= 9 HBC-1,3,5-$C_{8,9}$-DA-C_{12} (186c)
R= C_4H_9 m = 8, n= 9 HBC-1,3,5-$C_{8,9}$-DA-C_4 (186d)

Fig. 59 Molecular structure of HBC derivatives with three diacetylene-containing and three alkyl side chains in alternating positions (HBC-1,3,5-C$_{m,n}$-DA R).[227]

electronic properties, exhibiting a field-effect mobility-sum product ($\phi\sum\mu_{\max}$) in the range of ~1.0×10^{-4} cm^2 V^{-1} s^{-1}. This performance is comparable to that of D_{6h}-symmetric HBC analogues, suggesting that symmetry reduction to D_{3h} does not detrimentally impact charge transport. Instead, it offers alternative molecular design strategies for enhancing alignment and functional performance. This work underscores the role of side-chain engineering and symmetry control in fine-tuning the structural and functional properties of HBC-based mesogens. The D_{3h} symmetry facilitates columnar assembly with defined alignment characteristics, which is critical for ensuring directional charge transport in organic electronic devices. Importantly, the observed field-effect mobility supports the viability of these materials in practical optoelectronic applications. Future investigations into substrate alignment, molecular orientation, and side-chain dynamics could yield deeper insights into achieving long-range molecular order and improved electronic performance in HBC-derived liquid crystals.[227]

Chen *et al.* (2023) investigated a series of discotic mesogens derived from D_{3h}-symmetric HBC cores, denoted as HBC-1,3,5-C$_{m,n}$-DA-C$_{6,8}$ **187**, synthesized by functionalizing the periphery with three diacetylene (DA)-containing alkyl chains and three branched aliphatic chains arranged alternately as shown in Fig. 60. These mesogens displayed columnar liquid crystalline phases over a temperature range of −2 °C to 17 °C, depending on the position of the DA moiety along the side chain. This photochemical behavior yielded two distinct outcomes based on the structural positioning of the DA unit. For compound **187a**, where the diacetylene group is located closer to the aromatic HBC core, UV exposure for 2 hours resulted in efficient one-dimensional polymerization along the columns, producing poly(eneyne) chains with a conversion yield of approximately 53% as shown in Fig. 60. In contrast, compound **187b**, with the DA unit positioned further from the HBC core, exhibited limited photopolymerization, predominantly undergoing intermolecular crosslinking between columns and yielding a lower product efficiency of around 23%. These results indicate that the spatial positioning of the DA moiety significantly influences the photo reactivity, alignment, and packing behavior of the mesogens. In particular, the proximity of the reactive unit to the rigid HBC core promotes linear polymer growth, while increased chain flexibility and distance lead to crosslinked networks with diminished conversion rates. Furthermore, the presence of branched alkyl chains impacts the steric environment and molecular self-assembly, thereby modulating both mesophase stability and polymerization pathways. The resulting polymerized columnar structures hold significant potential for application in optoelectronic devices, particularly where thermal stability and anisotropic charge transport are essential. Additionally, tuning the side chain composition and optimizing irradiation conditions could lead to improved conversion efficiencies and mechanical robustness. The incorporation of such HBC-based LC polymers in nanowire templating, light-harvesting arrays, and flexible electronics represents a promising direction for next-generation organic electronic materials.[228]

Chen *et al.* (2024) demonstrated the effective application of the bar-coating technique to fabricate aligned thin films of the liquid crystalline small molecule HBC-1,3,5-PhC$_{12}$ (**188**) on quartz substrates as shown in Fig. 61. This method facilitated the formation of well-organized columnar mesophases. At a slower coating velocity of 250 μm s^{-1}, the material exhibited a striped surface morphology, characterized by columnar stacks oriented perpendicularly to the coating direction. In contrast, increasing the coating speed to 350 μm s^{-1} yielded a continuous fibrous texture, with the columnar aggregates aligning parallel to the direction of bar movement. These anisotropic morphological features were thoroughly characterized by different spectroscopic techniques. The observed orientation behavior

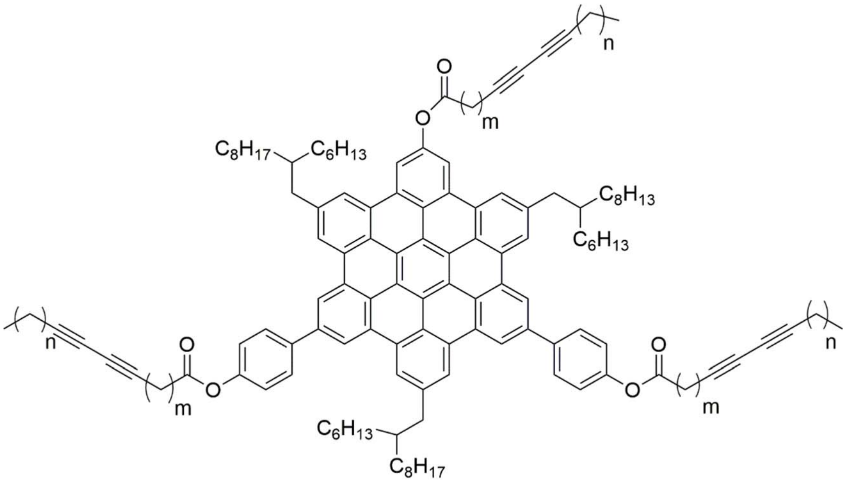

187

HBC-1,3,5-$C_{2,13}$-DA-$C_{6,8}$ (187a)
HBC-1,3,5-$C_{8,9}$-DA-$C_{6,8}$ (187b)

Fig. 60 Structural representation of HBC-1,3,5-$C_{m,n}$-DA-$C_{6,8}$.[228]

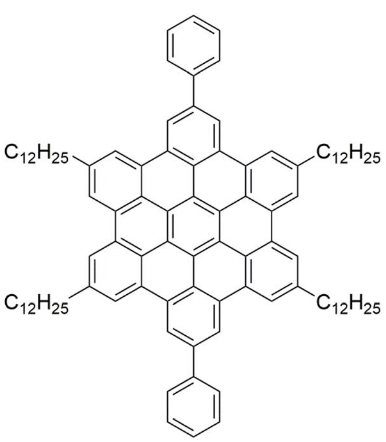

188

Fig. 61 Molecular structure of HBC-1,3,5-Ph-C_{12}.[229]

was attributed to a complex interplay between surface energy minimization and shear-induced alignment during the coating process. While such alignment phenomena have been previously reported in the context of conjugated polymers, this study marks the first successful observation of flow-induced alignment in small organic molecules bearing HBC core. This work presents a significant advancement in the controlled alignment of discotic liquid crystals, particularly in the context of small organic π-conjugated systems. By modulating the coating speed, the molecular orientation can be precisely tailored, which is crucial for optimizing anisotropic charge transport in organic electronic devices. Such fine-tuned alignment strategies are expected to enhance the performance of organic field-effect transistors (OFETs), organic photovoltaics (OPVs), and related optoelectronic systems. Future research may focus on substrate surface modifications, thermal annealing post-deposition, and incorporation of functional side chains to further refine alignment control and expand applicability across diverse device architectures.[229]

4.6. Applications of HBCs in solar cells

Zheng *et al.* (2015) pioneered the use of a functionalized nanographene material perthiolated trisulfur-annulated HBC (TSHBC) (**189**) as a hole transport layer (HTL) in perovskite solar cells (PVSCs), incorporating it in combination with graphene sheets as shown in Fig. 62a. This novel HTL design facilitated efficient charge extraction at the perovskite interface. A key advantage of TSHBC is the presence of peripheral thiol functionalities, which impart significant hydrophobicity. These thiol groups form a protective barrier on the perovskite surface, effectively hindering moisture ingress and thereby enhancing the operational stability of the solar cells. Device stability was evaluated under AM 1.5 G solar illumination at approximately 45% relative humidity in the absence of encapsulation as shown in Fig. 62e. The perovskite solar cells featuring the TSHBC/graphene composite HTL retained over 90% of their initial power conversion efficiency after 10 days of exposure. In stark contrast, devices employing the conventional spiro-OMeTAD HTL preserved only 20% of their original efficiency under identical conditions as shown in Fig. 62c. This substantial difference clearly demonstrates the improved environmental resilience imparted by the TSHBC-based HTL. The improved stability can be attributed to both electronic and interfacial effects. The π-conjugated HBC core in TSHBC promotes efficient hole mobility, while the thiolated periphery provides a chemically robust, hydrophobic interface that passivates trap states and mitigates moisture-induced degradation. The synergistic interaction between TSHBC and graphene further enhances the conductive network and ensures intimate contact with the perovskite layer, reducing charge recombination. This study underscores the significance of

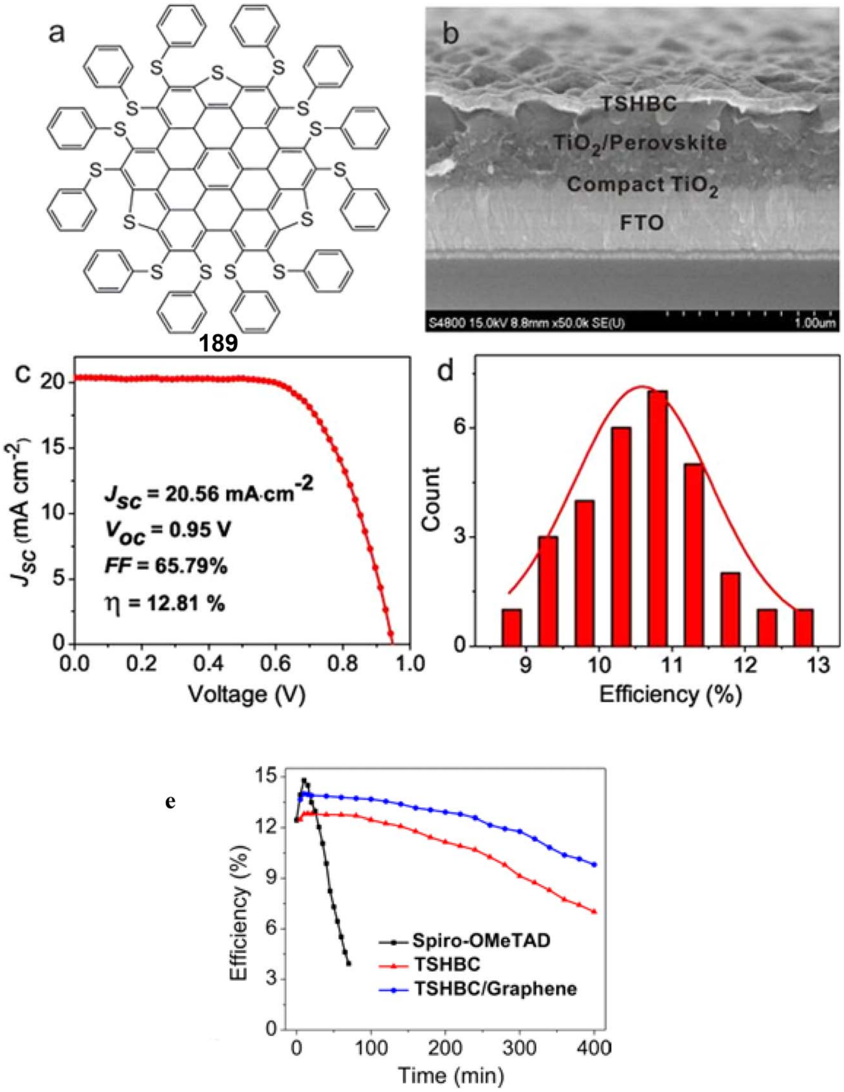

Fig. 62 (a) The molecular representation of TSHBC. (b) SEM image of the device of FTO/TiO_2/perovskite/TSHBC film. The best I–V characteristics (c) comparison of the performance distributions of 30 individual devices (d) of the cells. (e) The efficiency variation of the devices stored under illumination at AM 1.5 G with the humidity of 45%. Reproduced from ref. 230 with permission from American Chemical Society, Copyright © 2015.

tailored molecular design in achieving both high performance and durability in next-generation optoelectronic devices.[230]

Brabec *et al.* (2023) reported the synthesis and evaluation of four novel hole-transport materials (HTMs) based on a dumbbell-shaped architecture incorporating a central boron dipyrromethene (BODIPY) core, flanked by PAHs—either pyrene or HBC—and terminal 4,4-dimethoxytriphenylamine groups. Synthesized in yields ranging from 32–45%, these materials were comprehensively characterized through optical, electrochemical, and theoretical methods. Enhanced π-conjugation within the series led to broadened absorption, red-shifted transitions, increased charge delocalization, improved hole mobilities, and longer fluorescence lifetimes. Among them, TM-02 displayed the most promising features, including a high photoluminescence quantum yield ($\Phi = 0.29$), narrow optical/electrical band gaps (1.80/1.45 eV), excellent thermal stability ($T_d = 458$ °C), and notable hole mobility (4.32×10^{-4} cm^2 V^{-1} s^{-1}). When applied in p–i–n planar perovskite solar cells, TM-02 achieved a PCE of 20.26%, outperforming the benchmark HTM PTAA (19.30%), and retained 93% of its initial efficiency after 600 hours as shown in Fig. 63. These results underscore the potential of BODIPY–PAH-based HTMs for high-efficiency, thermally stable perovskite photovoltaics.[231]

Park *et al.* (2023) developed molecularly engineered hole-transport materials (HTMs) and interface modifiers aimed at enhancing the thermal stability of perovskite solar cells (PSCs). Two novel HTMs, named HBC-DPAMeOMe and HBC-DPAOMe, were synthesized using a nanographene (NG)-based HBC core. Both materials exhibited excellent hole mobility and high thermal decomposition temperatures ($T_d > 130$ °C), even in the presence of conventional dopant additives. Remarkably, the incorporation of HBC-DPAMeOMe in combination with PyMAI,

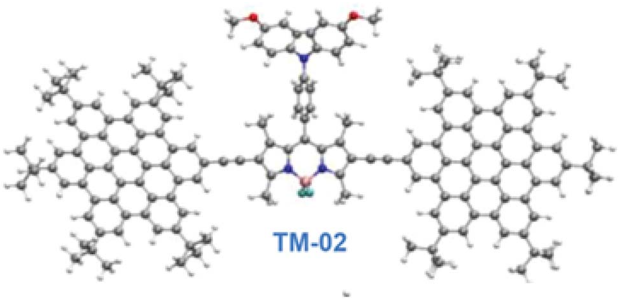

Fig. 63 DFT structure of TM-02 efficient for perovskite solar cells along with its inverted planar configuration. Reproduced from ref. 231 with permission from John Wiley & Sons, Copyright © 2023, Wiley-VCH Verlag GmbH & Co. KGaA, Weinheim.

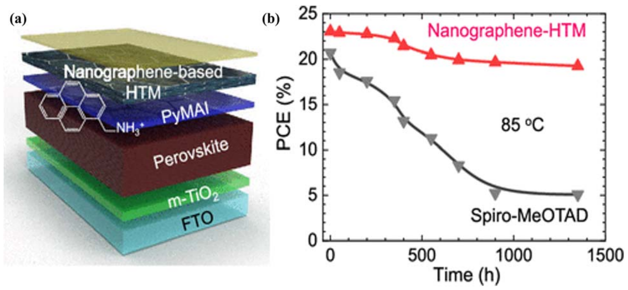

Fig. 64 (a) The FTO/m-TiO$_2$/perovskite/HTM/Au device structure is shown schematically, with PyMAI acting as an interface modifier between the perovskite and HBC-DPA(Me)OMe (b) PCE using the ISOS-D-2I protocol as a function of aging time at 85 °C. Reproduced from ref. 232 with permission from American Chemical Society, Copyright © 2023.

a pyrene-derived interface material, resulted in PSCs achieving a PCE exceeding 23%. Furthermore, devices employing HBC-DPAMeOMe maintained approximately 84% of their initial PCE after 1000 hours of continuous thermal stress at 85 °C. This performance was significantly superior to that of devices using the conventional spiro-MeOTAD HTM, which exhibited a substantial efficiency drop from 20.69% to 5.08% under the same conditions, as shown in Fig. 64. These findings underscore the potential of NG-based HTMs in the development of thermally robust PSCs suitable for long-term commercial deployment.[232]

Chen *et al.* (2025) reported the development of two non-planar, propeller-shaped carbazole-fused HAB-based compounds—K5-36 and its cyclized analog K5-13—as efficient hole-selective layers (HSLs) for perovskite solar cells (PSCs) (Fig. 65). Synthesized *via* a metal-free, green protocol with high yields (60–85%) and low production costs ($18–27 per g), these materials were integrated into p–i–n devices with the configuration ITO/4PADCB/K5-HSL/$Cs_{0.18}FA_{0.82}Pb(I_{0.8}Br_{0.2})_3$/PDADI/$PC_{61}BM$/BCP/Ag. Incorporation of K5-36 significantly enhanced device performance by promoting larger perovskite crystal growth and reducing charge recombination. Under AM 1.5 G illumination, the K5-36-based PSC achieved a power conversion efficiency (PCE) of 20.06%. Notably, under low-light conditions, the same device exhibited a J_{SC} of 283.05 μA cm^{-2}, V_{OC} of 1.07 V, and fill factor of 82.66%, resulting in an exceptional PCE of 42.02%. This marks the first instance of an HAB-based HSL enabling such high performance, demonstrating strong potential for advanced PSC applications.[233]

5. Overview of synthesis methods and applications of HBC

HBC is a promising molecule due to its well-defined, highly conjugated π-system and its significant potential in a variety of cutting-edge applications. The synthesis of HBC and its derivatives can be accomplished through several well-established methodologies, each providing distinct advantages and limitations. Table 1 summarizes the most widely used synthesis methods for HBC, including the Scholl reaction, annulative π-extension (APEX), dehydrative π-extension (DPEX), surface-assisted cyclodehydrogenation, Pd-catalyzed annulation, bottom-up synthesis *via* solution methods, and self-assembly from substituted HBCs. Each of these approaches enables precise control of molecular architecture, which is crucial for tailoring the material properties for specific applications.

In addition to the synthetic methods, the applications of HBC have been explored across various fields, including organic electronics, energy storage, catalysis, and biomedicine. Table 2 outlines the key application areas of HBC, such as organic field-effect transistors (OFETs), organic light-emitting diodes

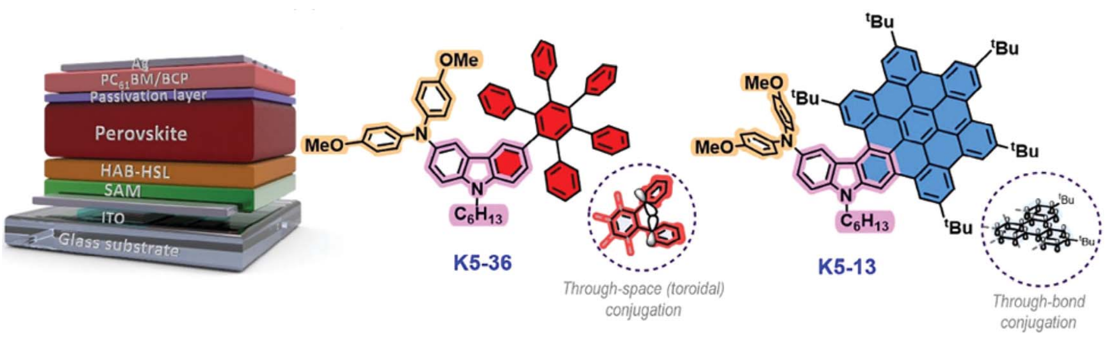

Fig. 65 Polyarene-based HBC perovskite solar cells. Reproduced from ref. 233 with permission from John Wiley & Sons, Copyright © 2025, Wiley-VCH Verlag GmbH & Co. KGaA, Weinheim.

Table 1 Overview of synthesis methods of HBC

Synthesis method	Description	Key advantages	Representative applications
Scholl reaction	Oxidative cyclodehydrogenation of preformed oligophenylenes	Simple protocol; widely used	Organic electronics, OLEDs, photovoltaic devices
Annulative π-extension (APEX)	Direct annulation to extend π-conjugation using halogenated aromatics	Regioselectivity; formation of large PAHs	Organic field-effect transistors (OFETs), energy storage
Dehydrative π-extension (DPEX)	Cyclization of aryl aldehydes to form extended π-systems	High atom economy, mild conditions	Catalysis, porous materials (COFs)
Surface-assisted cyclodehydrogenation	On-surface synthesis using metal surfaces under UHV conditions	High structural precision, avoids solubility issues	Nanoribbons, quantum materials
Pd-catalyzed annulation	Transition-metal-catalyzed C–C bond formation	High efficiency, useful for functionalized HBCs	Bioimaging, chemical sensors
Bottom-up synthesis *via* solution methods	Modular synthesis from small aromatic units	Atomic precision, tunable properties	Drug delivery, molecular electronics
Self-assembly from substituted HBCs	Formation of nanostructures *via* non-covalent interactions	Enables supramolecular architectures	Columnar liquid crystals, nanotubes, supercapacitors

Table 2 Applications of HBC in various technological fields

Field	Application areas	Key properties utilized
Organic and optoelectronics	- Organic field-effect transistors (OFETs) – organic light-emitting diodes (OLEDs) – organic photovoltaic devices (OPVs)	- Extended π-conjugation – high charge carrier mobility – strong absorption in UV-vis region
Energy storage	- Lithium-ion batteries – supercapacitors	- Excellent thermal/chemical stability – high electrical conductivity – π-stacking for electrode design
Catalysis	- Photocatalysis – metal nanoparticle support	- Redox-active surfaces – large surface area – tunable electronic environment
Biomedicine	- Drug delivery systems – fluorescence imaging	- Biocompatibility – strong fluorescence – functionalizable periphery

(OLEDs), photocatalysis, metal nanoparticle supports, and drug delivery systems. HBC's unique properties, including its high charge mobility, electrical conductivity, fluorescence, and biocompatibility, make it an ideal candidate for advancing technologies in these diverse fields. The continued development of HBC-based materials holds the promise of enhanced performance and innovations in energy storage, optoelectronics, catalysis, and biomedical applications.

6. Structure–property relationship

The unique physicochemical behavior of HBC stems from its planar π-extended framework, defined by its rigid, symmetric hexagonal core. HBC has significant UV-visible absorbance, low HOMO–LUMO energy gaps, and great thermal and oxidative stability due to the substantial delocalization of π-electrons over the conjugated aromatic surface. These electronic features make HBC and its derivatives ideal candidates for various optoelectronic applications. The structural modifiability at the periphery of the HBC core plays a pivotal role in determining intermolecular interactions, solubility, and self-assembly behavior. Substitution with long alkyl or branched side chains, for instance, improves solubility and facilitates liquid crystalline or supramolecular columnar stacking. These ordered assemblies enhance charge carrier mobility and exciton diffusion, making them suitable for organic field-effect transistors (OFETs) and photovoltaic applications.

HBC is a planar polycyclic aromatic hydrocarbon composed entirely of carbon atoms arranged in a rigid, conjugated π-system. The highly symmetric and extended aromatic core leads to strong π–π interactions between neighboring molecules, facilitating efficient charge transport and molecular ordering in the solid state. However, this same structural rigidity and absence of functional groups render pristine HBC poorly soluble in common organic solvents, limiting its processability for practical applications.

Doping the HBC framework with heteroatoms such as nitrogen or sulfur introduces significant changes in its electronic structure and physical properties. Nitrogen-doped HBCs (*e.g.*, aza-HBCs) often exhibit enhanced electron-accepting characteristics due to the electron-withdrawing nature of nitrogen, which lowers the LUMO energy levels and improves n-type semiconducting behavior. Additionally, nitrogen incorporation can disrupt the planarity and reduce the aromatic stabilization, affecting stacking behavior and photophysical properties.

Similarly, sulfur-doped HBCs introduce heteroatoms into the conjugated framework that can improve charge carrier mobility by altering the electronic distribution and increasing polarizability. Sulfur atoms, when inserted into the HBC scaffold (*e.g.*, thia-HBCs), may lead to enhanced hole transport and modulate the HOMO–LUMO energy gap, often resulting in red-shifted absorption and improved performance in optoelectronic devices.

In aza-HBC derivatives, one or more carbon atoms in the HBC core are replaced by nitrogen atoms. This substitution reduces the overall aromatic stabilization due to the lower electron-donating capacity of nitrogen, leading to changes in optical properties such as bathochromic shifts in UV-Vis absorption and altered fluorescence behavior. The incorporation of nitrogen also introduces asymmetry in the molecular framework, which may enhance dipole moments and improve solubility in polar solvents. Moreover, aza-HBCs are promising candidates for electron-transporting layers due to their modified electronic configuration and lower LUMO levels compared to the parent HBC.

The pristine HBC molecule, due to its extended conjugation and lack of substituents, exhibits strong intermolecular π–π interactions and tight molecular packing in the solid state, which severely limits its solubility. However, functionalization at the periphery of the HBC core with flexible or bulky groups significantly enhances solubility by disrupting planarity and reducing aggregation tendencies. For instance, the introduction of alkyl chains (*e.g.*, *n*-dodecyl, *n*-hexyl, or *tert*-butyl), oligoethylene glycol units, or aryl substituents at the peripheral positions leads to increased solubility in a variety of organic solvents. These substitutions not only improve processability but also allow for fine-tuning of the material's liquid crystalline behavior, thermal stability, and self-assembly into columnar mesophases.

Electronic and photophysical properties such as absorption maxima, fluorescence quantum yields, and redox potentials can be precisely tuned by introducing electron-donating or electron-withdrawing groups at strategic positions. Additionally, π-extension strategies, such as the incorporation of HBC into larger nanographene or polymeric systems, further modulate optical and electronic characteristics, extending their utility in organic electronics, energy storage systems, catalysis, and biosensing platforms.

In summary, the structural modification of HBC through heteroatom doping or peripheral substitution offers a versatile strategy to tailor its physical, chemical, and electronic properties. While undoped HBCs benefit from strong intermolecular interactions and high charge transport due to their planar π-system, nitrogen and sulfur doping introduces electronic modulation, and peripheral groups enhance solubility and processability—making these derivatives more suitable for applications in organic electronics, photovoltaics, and sensing.

7. Future directions and challenges

Despite considerable advances in the synthesis of HBC derivatives through approaches such as Scholl reactions and annulative π-extension, several synthetic challenges persist. These include issues related to low regioselectivity, poor solubility of key intermediates, and limited scalability of reaction protocols. Such limitations hinder large-scale production and practical integration of HBC-based materials. Consequently, the development of more efficient, selective, and environmentally benign synthetic strategies remains an essential area of research to facilitate the broader application of HBC derivatives in advanced technologies.

The performance of HBC-based systems in optoelectronic and energy-related devices is highly dependent on their precise supramolecular organization. Controlling the self-assembly and long-range order of HBC molecules through peripheral functionalization is vital for achieving optimal charge transport, exciton diffusion, and photophysical behavior. However, designing substituents that promote hierarchical organization without compromising electronic properties or processability remains a significant scientific challenge. Further exploration of structure–property relationships in these systems is necessary to enable targeted molecular design for enhanced device performance.

For the integration of HBCs into real-world devices—such as organic light-emitting diodes (OLEDs), sensors, and supercapacitors—a robust understanding of material–device interfaces are imperative. Key challenges include enhancing material stability under operational stress, optimizing interfacial interactions, and developing scalable and cost-effective fabrication techniques. Addressing these aspects will be critical for translating HBC-based materials from laboratory-scale demonstrations to commercially viable technologies.

An emerging strategy to enhance the versatility and performance of HBCs involves the creation of multifunctional hybrid materials. Combining HBCs with other components such as metal nanoparticles, graphene-based materials, or conductive polymers offers a pathway to engineer synergistic properties. These hybrid systems may unlock new functionalities, including catalytic activity, mechanical flexibility, and electronic tunability. Exploration in this direction holds significant potential for advancing flexible electronics, energy storage, catalysis, and multifunctional nanodevices.

Ongoing developments in HBC-based nanographenes (NGs), particularly those exhibiting open-shell (radicaloid) character, present promising avenues for spintronics and molecular magnetic materials. Their intrinsic unpaired electrons offer potential for next-generation applications in chiral spintronics, molecular magnets, and nonlinear optical systems. However, the instability of radicaloid HBC derivatives under ambient conditions remains a critical limitation. Strategies such as spin delocalization over extended π-systems, introduction of sterically bulky substituents, and incorporation of electron-deficient heteroatoms can enhance the stability of these systems while retaining their open-shell electronic nature.

In the realm of biomedical applications, the utility of HBC-based materials remains underexplored due to challenges such as poor solubility in aqueous media, limited biocompatibility, and insufficient functionalization for biological targeting. These barriers can potentially be overcome through the design of water-dispersible HBC derivatives, implementation of targeted bioconjugation strategies, and comprehensive *in vitro* and *in vivo* toxicity evaluations. Nevertheless, their practical use is constrained by a lack of comprehensive studies on biocompatibility, cellular internalization mechanisms, and long-term toxicity. Systematic investigations into these biological parameters are crucial for ensuring the safe and effective deployment of HBC-based nanomaterials in medical and diagnostic settings. Such advancements could enable the integration of HBC-based nanostructures into biosensing, drug delivery, and fluorescence imaging platforms.

Another pressing concern lies in the limited translation of HBC-based materials into real-world technologies, which is primarily attributed to fabrication challenges, high production costs, and insufficient device-level performance data. Addressing these issues necessitates the development of scalable processing methods, including inkjet printing, roll-to-roll deposition, and interface optimization with diverse substrates. Integration with flexible and hybrid platforms will also be essential for enabling widespread adoption.

The convergence of HBC research with emerging tools such as artificial intelligence (AI) and machine learning (ML) is poised to accelerate innovation. These technologies can facilitate the prediction of structure–property relationships, optimize synthetic pathways, and guide molecular design with higher efficiency. Furthermore, the establishment of open-access databases containing experimental and computational data on HBC-based compounds could foster collaborative, data-driven research across disciplines.

Cross-disciplinary integration between synthetic organic chemistry, materials science, device engineering, and computational modeling is essential for harnessing the full potential of HBCs. Hybrid materials that combine HBC frameworks with polymers, inorganic components, or quantum dots may give rise to multifunctional systems with synergistic properties. Additionally, focused research on enantioselective synthesis, chiral control, and stabilization of radicaloid frameworks will pave the way for the application of HBCs in advanced optoelectronic, spintronic, and photonic devices.

8. Conclusions

HBC stands at the forefront of molecular nanographenes due to its structurally defined, highly conjugated, and stable aromatic framework. Through strategic structural modifications, its optical, electronic, and assembly properties can be finely tuned to meet the demands of diverse technological applications. This review highlights the critical advances in synthetic methodologies, structure–property correlations, and emerging roles of HBC-based materials in optoelectronics, energy storage, catalysis, sensing, and biomedicine. As the field progresses, overcoming synthetic challenges, achieving hierarchical control of molecular organization, and expanding application domains—especially in biological systems—will be crucial. Interdisciplinary approaches that integrate organic synthesis, materials science, and nanotechnology will play a central role in shaping the next generation of HBC-based functional materials with real-world impact.

Looking forward, several exciting avenues are expected to shape the next generation of HBC-based research. One prominent direction is the integration of HBC derivatives into hybrid electronic and optoelectronic devices in combination with two-dimensional materials such as graphene and molybdenum disulfide (MoS_2). These hybrid systems may enable synergistic interactions that enhance charge transport, light absorption, and overall device performance. Another significant opportunity lies in the development of covalent organic frameworks (COFs) constructed from HBC building blocks. These porous, crystalline materials can leverage the planarity and rigidity of HBC to yield highly ordered frameworks with tailored electronic properties, making them suitable for gas storage, catalysis, and energy-related applications. In the biomedical field, the biofunctionalization of HBC structures offers an innovative strategy for targeted drug delivery and cancer therapy. The ability to fine-tune the molecular architecture of HBC facilitates the incorporation of biocompatible moieties, allowing for selective interaction with biological targets. Given its adaptability and multifunctionality, HBC is poised to remain a key molecular scaffold in the ongoing exploration of advanced materials across both technological and therapeutic domains.

Author contributions

Ehsan Ullah Mughal: supervision, main idea, reviewing and editing, visualization, validation, final writing the manuscript. Nafeesa Naeem: first-draft preparation, data collection, reviewing and editing, visualization, validation. Syeda Fariha Kainat: first-draft preparation. Amina Sadiq: formal analysis. Hanan A. Oglay: formal analysis and funding acquisition.

Conflicts of interest

The authors have no conflict of interest to declare.

Data availability

No primary research results, software or code have been included and no new data were generated or analyzed as part of this review.

Acknowledgements

The authors extend their appreciation to the Deanship of Research and Graduate Studies at King Khalid University for funding this work through Large Research Project under grant number RGP2/95/46.

References

1 K. S. Novoselov, A. K. Geim, S. V. Morozov, D. Jiang, Y. Zhang, S. V. Dubonos, I. V. Grigorieva and A. A. Firsov, *Science*, 2004, **306**, 666–669.
2 K. S. Novoselov, D. Jiang, F. Schedin, T. J. Booth, V. V. Khotkevich, S. V. Morozov and A. K. Geim, *Proc. Natl. Acad. Sci. U. S. A.*, 2005, **102**, 10451–10453.
3 A. K. Geim and K. S. Novoselov, *Nat. Mater.*, 2007, **6**, 183–191.
4 K. S. Novoselov, V. I. Fal′ko, L. Colombo, P. R. Gellert, M. G. Schwab and K. Kim, *Nature*, 2012, **490**, 192–200.

5 W. Chen, P. Xiao, H. Chen, H. Zhang, Q. Zhang and Y. Chen, *Adv. Mater.*, 2019, **31**, 1802403.

6 C. Dai, G. Sun, L. Hu, Y. Xiao, Z. Zhang and L. Qu, *InfoMat*, 2020, **2**, 509–526.

7 Y. Zhang, X. Xia, B. Liu, S. Deng, D. Xie, Q. Liu, Y. Wang, J. Wu, X. Wang and J. Tu, *Adv. Energy Mater.*, 2019, **9**, 1803342.

8 H. Zhou, S. J. Han, A. K. Harit, D. H. Kim, D. Y. Kim, Y. S. Choi, H. Kwon, K.-N. Kim, G.-T. Go, H. J. Yun, B. H. Hong, M. C. Suh, S. Y. Ryu, H. Y. Woo and T.-W. Lee, *Adv. Mater.*, 2022, **34**, 2203040.

9 L.-P. Ma, Z. Wu, L. Yin, D. Zhang, S. Dong, Q. Zhang, M.-L. Chen, W. Ma, Z. Zhang, J. Du, D.-M. Sun, K. Liu, X. Duan, D. Ma, H.-M. Cheng and W. Ren, *Proc. Natl. Acad. Sci. U. S. A.*, 2020, **117**, 25991–25998.

10 I.-J. Park, T. I. Kim, T. Yoon, S. Kang, H. Cho, N. S. Cho, J.-I. Lee, T.-S. Kim and S.-Y. Choi, *Adv. Funct. Mater.*, 2018, **28**, 1704435.

11 N. Li, S. Oida, G. S. Tulevski, S.-J. Han, J. B. Hannon, D. K. Sadana and T.-C. Chen, *Nat. Commun.*, 2013, **4**, 2294.

12 M. Coroș, S. Pruneanu and R.-I. Stefan-van Staden, *J. Electrochem. Soc.*, 2019, **167**, 037528.

13 W. Tian, X. Liu and W. Yu, *Appl. Sci.*, 2018, **8**, 1118.

14 S. Das, D. Pandey, J. Thomas and T. Roy, *Adv. Mater.*, 2019, **31**, 1802722.

15 S. K. Behura, C. Wang, Y. Wen and V. Berry, *Nat. Photonics*, 2019, **13**, 312–318.

16 H. Su, T. Wu, D. Cui, X. Lin, X. Luo, Y. Wang and L. Han, *Small Methods*, 2020, **4**, 2000507.

17 X. Kong, L. Zhang, B. Liu, H. Gao, Y. Zhang, H. Yan and X. Song, *RSC Adv.*, 2019, **9**, 863–877.

18 M. Yi and Z. Shen, *J. Mater. Chem. A*, 2015, **3**, 11700–11715.

19 M. Coroș, F. Pogăcean, L. Măgerușan, C. Socaci and S. Pruneanu, *Front. Mater. Sci.*, 2019, **13**, 23–32.

20 N. Kumar, R. Salehiyan, V. Chauke, O. J. Botlhoko, K. Setshedi, M. Scriba, M. Masukume and S. S. Ray, *FlatChem*, 2021, **27**, 100224.

21 Y. Gu, Z. Qiu and K. Müllen, *J. Am. Chem. Soc.*, 2022, **144**, 11499–11524.

22 A. Narita, X.-Y. Wang, X. Feng and K. Müllen, *Chem. Soc. Rev.*, 2015, **44**, 6616–6643.

23 A. Ambrosi, C. K. Chua, A. Bonanni and M. Pumera, *Chem. Rev.*, 2014, **114**, 7150–7188.

24 Z. Liu, S. Fu, X. Liu, A. Narita, P. Samorì, M. Bonn and H. I. Wang, *Adv. Sci.*, 2022, **9**, 2106055.

25 X. Zhang, S. Wang, X. Chen, Z. Cui, X. e. Li, Y. Zhou, H. Wang, R. Sun and Q. Wang, *ACS Appl. Mater. Interfaces*, 2024, **16**, 45473–45486.

26 D. Yang, Y. Lin, W. Meng, Z. Wang, H. Li, C. Li, Z. Zhang, Q. Zhang, J. You and J. Wang, *Adv. Mater.*, 2025, 2419204.

27 N. Martin and C. P. Nuckolls, *Molecular Nanographenes: Synthesis, Properties, and Applications*, John Wiley & Sons, 2025.

28 W. Tong, H. Li, D. Liu, Y. Wu, M. Xu and K. Wang, *Fusion Eng. Des.*, 2025, **211**, 114744.

29 L. Zhai, R. Shukla and R. Rathore, *Org. Lett.*, 2009, **11**, 3474–3477.

30 X. Tian, R. Xun, T. Chang and J. Yu, *Phys. Lett. A*, 2025, 130597.

31 M. Müller, V. S. Iyer, C. Kübel, V. Enkelmann and K. Müllen, *Angew Chem. Int. Ed. Engl.*, 1997, **36**, 1607–1610.

32 S. H. Wadumethrige and R. Rathore, *Org. Lett.*, 2008, **10**, 5139–5142.

33 K. Xu, X. Xiao, L. Wang, M. Lou, F. Wang, C. Li, H. Ren, X. Wang and K. Chang, *Adv. Sci.*, 2024, **11**, 2405262.

34 A. K. Steiner and K. Y. Amsharov, *Angew. Chem., Int. Ed.*, 2017, **56**, 14732–14736.

35 O. Papaianina, V. A. Akhmetov, A. A. Goryunkov, F. Hampel, F. W. Heinemann and K. Y. Amsharov, *Angew. Chem., Int. Ed.*, 2017, **56**, 4834–4838.

36 M. Daigle, A. Picard-Lafond, E. Soligo and J. F. Morin, *Angew. Chem.*, 2016, **128**, 2082–2087.

37 Y. Koga, T. Kaneda, Y. Saito, K. Murakami and K. Itami, *Science*, 2018, **359**, 435–439.

38 S. Seifert, K. Shoyama, D. Schmidt and F. Würthner, *Angew. Chem.*, 2016, **128**, 6500–6505.

39 W. Matsuoka, H. Ito and K. Itami, *Angew. Chem.*, 2017, **129**, 12392–12396.

40 Z. Wang, P. Gu, G. Liu, H. Yao, Y. Wu, Y. Li, G. Rakesh, J. Zhu, H. Fu and Q. Zhang, *Chem. Commun.*, 2017, **53**, 7772–7775.

41 Z. Zhang and Q. Zhang, *Mater. Chem. Front.*, 2020, **4**, 3419–3432.

42 J. Li and Q. Zhang, *Synlett*, 2013, **24**, 686–696.

43 P.-Y. Gu, Y. Zhao, J.-H. He, J. Zhang, C. Wang, Q.-F. Xu, J.-M. Lu, X. W. Sun and Q. Zhang, *J. Org. Chem.*, 2015, **80**, 3030–3035.

44 W. Chen, X. Li, G. Long, Y. Li, R. Ganguly, M. Zhang, N. Aratani, H. Yamada, M. Liu and Q. Zhang, *Angew. Chem.*, 2018, **130**, 13743–13747.

45 W. Chen, F. Yu, Q. Xu, G. Zhou and Q. Zhang, *Adv. Sci.*, 2020, **7**, 1903766.

46 Z. Zhang, Z. Wang, N. Aratani, X. Zhu and Q. Zhang, *CCS Chem.*, 2022, **4**, 3491–3496.

47 J. Li, S. Chen, Z. Wang and Q. Zhang, *Chem. Rec.*, 2016, **16**, 1518–1530.

48 P.-Y. Gu, Z. Wang, G. Liu, H. Yao, Z. Wang, Y. Li, J. Zhu, S. Li and Q. Zhang, *Chem. Mater.*, 2017, **29**, 4172–4175.

49 P.-Y. Gu, Z. Wang and Q. Zhang, *J. Mater. Chem. B*, 2016, **4**, 7060–7074.

50 K. Ozaki, K. Kawasumi, M. Shibata, H. Ito and K. Itami, *Nat. Commun.*, 2015, **6**, 6251.

51 H. Kitano, W. Matsuoka, H. Ito and K. Itami, *Chem. Sci.*, 2018, **9**, 7556–7561.

52 E. H. Fort and L. T. Scott, *Tetrahedron Lett.*, 2011, **52**, 2051–2053.

53 A. Konishi, Y. Hirao, K. Matsumoto, H. Kurata and T. Kubo, *Chem. Lett.*, 2013, **42**, 592–594.

54 B. Schuler, S. Collazos, L. Gross, G. Meyer, D. Pérez, E. Guitián and D. Peña, *Angew. Chem.*, 2014, **126**, 9150–9152.

55 J. Li, C. Jiao, K. W. Huang and J. Wu, *Chem.–Eur. J.*, 2011, **17**, 14672–14680.

56 E. Gonzalez-Rodriguez, M. A. Abdo, G. dos Passos Gomes, S. Ayad, F. D. White, N. P. Tsvetkov, K. Hanson and I. V. Alabugin, *J. Am. Chem. Soc.*, 2020, **142**, 8352–8366.

57 H. Ito, K. Ozaki and K. Itami, *Angew. Chem., Int. Ed.*, 2017, **56**, 11144–11164.

58 D. Lungerich, O. Papaianina, M. Feofanov, J. Liu, M. Devarajulu, S. I. Troyanov, S. Maier and K. Amsharov, *Nat. Commun.*, 2018, **9**, 4756.

59 H. Qi, X. Jing, Y. Hu, P. Wu, X. Zhang, Y. Li, H. Zhao, Q. Ma, X. Dong and C. Mahadevan, *Composites, Part B*, 2025, **288**, 111933.

60 J. W. Flesher and A. F. Lehner, *Toxicol. Mech. Methods*, 2016, **26**, 151–179.

61 J. E. Anthony, *Angew. Chem., Int. Ed.*, 2008, **47**, 452–483.

62 J. E. Anthony, *Chem. Rev.*, 2006, **106**, 5028–5048.

63 D. J. Gundlach, J. E. Royer, S. K. Park, S. Subramanian, O. D. Jurchescu, B. H. Hamadani, A. J. Moad, R. J. Kline, L. C. Teague and O. Kirillov, *Nat. Mater.*, 2008, **7**, 216–221.

64 S. K. Park, T. N. Jackson, J. E. Anthony and D. A. Mourey, *Appl. Phys. Lett.*, 2007, **91**, 1–9.

65 S. Zhang, J. Li, Y. Tian, S. Fang, C. Li, X. Yu, Y. Jiang and L. Yang, *Combust. Flame*, 2025, **272**, 113858.

66 J. Wu, W. Pisula and K. Müllen, *Chem. Rev.*, 2007, **107**, 718–747.

67 H. Seyler, B. Purushothaman, D. J. Jones, A. B. Holmes and W. W. Wong, *Pure Appl. Chem.*, 2012, **84**, 1047–1067.

68 M. Randić, *Chem. Phys. Lett.*, 2014, **601**, 1–5.

69 M. Kastler, W. Pisula, D. Wasserfallen, T. Pakula and K. Müllen, *J. Am. Chem. Soc.*, 2005, **127**, 4286–4296.

70 A. M. van de Craats, J. M. Warman, K. Müllen, Y. Geerts and J. D. Brand, *Adv. Mater.*, 1998, **10**, 36–38.

71 P. Herwig, C. W. Kayser, K. Müllen and H. W. Spiess, *Adv. Mater.*, 1996, **8**, 510–513.

72 F. J. Hoeben, P. Jonkheijm, E. Meijer and A. P. Schenning, *Chem. Rev.*, 2005, **105**, 1491–1546.

73 W. Zhang, W. Jin, T. Fukushima, A. Saeki, S. Seki and T. Aida, *Science*, 2011, **334**, 340–343.

74 J. P. Hill, W. Jin, A. Kosaka, T. Fukushima, H. Ichihara, T. Shimomura, K. Ito, T. Hashizume, N. Ishii and T. Aida, *Science*, 2004, **304**, 1481–1483.

75 W. Jin, Y. Yamamoto, T. Fukushima, N. Ishii, J. Kim, K. Kato, M. Takata and T. Aida, *J. Am. Chem. Soc.*, 2008, **130**, 9434–9440.

76 T. Aida, E. Meijer and S. Stupp, *Science*, 2012, **335**, 813–817.

77 Y. Yamamoto, T. Fukushima, Y. Suna, N. Ishii, A. Saeki, S. Seki, S. Tagawa, M. Taniguchi, T. Kawai and T. Aida, *Science*, 2006, **314**, 1761–1764.

78 R. Rieger and K. Müllen, *J. Phys. Org. Chem.*, 2010, **23**, 315–325.

79 G. Rouillé, M. Steglich, F. Huisken, T. Henning and K. Müllen, *J. Chem. Phys.*, 2009, **131**, 204311–204323.

80 P. Haines, D. Reger, J. Träg, V. Strauss, D. Lungerich, D. Zahn, N. Jux and D. M. Guldi, *Nanoscale*, 2021, **13**, 801–809.

81 G. M. Beneventi, M. Krug, D. Reger, N. Jux and D. M. Guldi, *J. Photochem. Photobiol., C*, 2023, **56**, 100602.

82 V. Balzani, P. Ceroni and A. Juris, *Photochemistry and Photophysics: Concepts, Research, Applications*, John Wiley & Sons, 2014.

83 W. Hendel, Z. Khan and W. Schmidt, *Tetrahedron*, 1986, **42**, 1127–1134.

84 R. Rathore and C. L. Burns, *J. Org. Chem.*, 2003, **68**, 4071–4074.

85 A. Stabel, P. Herwig, K. Müllen and J. P. Rabe, *Angew Chem. Int. Ed. Engl.*, 1995, **34**, 1609–1611.

86 C. Kübel, K. Eckhardt, V. Enkelmann, G. Wegner and K. Müllen, *J. Mater. Chem.*, 2000, **10**, 879–886.

87 K. P. C. Vollhardt, *Angew. Chem.*, 1984, **96**, 525–541.

88 K. P. C. Vollhardt, *Acc. Chem. Res.*, 1977, **10**, 1–8.

89 J. A. Hyatt, *Org. Prep. Proced. Int.*, 1991, **23**, 460–463.

90 X. Feng, W. Pisula, L. Zhi, M. Takase and K. Müllen, *Angew. Chem., Int. Ed.*, 2008, **47**, 1703–1706.

91 X. Feng, W. Pisula, M. Takase, X. Dou, V. Enkelmann, M. Wagner, N. Ding and K. Müllen, *Chem. Mater.*, 2008, **20**, 2872–2874.

92 S. Ito, M. Wehmeier, J. D. Brand, C. Kübel, R. Epsch, J. P. Rabe and K. Müllen, *Chem.–Eur. J.*, 2000, **6**, 4327–4342.

93 A. Fechtenkötter, N. Tchebotareva, M. Watson and K. Müllen, *Tetrahedron*, 2001, **57**, 3769–3783.

94 X. Yang, X. Dou and K. Müllen, *Chem.–Asian J.*, 2008, **3**, 759–766.

95 J. Wu, M. Baumgarten, M. G. Debije, J. M. Warman and K. Müllen, *Angew. Chem., Int. Ed.*, 2004, **43**, 5331–5335.

96 X. Feng, J. Wu, V. Enkelmann and K. Müllen, *Org. Lett.*, 2006, **8**, 1145–1148.

97 R. Scholl and J. Mansfeld, *Ber. Dtsch. Chem. Ges.*, 1910, **43**, 1734–1746.

98 P. Kovacic and M. B. Jones, *Chem. Rev.*, 1987, **87**, 357–379.

99 P. Rempala, J. Kroulík and B. T. King, *J. Org. Chem.*, 2006, **71**, 5067–5081.

100 L. Zhai, R. Shukla and R. Rathore, *Org. Lett.*, 2009, **11**, 3474–3477.

101 M. Müller, C. Kübel and K. Müllen, *Chem.–Eur. J.*, 1998, **4**, 2099–2109.

102 Y. Kikuzawa, T. Mori and H. Takeuchi, *Org. Lett.*, 2007, **9**, 4817–4820.

103 W. W. H. Wong, D. J. Jones, C. Yan, S. E. Watkins, S. King, S. A. Haque, X. Wen, K. P. Ghiggino and A. B. Holmes, *Org. Lett.*, 2009, **11**, 975–978.

104 Z. Zeng, Z. Yin, X. Huang, H. Li, Q. He, G. Lu, F. Boey and H. Zhang, *Angew. Chem., Int. Ed.*, 2011, **50**, 11093–11097.

105 F. A. Murphy and S. M. Draper, *J. Org. Chem.*, 2010, **75**, 1862–1870.

106 X. Feng, W. Pisula, M. Ai, S. Gröper, J. P. Rabe and K. Müllen, *Chem. Mater.*, 2008, **20**, 1191–1193.

107 K. Weiss, G. Beernink, F. Dötz, A. Birkner, K. Müllen and C. H. Wöll, *Angew. Chem., Int. Ed.*, 1999, **38**, 3748–3752.

108 X. Dou, X. Yang, G. J. Bodwell, M. Wagner, V. Enkelmann and K. Müllen, *Org. Lett.*, 2007, **9**, 2485–2488.

109 M. Lee, J.-W. Kim, S. Peleshanko, K. Larson, Y.-S. Yoo, D. Vaknin, S. Markutsya and V. V. Tsukruk, *J. Am. Chem. Soc.*, 2002, **124**, 9121–9128.

110 J. P. Hill, W. Jin, A. Kosaka, T. Fukushima, H. Ichihara, T. Shimomura, K. Ito, T. Hashizume, N. Ishii and T. Aida, *Science*, 2004, **304**, 1481–1483.

111 Y. Lu and J. S. Moore, *Tetrahedron Lett.*, 2009, **50**, 4071–4077.

112 X. Feng, W. Pisula and K. Müllen, *Pure Appl. Chem.*, 2009, **81**, 2203–2224.

113 J. Wu, M. D. Watson, L. Zhang, Z. Wang and K. Müllen, *J. Am. Chem. Soc.*, 2004, **126**, 177–186.

114 S. K. Sadhukhan, C. Viala and A. Gourdon, *Synthesis*, 2003, 1521–1525.

115 P. T. Herwig, V. Enkelmann, O. Schmelz and K. Müllen, *Chem.–Eur. J.*, 2000, **6**, 1834–1839.

116 J. Wu, M. D. Watson, L. Zhang, Z. Wang and K. Müllen, *J. Am. Chem. Soc.*, 2004, **126**, 177–186.

117 L. Zhai, R. Shukla, S. H. Wadumethrige and R. Rathore, *J. Org. Chem.*, 2010, **75**, 4748–4760.

118 A. A. O. Sarhan and C. Bolm, *Chem. Soc. Rev.*, 2009, **38**, 2730–2744.

119 B. T. King, J. Kroulík, C. R. Robertson, P. Rempala, C. L. Hilton, J. D. Korinek and L. M. Gortari, *J. Org. Chem.*, 2007, **72**, 2279–2288.

120 P. Rempala, J. Kroulík and B. T. King, *J. Am. Chem. Soc.*, 2004, **126**, 15002–15003.

121 M. Di Stefano, F. Negri, P. Carbone and K. Müllen, *Chem. Phys.*, 2005, **314**, 85–99.

122 Y. He, Y. Yamamoto, W. Jin, T. Fukushima, A. Saeki, S. Seki, N. Ishii and T. Aida, *Adv. Mater.*, 2010, **7**, 829–832.

123 A. J. Berresheim, M. Müller and K. Müllen, *Chem. Rev.*, 1999, **99**, 1747–1786.

124 S. Sergeyev, W. Pisula and Y. H. Geerts, *Chem. Soc. Rev.*, 2007, **36**, 1902–1929.

125 X. Dou, W. Pisula, J. Wu, G. J. Bodwell and K. Müllen, *Chem.–Eur. J.*, 2008, **14**, 240–249.

126 C.-W. Chen, H.-Y. Chang, S.-L. Lee, I.-J. Hsu, J.-J. Lee, C.-h. Chen and T.-Y. Luh, *Macromolecules*, 2010, **43**, 8741–8746.

127 J. M. Mativetsky, M. Kastler, R. C. Savage, D. Gentilini, M. Palma, W. Pisula, K. Müllen and P. Samorì, *Adv. Funct. Mater.*, 2009, **19**, 2486–2494.

128 M. Ai, S. Groeper, W. Zhuang, X. Dou, X. Feng, K. Müllen and J. P. Rabe, *Appl. Phys. A*, 2008, **93**, 277–283.

129 M. Kastler, W. Pisula, R. J. Davies, T. Gorelik, U. Kolb and K. Müllen, *Small*, 2007, **3**, 1438–1444.

130 S. Entani, T. Kaji, S. Ikeda, T. Mori, Y. Kikuzawa, H. Takeuchi and K. Saiki, *J. Phys. Chem. C*, 2009, **113**, 6202–6207.

131 T. Mori, Y. Kikuzawa and H. Takeuchi, *Org. Electron.*, 2008, **9**, 328–332.

132 Q. Zheng, T. Y. Ohulchanskyy, Y. Sahoo and P. N. Prasad, *J. Phys. Chem. C*, 2007, **111**, 16846–16851.

133 Z. Zeng, Z. Guan, Q. H. Xu and J. Wu, *Chem.–Eur. J.*, 2011, **14**, 3837–3841.

134 J. Motoyanagi, T. Fukushima, A. Kosaka, N. Ishii and T. Aida, *J. Polym. Sci., Part A: Polym. Chem.*, 2006, **44**, 5120–5127.

135 T. Yamamoto, T. Fukushima, Y. Yamamoto, A. Kosaka, W. Jin, N. Ishii and T. Aida, *J. Am. Chem. Soc.*, 2006, **128**, 14337–14340.

136 J. L. Mynar, T. Yamamoto, A. Kosaka, T. Fukushima, N. Ishii and T. Aida, *J. Am. Chem. Soc.*, 2008, **130**, 1530–1531.

137 W. Zhang, W. Jin, T. Fukushima, N. Ishii and T. Aida, *Angew. Chem., Int. Ed.*, 2009, **48**, 4747–4750.

138 Y. Yamamoto, T. Fukushima, A. Saeki, S. Seki, S. Tagawa, N. Ishii and T. Aida, *J. Am. Chem. Soc.*, 2007, **129**, 9276–9277.

139 J. Motoyanagi, T. Fukushima, N. Ishii and T. Aida, *J. Am. Chem. Soc.*, 2006, **128**, 4220–4221.

140 Y. Yamamoto, G. Zhang, W. Jin, T. Fukushima, N. Ishii, A. Saeki, S. Seki, S. Tagawa, T. Minari and K. Tsukagoshi, *Proc. Natl. Acad. Sci. U. S. A.*, 2009, **106**, 21051–21056.

141 W. W. Wong, T. B. Singh, D. Vak, W. Pisula, C. Yan, X. Feng, E. L. Williams, K. L. Chan, Q. Mao and D. J. Jones, *Adv. Funct. Mater.*, 2010, **20**, 927–938.

142 W. W. Wong, C.-Q. Ma, W. Pisula, C. Yan, X. Feng, D. J. Jones, K. Müllen, R. A. Janssen, P. Bäuerle and A. B. Holmes, *Chem. Mater.*, 2010, **22**, 457–466.

143 W. W. Wong, C. Q. Ma, W. Pisula, A. Mavrinskiy, X. Feng, H. Seyler, D. J. Jones, K. Müllen, P. Bäuerle and A. B. Holmes, *Chem.–Eur. J.*, 2011, **17**, 5549–5560.

144 W. W. Wong, T. Khoury, D. Vak, C. Yan, D. J. Jones, M. J. Crossley and A. B. Holmes, *J. Mater. Chem.*, 2010, **20**, 7005–7014.

145 W. W. Wong, D. Vak, T. B. Singh, S. Ren, C. Yan, D. J. Jones, I. I. Liaw, R. N. Lamb and A. B. Holmes, *Org. Lett.*, 2010, **12**, 5000–5003.

146 P.-C. Zhu, Y. Liu, L.-H. Peng and C. Zhang, *Tetrahedron Lett.*, 2014, **55**, 521–524.

147 J. M. Englert, J. Malig, V. A. Zamolo, A. Hirsch and N. Jux, *Chem. Commun.*, 2013, **49**, 4827–4829.

148 Q. Zhang, H. Peng, G. Zhang, Q. Lu, J. Chang, Y. Dong, X. Shi and J. Wei, *J. Am. Chem. Soc.*, 2014, **136**, 5057–5064.

149 M. Quernheim, F. E. Golling, W. Zhang, M. Wagner, H.-J. Räder, T. Nishiuchi and K. Müllen, *Angew. Chem., Int. Ed.*, 2015, **54**, 10341–10346.

150 S. Setia and S. K. Pal, *ChemistrySelect*, 2016, **1**, 880–885.

151 A. Keerthi, I. C.-Y. Hou, T. Marszalek, W. Pisula, M. Baumgarten and A. Narita, *Chem.–Asian J.*, 2016, **11**, 2710–2714.

152 J. Dosso, J. Tasseroul, F. Fasano, D. Marinelli, N. Biot, A. Fermi and D. Bonifazi, *Angew. Chem.*, 2017, **129**, 4554–4558.

153 K. Oda, S. Hiroto, I. Hisaki and H. Shinokubo, *Org. Biomol. Chem.*, 2017, **15**, 1426–1434.

154 D. Lu, G. Zhuang, H. Wu, S. Wang, S. Yang and P. Du, *Angew. Chem., Int. Ed.*, 2017, **56**, 158–162.

155 Y. Hu, D. Wang, M. Baumgarten, D. Schollmeyer, K. Müllen and A. Narita, *Chem. Commun.*, 2018, **54**, 13575–13578.

156 W. Zhang, K. Gu, P. Hou, X. Lyu, H. Pan, Z. Shen and X.-h. Fan, *Soft Matter*, 2018, **14**, 6774–6782.

157 M. Ruppel, L.-P. Gazetas, D. Lungerich and N. Jux, *Eur. J. Org Chem.*, 2020, **2020**, 6352–6360.

158 M. M. Martin, F. Hampel and N. Jux, *Chem.–Eur. J.*, 2020, **26**, 10210–10212.

159 C. Dusold, D. I. Sharapa, F. Hampel and A. Hirsch, *Chem.–Eur. J.*, 2021, **27**, 2332–2341.

160 B. Zhang, L. Ruan, Y.-K. Zhang, H. Zhang, R. Li and P. An, *Org. Lett.*, 2023, **25**, 732–737.

161 D. Wang, C. Zhao, Y. Zhu, X. Zhang, X. Wang and P. An, *Chem.–Eur. J.*, 2024, **30**, e202402723.

162 H.-H. Chen, H.-H. Hung, Y.-H. Cheng, J.-W. Yu and J.-J. Lee, *Liq. Cryst.*, 2015, **42**, 1773–1778.

163 Y. Hu, L. F. Dössel, X.-Y. Wang, S. Mahesh, W. Pisula, S. De Feyter, X. Feng, K. Müllen and A. Narita, *ChemPlusChem*, 2017, **82**, 1030–1033.

164 K. Oda, S. Hiroto and H. Shinokubo, *J. Mater. Chem. C*, 2017, **5**, 5310–5315.

165 M. Lein, *Aust. J. Chem.*, 2018, **71**, 222–226.

166 Q. Chen, M. Baumgarten, M. Wagner, Y. Hu, I. C. Y. Hou, A. Narita and K. Müllen, *Angew. Chem., Int. Ed.*, 2021, **60**, 11300–11304.

167 W. Zhang, W. Yang, H. Pan, X. Lyu, A. Xiao, D. Liu, Y. Liu, Z. Shen, H. Yang and X.-H. Fan, *Soft Matter*, 2022, **18**, 3430–3436.

168 J. Müller, J. Buck and A. Hirsch, *Eur. J. Org Chem.*, 2023, **26**, e202201310.

169 A. Camellini, L. Rebecchi, A. Rubino, W. Niu, S. W. Kim, J. Ma, X. Feng and I. Kriegel, *Nanoscale*, 2023, **15**, 17138–17146.

170 S. Mörsel, R. Kellner and A. Hirsch, *Eur. J. Org Chem.*, 2023, **26**, e202300299.

171 J. I. Mapley, J. N. Smith, G. E. Shillito, S. J. Fraser-Miller, N. T. Lucas and K. C. Gordon, *Inorg. Chem.*, 2023, **62**, 11028–11036.

172 R. Li, B. Ma, S. Li, C. Lu and P. An, *Chem. Sci.*, 2023, **14**, 8905–8913.

173 C. Oleszak, P. R. Schol, C. L. Ritterhoff, M. Krug, M. M. Martin, Y. Bo, B. Meyer, T. Clark, D. M. Guldi and N. Jux, *Angew. Chem.*, 2024, **136**, e202409363.

174 J. Buck, F. Hampel and A. Hirsch, *Chem.–Eur. J.*, 2025, **31**, e202404000.

175 C. Suresh and S. R. Gadre, *J. Org. Chem.*, 1999, **64**, 2505–2512.

176 G. R. Desiraju and A. Gavezzotti, *Acta Crystallogr. Sect. B Struct. Sci.*, 1989, **45**, 473–482.

177 A. Gavezzotti and G. R. Desiraju, *Acta Crystallogr. Sect. B Struct. Sci.*, 1988, **44**, 427–434.

178 D. A. Britz and A. N. Khlobystov, *Chem. Soc. Rev.*, 2006, **35**, 637–659.

179 E. Clar, C. Ironside and M. Zander, *J. Chem. Soc.*, 1959, 142–147.

180 E. Clar and R. Schoental, *Polycyclic Hydrocarbons*, Springer, 1964.

181 J. C. Fetzer, *Large (C>= 24) Polycyclic Aromatic Hydrocarbons: Chemistry and Analysis*, John Wiley & Sons, 2000.

182 J. M. Robertson and J. Trotter, *J. Chem. Soc.*, 1961, 1280–1284.

183 R. Goddard, M. W. Haenel, W. C. Herndon, C. Krueger and M. Zander, *J. Am. Chem. Soc.*, 1995, **117**, 30–41.

184 W. Pisula, Ž. Tomović, C. Simpson, M. Kastler, T. Pakula and K. Müllen, *Chem. Mater.*, 2005, **17**, 4296–4303.

185 D. W. Breiby, F. Hansteen, W. Pisula, O. Bunk, U. Kolb, J. W. Andreasen, K. Müllen and M. M. Nielsen, *J. Phys. Chem. B*, 2005, **109**, 22319–22325.

186 C.-y. Liu, A. Fechtenkötter, M. D. Watson, K. Müllen and A. J. Bard, *Chem. Mater.*, 2003, **15**, 124–130.

187 D. Wasserfallen, I. Fischbach, N. Chebotareva, M. Kastler, W. Pisula, F. Jäckel, M. D. Watson, I. Schnell, J. P. Rabe and H. W. Spiess, *Adv. Funct. Mater.*, 2005, **15**, 1585–1594.

188 S. Brown, I. Schnell, J. D. Brand, K. Müllen and H. W. Spiess, *J. Mol. Struct.*, 2000, **521**, 179–195.

189 S. P. Brown, I. Schnell, J. D. Brand, K. Müllen and H. W. Spiess, *Phys. Chem. Chem. Phys.*, 2000, **2**, 1735–1745.

190 C. Grigoriadis, N. Haase, H. J. Butt, K. Müllen and G. Floudas, *Adv. Mater.*, 2010, **22**, 1403–1406.

191 C. Grigoriadis, N. Haase, H.-J. Butt, K. Müllen and G. Floudas, *Soft Matter*, 2011, **7**, 4680–4689.

192 G. Zhang, W. Jin, T. Fukushima, A. Kosaka, N. Ishii and T. Aida, *J. Am. Chem. Soc.*, 2007, **129**, 719–722.

193 T. Yamamoto, T. Fukushima, A. Kosaka, W. Jin, Y. Yamamoto, N. Ishii and T. Aida, *Angew. Chem.*, 2008, **120**, 1696–1699.

194 Y. Yamamoto, T. Fukushima, W. Jin, A. Kosaka, T. Hara, T. Nakamura, A. Saeki, S. Seki, S. Tagawa and T. Aida, *Adv. Mater.*, 2006, **18**, 1297–1300.

195 W. Jin, T. Fukushima, M. Niki, A. Kosaka, N. Ishii and T. Aida, *Proc. Natl. Acad. Sci. U. S. A.*, 2005, **102**, 10801–10806.

196 W. Jin, T. Fukushima, A. Kosaka, M. Niki, N. Ishii and T. Aida, *J. Am. Chem. Soc.*, 2005, **127**, 8284–8285.

197 H. C. Hesse, D. Lembke, L. Dössel, X. Feng, K. Müllen and L. Schmidt-Mende, *Nanotechnology*, 2010, **22**, 055303.

198 H. H. Dam, K. Sun, E. Hanssen, J. M. White, T. Marszalek, W. Pisula, J. Czolk, J. Ludwig, A. Colsmann, M. Pfaff, D. Gerthsen, W. W. H. Wong and D. J. Jones, *ACS Appl. Mater. Interfaces*, 2014, **6**, 8824–8835.

199 S.-H. Wu and H.-H. Chen, *Tetrahedron*, 2019, **75**, 220–229.

200 W. W. H. Wong, J. Subbiah, S. R. Puniredd, B. Purushothaman, W. Pisula, N. Kirby, K. Müllen, D. J. Jones and A. B. Holmes, *J. Mater. Chem.*, 2012, **22**, 21131–21137.

201 H. C. Hesse, C. Schaffer, C. Hundschell, A. Narita, X. Feng, K. Müllen, B. Nickel and L. S. Mende, *Phys. Status Solidi A*, 2012, **209**, 785–789.

202 L. F. Dössel, V. Kamm, I. A. Howard, F. Laquai, W. Pisula, X. Feng, C. Li, M. Takase, T. Kudernac, S. De Feyter and K. Müllen, *J. Am. Chem. Soc.*, 2012, **134**, 5876–5886.

203 C. Gao, Z. Qiao, K. Shi, S. Chen, Y. Li, G. Yu, X. Li and H. Wang, *Org. Electron.*, 2016, **38**, 245–255.

204 L. Liang, X.-Q. Chen, L.-N. Liu, J. Ling, X. Xiang, W.-J. Xiao, C.-W. Ge, F.-G. Zhao, G. Xie, Z. Lu, J. Li and W.-S. Li, *Tetrahedron*, 2016, **72**, 4329–4336.

205 F.-J. Lin, H.-H. Chen and Y.-T. Tao, *ACS Appl. Mater. Interfaces*, 2019, **11**, 10801–10809.

206 S. Kumar, S. Pola, C.-W. Huang, M. M. Islam, S. Venkateswarlu and Y.-T. Tao, *J. Org. Chem.*, 2019, **84**, 8562–8570.

207 Z. Xu, Y. Liu, A. Chandresh, P. B. Pati, V. Monnier, L. Heinke, F. Odobel, S. Diring, R. Haldar and C. Wöll, *Adv. Funct. Mater.*, 2024, **34**, 2308847.

208 L. Qin, Y. Zhang, X. Wu, L. Nian, Z. Xie, L. Liu and Y. Ma, *Small*, 2015, **11**, 3028–3034.

209 Z.-S. Wu, Y.-Z. Tan, S. Zheng, S. Wang, K. Parvez, J. Qin, X. Shi, C. Sun, X. Bao, X. Feng and K. Müllen, *J. Am. Chem. Soc.*, 2017, **139**, 4506–4512.

210 D. He, F. Xiao, Z. Wang, A. He, R. Liu and G. Jin, *Nanoscale Res. Lett.*, 2019, **14**, 1–8.

211 A. A. Peyghan and J. Beheshtian, *Thin Solid Films*, 2020, **704**, 137979.

212 X. Wu, Z. Zhang and H. Soleymanabadi, *Solid State Commun.*, 2020, **306**, 113770.

213 L. Buenaño, Y. Ajaj, C. Padilla, B. Vaca Barahona, N. Mejía, R. B. D. Real, B. S. R. Oviedo, J. J. F. Fiallos and S. K. Saraswat, *Chem. Phys.*, 2024, **579**, 112194.

214 R. G. S. Nair, A. K. N. Nair, B. Yan and S. Sun, *Phys. Chem. Chem. Phys.*, 2025, **27**, 218–231.

215 V. Vij, V. Bhalla and M. Kumar, *ACS Appl. Mater. Interfaces*, 2013, **5**, 5373–5380.

216 J. Zhang, S. You, S. Yan, K. Müllen, W. Yang and M. Yin, *Chem. Commun.*, 2014, **50**, 7511–7513.

217 A. A. Salari, *C. R. Chim.*, 2017, **20**, 758–764.

218 N. Javadi and M. Vatanparast, *Struct. Chem.*, 2018, **29**, 929–935.

219 S. Liu, P. Zhu, S. Zou and S. Ebrahimiasl, *Comput. Theor. Chem.*, 2021, **1204**, 113412.

220 Y. Cao, A. S. El-Shafay, H. A. Ibrahium, N. S. Awwad, M. Y. Alshahrani and S. Ebrahim, *Chem. Phys.*, 2022, **553**, 111388.

221 Y. Wang, Z. Wang, Z. Qiu, X. Zhang, J. Chen, J. Li, A. Narita, K. Müllen and C.-A. Palma, *ACS Nano*, 2023, **17**, 18832–18842.

222 M. Yin, J. Shen, W. Pisula, M. Liang, L. Zhi and K. Müllen, *J. Am. Chem. Soc.*, 2009, **131**, 14618–14619.

223 M.-M. Song, H.-H. Xiang, M.-Y. Fei, D.-P. Lu, T.-C. Jiang, Y.-Q. Yu, R. Liu and Y.-X. Shen, *RSC Adv.*, 2018, **8**, 40554–40563.

224 A. A. Dolatabad, M. Salehpour and Z. Saadati, *J. Mol. Liq.*, 2024, **407**, 125206.

225 T. Hirose, Y. Miyazaki, M. Watabe, S. Akimoto, T. Tachikawa, K. Kodama and M. Yasutake, *Tetrahedron*, 2015, **71**, 4714–4721.

226 S. Masoomi-Godarzi, M. Liu, Y. Tachibana, V. D. Mitchell, L. Goerigk, K. P. Ghiggino, T. A. Smith and D. J. Jones, *Adv. Energy Mater.*, 2019, **9**, 1901069.

227 Y.-L. Kuo, C.-Y. Tseng, C.-W. Tseng, K.-T. Chu, Y.-C. Liu, M.-H. Chiang, A. Saeki, Y.-T. Tao and H.-H. Chen, *ACS Appl. Polym. Mater.*, 2020, **2**, 248–255.

228 X. Ou-Yang, Y.-C. Huang, Y.-C. Chi, M. Egashira, H.-C. Yang and H.-H. Chen, *Polym. Chem.*, 2023, **14**, 737–746.

229 H.-C. Yang, Y.-S. Du, J.-J. Lee, C.-H. Yeh, M.-C. Tseng, Y.-C. Ho, H.-W. Kuo, H. Yoshida, A. Fujii, M. Ozaki, Y.-T. Tao, T. Akutagawa and H.-H. Chen, *Langmuir*, 2024, **40**, 16846–16854.

230 J. Cao, Y.-M. Liu, X. Jing, J. Yin, J. Li, B. Xu, Y.-Z. Tan and N. Zheng, *J. Am. Chem. Soc.*, 2015, **137**, 10914–10917.

231 J. S. Rocha-Ortiz, J. Wu, J. Wenzel, A. J. Bornschlegl, J. D. Perea, S. Leon, A. Barabash, A.-S. Wollny, D. M. Guldi, J. Zhang, A. Insuasty, L. Lüer, A. Ortiz, A. Hirsch and C. J. Brabec, *Adv. Funct. Mater.*, 2023, **33**, 2304262.

232 S.-G. Kim, T. de Monfreid, J.-H. Kim, F. Goubard, J. J. Berry, K. Zhu, T.-T. Bui and N.-G. Park, *ACS Energy Lett.*, 2023, **8**, 2267–2275.

233 Z.-E. Shi, K. Kollimalaian, J.-K. Peng, C.-W. Lin, W.-T. Peng, B.-H. Jiang, Y. H. Lin, L.-Y. Yang, Y.-C. Lin, P. Venkatakrishnan, Y. J. Chang and C.-P. Chen, *Adv. Energy Mater.*, 2025, **15**, 2404234.